UNIVERSIDADE FEDERAL DO PARANÁ

LAÍS GONÇALVES FERNANDES

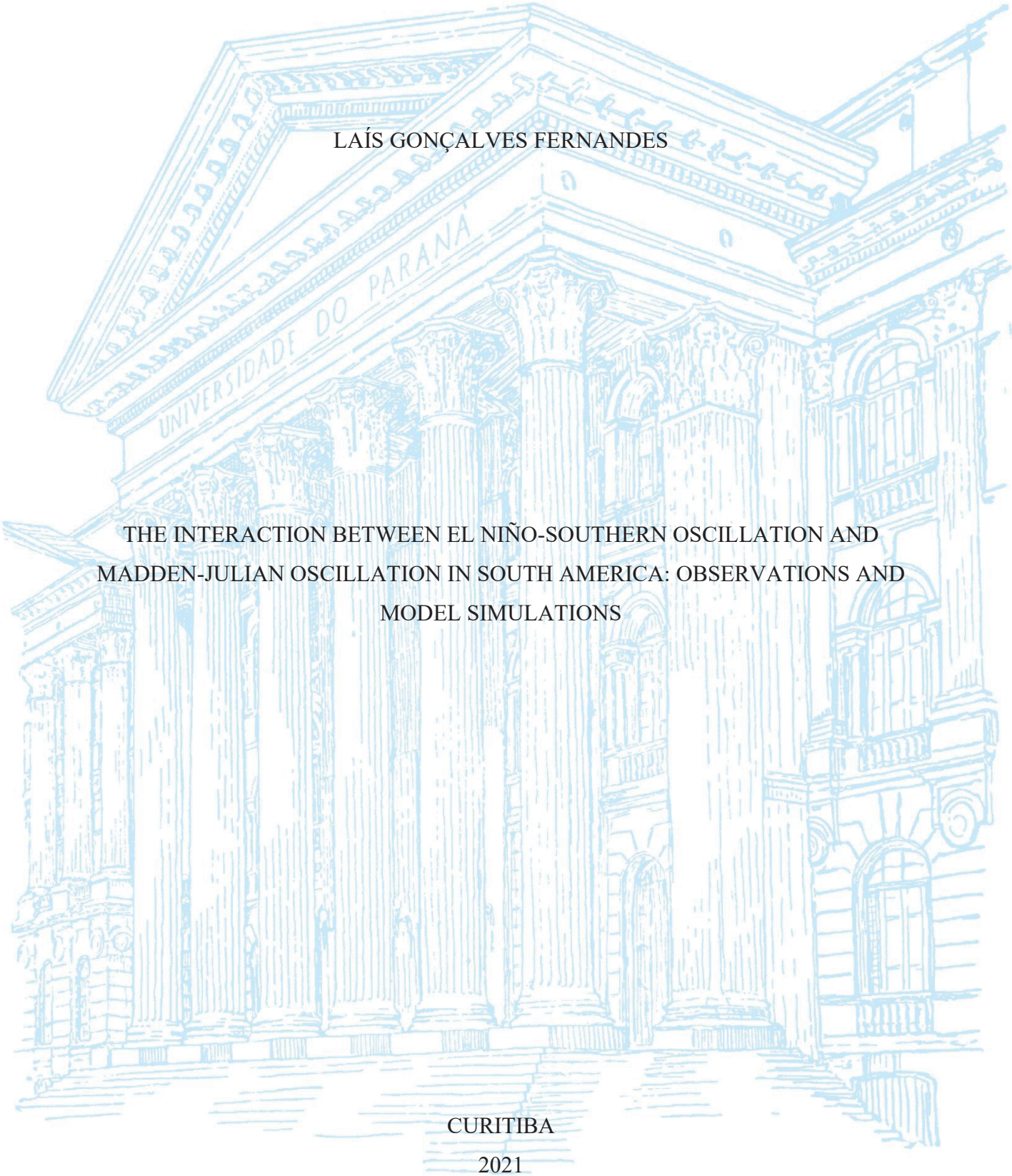

THE INTERACTION BETWEEN EL NIÑO-SOUTHERN OSCILLATION AND MADDEN-JULIAN OSCILLATION IN SOUTH AMERICA: OBSERVATIONS AND MODEL SIMULATIONS

CURITIBA

2021

LAÍS GONÇALVES FERNANDES

THE INTERACTION BETWEEN EL NIÑO-SOUTHERN OSCILLATION AND MADDEN-JULIAN OSCILLATION IN SOUTH AMERICA: OBSERVATIONS AND MODEL SIMULATIONS

Tese apresentada ao Programa de Pós-Graduação em Engenharia de Recursos Hídricos e Ambiental, Setor de Ciência e Tecnologia, Universidade Federal do Paraná, como requisito parcial à obtenção do título de Doutora em Engenharia de Recursos Hídricos e Ambiental.

Orientadora: Prof.ª Dr.ª Alice Marlene Grimm

CURITIBA

2021

Catalogação na Fonte: Sistema de Bibliotecas, UFPR
Biblioteca de Ciência e Tecnologia

F363i Fernandes, Laís Gonçalves

The interaction between El Niño-Southern Oscillation and Madden-Julian Oscillation in South America: observations and model simulations [recurso eletrônico] / Laís Gonçalves Fernandes - Curitiba, 2021.

Tese (doutorado) - Programa de Pós-Graduação em Engenharia de Recursos Hídricos e Ambiental, Setor de Ciências e Tecnologia, Universidade Federal do Paraná.

Orientadora: Profa. Dra. Alice Marlene Grimm

1. Engenharia. 2. Climatologia. 3. Meteorologia. I. Universidade Federal do Paraná. II. Grimm, Alice Marlene. III. Título.

CDD 551.51011

Bibliotecário: Nilson Carlos Vieira Junior CRB9/1797

MINISTÉRIO DA EDUCAÇÃO
SETOR DE TECNOLOGIA
UNIVERSIDADE FEDERAL DO PARANÁ
PRÓ-REITORIA DE PESQUISA E PÓS-GRADUAÇÃO
PROGRAMA DE PÓS-GRADUAÇÃO ENGENHARIA DE RECURSOS HÍDRICOS E AMBIENTAL - 40001016021P0

APPROVAL MINUTE

The Examining Board is designated by the Faculty of the Graduate Program of the Federal University of Paraná in ENGENHARIA DE RECURSOS HÍDRICOS E AMBIENTAL where invited to argue the DISSERTATION of PHILOSOPHY DOCTOR by **LAÍS GONÇALVES FERNANDES** , entitled: **The interaction between El Niño-Southern Oscillation and Madden-Julian Oscillation in South America: observations and model simulations**, under the supervision of Dr. ALICE MARLENE GRIMM, which and after assessment of the candidate and the work, the Examining Board decided for the APPROVAL in the present rite.

The granting of the title of philosophy doctor is contingent upon the fulfillment of all the requirements indicated by the Examining Board and terms determined in the regulation of the Graduate Program.

CURITIBA, November 16th, 2021.

Eletronic Signature
06/12/2021 16:03:27.0
ALICE MARLENE GRIMM
President of the Examining Board

Eletronic Signature
08/12/2021 12:13:12.0
ALEXANDRE KOLODYNSKIE GUETTER
Internal Member(UNIVERSIDADE FEDERAL DO PARANÁ)

Eletronic Signature
06/12/2021 15:38:30.0
DANIEL HENRIQUE MARCO DETZEL
Internal Member(UNIVERSIDADE FEDERAL DO PARANÁ)

Eletronic Signature
14/12/2021 18:21:05.0
MARY TOSHIE KAYANO
External Member (INSTITUTO NACIONAL DE PESQUISAS ESPACIAIS)

Eletronic Signature
07/12/2021 11:16:42.0
ELOY KAVISKI
Internal Member(UNIVERSIDADE FEDERAL DO PARANÁ)

Eletronic Signature
17/12/2021 09:11:19.0
EDMILSON DIAS DE FREITAS
External Member (INSTITUTO DE ASTRONOMIA, GEOFíSICA E CIêNCIAS ATMOSFéRICAS - UNIVERSIDADE DE SãO PAULO)

“The universal force is LOVE.
Love is light that enlightens those who give and receive it.
Love is gravity, because it makes some people feel attracted to others. Love is power, because it multiplies the best we have, and allows humanity not to be extinguished in their blind selfishness. Love unfolds and reveals.”

Albert Einstein

RESUMO

A Oscilação de Madden-Julian (OMJ) e o El Niño-Oscilação Sul (ENOS) são, respectivamente, os principais modos de variabilidade climática intrassazonal e interanual afetando a precipitação da América do Sul (AS). Vários estudos têm focado a modulação dos impactos da OMJ pelo ENOS ao redor do globo. Alguns deles mostram variações na propagação para leste da OMJ sob diferentes estados básicos associados ao ENOS (El Niño, EN, e La Niña, LN). Neste estudo, verifica-se se a modulação da OMJ pelo ENOS pode afetar as teleconexões da OMJ e seus impactos sobre a AS. Variações na propagação para leste da OMJ podem influenciar o estabelecimento da teleconexão trópicos-trópicos da OMJ entre o Pacífico e a AS. Além disso, mudanças no estado básico devido aos diferentes estados do ENOS podem também afetar a convecção sobre o Pacífico Sul subtropical central-leste (ou região fonte), a qual desencadeia a teleconexão trópicos-extratrópicos da OMJ para a AS. O objetivo é compreender como o fenômeno ENOS influencia a OMJ e seus impactos na AS durante a estação de monção (dezembro, janeiro, e fevereiro – DJF). Os conjuntos de dados analisados são de observações e resultados de simulações do *UK Met Office Unified Model Global Ocean Mixed Layer* (MetUM-GOML3). Anomalias diárias são filtradas na banda de 20-90 dias, para reter apenas oscilações intrassazonais e analisar o efeito do ENOS na OMJ ao invés da soma das anomalias relacionadas ao ENOS e à OMJ. Composições de anomalias são calculadas em períodos quando ambos ENOS e OMJ estão ativos. As teleconexões da OMJ são estabelecidas mais tardiamente em EN (fase 1) que em LN (fase 8) nas observações. A teleconexão extratropical e seus impactos sobre o centro-leste da AS (CESA) subtropical intensificam em EN e LN e enfraquecem em anos neutros (NT). A convecção sobre a região fonte, a qual desencadeia a teleconexão trópicos-extratrópicos, é intensificada mais tardiamente e está um pouco mais para leste em EN (fases 8+1) que em LN (fases 7+8). Portanto, os impactos mais significativos na precipitação da AS acontecem mais tarde e mais para leste em EN (fase 1) que em LN (fase 8). O estado básico em EN melhora a convecção da OMJ e a sua propagação para leste no modelo, incluindo a convecção sobre a região fonte. As teleconexões trópicos-extratrópicos da OMJ estão mais fortes em simulações com ENOS em comparação com aquelas sem eventos ENOS. Surpreendentemente, o padrão de teleconexão extratropical aparece mais claramente nas simulações em LN, apesar da OMJ enfraquecida sob o estado básico da LN. Portanto, ambos os estados de ENOS no modelo e nas observações fornecem forçantes na região fonte que desencadeiam mais eficientemente as teleconexões extratropicais mais fortes que anos NT e em simulações sem ENOS, indicando efeitos não-lineares do ENOS nas anomalias da OMJ sobre a AS.

Palavras-chave: Precipitação. Teleconexões da OMJ. Interação ENOS-OMJ. Monção da América do Sul.

ABSTRACT

The Madden-Julian Oscillation (MJO) and the El Niño-Southern Oscillation (ENSO) are respectively the main intraseasonal and interannual climate variability modes affecting the South America (SA) rainfall. Several studies have focused on the ENSO-driven modulation of the MJO and its impacts worldwide. Some of them show variations in the eastward propagation of the MJO within different ENSO background states (El Niño, EN, and La Niña, LN). The present study verifies if the ENSO modulation affects the MJO teleconnections and their impacts on SA. Variations in the eastward MJO propagation may influence the establishment of the MJO tropics-tropics teleconnection between the Pacific and SA. Moreover, changes in the background by different ENSO states may also affect the convection over the subtropical central-east South Pacific (or source region), which triggers the MJO tropics-extratropics teleconnection to SA. The goal is to understand how the ENSO phenomenon influences the MJO and its impacts on SA during the summer monsoon season (December, January, and February – DJF). The datasets analyzed are observational data and outputs from simulations with the UK Met Office Unified Model Global Ocean Mixed Layer (MetUM-GOML3). Daily anomalies are filtered in the 20-90 day band, to retain only intraseasonal oscillations and analyze the ENSO effect on the MJO rather than the sum of the MJO and ENSO-related anomalies. Composite anomalies are computed over periods when both ENSO and MJO are active. The MJO teleconnections are fully established later in EN (phase 1) than in LN (phase 8) in observations. The extratropical teleconnection and its impacts over the subtropical central-east SA (CESA) intensify in EN and LN and weaken in neutral (NT) years. The convection over the source region, which triggers tropics-extratropics teleconnection, is enhanced later, and is slightly shifted eastwards in EN (phases 8+1) than in LN (phases 7+8). Hence, the most significant impacts on SA precipitation happen later and more to the east in EN (phase 1) than LN (phase 8). The EN basic state improves the MJO convection and its eastward propagation in the model, including the convection over the source region. The MJO tropics-extratropics teleconnections are stronger in simulations with ENSO with respect to those without ENSO. Surprisingly, an improved extratropical teleconnection pattern appears in simulations during LN, despite MJO weakening in the LN basic state. Therefore, both ENSO states in the model and observations generate forcing in the source region that more efficiently triggers stronger extratropical teleconnections than NT years and simulations without ENSO, indicating nonlinear ENSO effects on MJO-related anomalies over SA.

Keywords: Precipitation. MJO teleconnections. ENSO-MJO interaction. South American monsoon.

LIST OF PAPERS

The present thesis is based on the following scientific publications:

(1) Fernandes, L. G.; Grimm, A. M. (2022) **Global ENSO modulation of MJO and its impacts on South America.**

(2) Fernandes, L. G.; Grimm, A. M.; Klingaman, N. P. (2022) **MJO impacts on South America and their modulation by ENSO in MetUM-GOML3 model.**

ACKNOWLEDGEMENTS

First and foremost, praises and thanks to God, the Almighty, for His showers of blessing throughout my research work. I want to express my deep and sincere gratitude to my advisor, Professor Dr. Alice M. Grimm, for the continuous support of my Ph.D. study and research, for her patience, motivation, enthusiasm, and immense knowledge. Her guidance helped me in all the time of research and writing of this thesis. I could not have imagined having a better advisor and mentor for my Ph.D. study.

My profound thanks to her and Dr. Nicholas Klingaman for offering me a Ph.D. student visit to the Meteorology Department, University of Reading, United Kingdom, under Dr. Klingaman's supervision. Dr. Klingaman always encouraged me with his insightful comments and challenging questions. I consider myself a very lucky individual as I had this opportunity abroad. I am also grateful for having a chance to meet so many wonderful people and professionals who led me through this sandwich doctorate period.

Thanks to Professors Dr. Alexandre K. Guetter, Dr. Daniel H. M. Detzel, and Dr. Eloy Kaviski for their marvelous lectures at UFPR and for taking part in all examination committees of my qualifying exams and the thesis committee. Also, thanks to Dr. Mary T. Kayano and Dr. Edmilson D. de Freitas for taking part in this thesis committee at the Thesis defense. Their comments and suggestions have enriched this thesis. Thanks to all staff and students from the Postgraduate Program in Water Resources and Environmental Engineering (PPGERHA) at Federal University of Paraná (UFPR) for all support during my research journey, helping me along the way.

Special thanks to my office mates at UFPR Meteorology Laboratory, Kénedy Silverio, Nicole Laureanti, Luana Scheibe, and Leonardo Yokohama, for their assistance which I needed at the Laboratory, for their friendship and interesting conversations. Special thanks to my office mates Carolina Natel (from UFPR), Armenia Franco-Diaz, Julia Mindlin, Godwin Ayesiga, and Gabriel Perez (from the University of Reading) for our fun conversations and pleasant moments supporting me throughout my sandwich doctorate period. Last but not least, I would like to thank my family, my mother Marli Gonçalves, my father, Júlio C. Fernandes, and my husband, Rodrigo B. Duarte (and our dogs) for supporting me spiritually throughout my life, for their love, patience, understanding, and emotional support. It is to them that this thesis is dedicated.

LIST OF FIGURES

Figure 1: The seasonal precipitation climatology (mm/month) in SA, with precipitation data between 1950 and 2009. 20
Figure 2: (Left) scheme shows the trade winds, the convection in the Walker cell and the SST anomalies over the equatorial Pacific Ocean in (a) neutral ENSO years, (b) EN, and (c) LN years. (Right) SST anomalies in (a) 1996 (neutral), (b) 1997 (EN), and (c) 1999 (LN). Red (blue) colors show positive (negative) SST anomalies. (Images from: https://www.youtube.com/watch? v=WPA-KpldDVc). 22
Figure 3: Upper-level streamfunction anomalies pattern which characterizes the main PSA mode in EN years. The contour interval is $1.0\,x\,106\,m2s-1$. Continuous (dashed) lines show positive (negative) streamfunction anomalies. Shaded areas represent areas with confidence levels better than 95%. The curved arrow shows the extratropical Rossby wave pathway. Modified from Vera et al. (2004). 23
Figure 4: SA topography, available on: (https://photojournal.jpl.nasa.gov/catalog/PIA03388). The colors show the elevation, green for the lower regions, yellow for intermediate heights, purple and white for mountain regions, like the Andes Mountains. The figure also displays the main regions in the continent impacted by climate variability modes: southeastern SA (SESA, in red), and central-east SA (CESA in blue). Other regions cited in the text: Amazon and NE Brazil. 24
Figure 5: Circulation anomalies at 700 hPa, for periods of (a) increase (white circles) and (b) decrease (gray circles) of convective cloudiness over SESA and CESA (red squares from Fig. 4). H and L represent the anticyclonic and cyclonic circulation anomalies, respectively. The strengthening (weakening) of the subtropical jet is characterized by arrows with different sizes. The meridional arrow to the east of the Andes Mountains is the South American low-level jet. Modified from Vera et al. (2006) 25
Figure 6: Equatorial Pacific Ocean areas known as Niño 1+2, Niño 3, Niño 3.4 e Niño 4. From NOAA, 2014. The Niño 3 region is analogous to the ENSO east region, and the Niño 4 region is over the ENSO central region, which reaches the Date Line. 26
Figure 7: Composite anomalies of OLR in each MJO phase in DJF according to the Wheeler and Hendon (2004) index. Contour interval is 2.5 W/m^2. The color bar indicates confidence levels for OLR anomalies, with signs indicating positive or negative anomalies. The red arrow shows the eastward MJO propagation of the OLR anomalies (Adapted from Grimm, 2019). 28
Figure 8: Circulation anomalies associated with the opposite phases of the SA intraseasonal variability dominant mode in DJF, which (a) strengthens or (b) weakens the SACZ. Orange arrows: SA low-level jet. Red circles indicate areas where mesoscale systems are intensified (From Mechoso et al., 2005). 32
Figure 9: (a) OLR anomalies associated with the MJO phase 8. Contour interval is 2.5 W/m^2. The ellipses indicate the convection anomalies relevant to the response in the tropics and in the SH. (b) 200 hPa streamfunction anomalies combined at phases 8 and 1. Contour interval is $6 \times 105\,m2s-1$; zero line omitted. (c) 200 hPa positive/negative idealized divergence

anomalies prescribed for the simulation of the tropical and SH response. Contour interval is $10 \times 10 - 7\ s - 1$; zero line omitted. (d) Simulated 200 hPa streamfunction anomaly response. Contour interval is $2 \times 106\ m2s - 1$; zero line omitted. From Grimm (2019). 33
Figure 10: The schematic diagrams illustrating the typical patterns of MJO tropics-extratropics teleconnections to SA in MJO_{EN}phase1 (top panel) and MJO_{LN}phase8 (bottom panel). Blue and red thick contours display the MJO teleconnection at 200 hPa. Letter A (C) depicts the anticyclonic (cyclonic) circulation anomaly. The color bar shows the SST anomalies. The cloud shape in green represents convection associated with MJO (small convection) and ENSO (large convection), and the cloud shape orange denotes the MJO subsidence.....140
Figure 11: Scheme shows changes in the Walker circulation due to (a) EN and (b) LN, and how they affect the intraseasonal OLR anomalies at the equator, over Central Pacific (CP), Eastern Pacific (EP), and South America (SA) in MJO phases 6+7 (top) and 8+1 (bottom). Red arrows: Walker circulation in each ENSO phase. Green arrows: Vertical motion associated with MJO. The cloud shape in green represents convection associated with MJO and ENSO, and the cloud shape orange denotes the subsidence.....143

LIST OF ACRONYMS

AGCMs – Atmospheric General Circulation Models

AMO – Atlantic Multidecadal Oscillation

ANA – Brazilian Water Agency

CESA – Central-east South America

CGCMs – Coupled General Circulation Models

CMIP5 – Coupled Model Intercomparison Project Phase 5

DJF – December, January, and February

ENSO – El Niño-Southern Oscillation

EN – El Niño

EOFs – Empirical Orthogonal Functions

ERSST.v3b – Extended Reconstructed Sea Surface Temperature

FL – Factor Loadings

FS – Factor Scores

GCMs – General Circulation Models

IPCC – Intergovernmental Panel on Climate Change

IPO – Interdecadal Pacific Oscillation

ITCZ – Intertropical Convergence Zone

JJA – June, July, and August

LN – La Niña

MAM – March, Abril, and May

MC – Maritime Continent

MCCs – Mesoscale Convective Complexes

MCSs – Mesoscale Convective Systems

MC-KPP – Multi-Column K Profile Parameterization Model

MetUM – Met Office Unified Model

MetUM-GOML – Met Office Global Ocean Mixed Layer Model

MJO – Madden-Julian Oscillation

NCDC – National Climatic Data Center

NCEP/NCAR – National Centers for Environmental Prediction/National Center for Atmospheric Research

NE – Northeast

NH – Northern Hemisphere

NT – Neutral ENSO

NW – Northwest

OLR – Outgoing longwave radiation

ONI – Oceanic Nino Index

PCA – Principal Component Analysis

PSA – Pacific-South America wave train

RMM – Real-time Multivariate MJO index

S2S – Seasonal to Subseasonal

SA – South America

SACZ – South Atlantic Convergence Zone

SAMS – South America Monsoon System

SESA – Southeastern South America

SH – Southern Hemisphere

SON – September, October, November

SP – South Pacific

SPCZ – South Pacific Convergence Zone

SST – Sea Surface Temperature

WMO – World Meteorological Organization

CONTENTS

1. Introduction 15

1.1. Justification 16

1.2. Hypothesis 18

1.3. Objectives 18

1.3.1. General objective 18

1.3.2. Specific objectives 18

1.4. Thesis Framework 19

2. Background 20

2.1. Precipitation Climatology 20

2.2. Interannual Climate Variability 21

2.3. Intraseasonal Climate Variability 27

2.3.1. MJO Dynamical Mechanisms 29

2.3.2. MJO impacts on SA 31

3. Data and methodology 35

3.1. Datasets 35

3.1.1. Observational datasets 35

3.1.2. Model output datasets for different MetUM-GOML3 set-ups 35

3.1.2.1. *N96 and N216 simulations* 37

3.1.2.2. *N96-ENSO and N216-ENSO simulations* 37

3.2. Methods 38

3.2.1. Definition of ENSO phases 38

3.2.1 Definition of MJO phases 39

3.2.2 Frequency of MJO phases in each ENSO state 40

3.2.3 Daily filtered anomalies 40

3.2.4 Composites 41

3.2.5 Frequency of extreme precipitation events 41

4. Manuscript 1 43

5. Manuscript 2 93

6. Summary and Conclusions 139

References 145

1. Introduction

The South American climate has been vastly investigated during the last 40 years, when technological advances have enabled the extension and modernization of hydrological, meteorological and oceanographic data collection networks over South America (SA) and the adjacent South Pacific and South Atlantic Oceans. After their verification by a quality control process, these datasets become crucial for diagnostic climate studies, for establishing initial conditions in numerical climate models and for validation of satellite original or derived data and models' output data. Besides, they are frequently assimilated by numerical models to generate spatially and temporally completed reanalysis datasets. While in the 1980s decade, the time step for data registration in the South American observation network were few times a day, nowadays they are obtained in each hour or even on a smaller time scale.

The development of tools to investigate the climate is essential for the Southern Hemisphere (SH). The climate change predicted for this century in this region is yet uncertain, and not as reliable as the climate change predictions for the Northern Hemisphere (NH), according to the Intergovernmental Panel on Climate Change (IPCC) report written in 2013.

These technological advances, which improved the tools for South American climate studies, allowed the progress of studies on the main atmospheric and oceanic patterns related to the natural climate variability in SA. Understanding the natural climate variability is crucial to detect the anthropogenic effect on climate change. The World Meteorological Organization (WMO) recommends a minimum period between 30 and 40 years to characterize a specific region's climate (WMO, 2019). However, to detect real changes in the climate behavior, the time series' length depends on the time scale of the climate variability mode investigated.

1.1. Justification

Investigating the atmospheric and oceanic patterns associated with natural climate variability helps distinguishing this variability from anthropogenic climate change and increasing the accuracy of climate forecasts. Climate models are not yet able to represent all climatic oscillations and their impacts, nor the connections between the different oscillations or the interactions between their impacts.

Knowledge about these interactions will contribute to a safer management of hydroelectricity generation and agricultural production, since prolonged droughts bring losses to both sectors. This knowledge is also important for preventing natural disasters or mitigating their effects when they cannot be avoided, since the overlapping effects of different climatic fluctuations can favor the occurrence of extreme precipitation events, which can cause floods and landslides.

The best-known impacts are those of the interannual variability associated with El Niño-Southern Oscillation (ENSO), although slower interdecadal variability also modulates the South American climate (e.g., Interdecadal Pacific Oscillation – IPO and Atlantic Multidecadal Oscillation – AMO). In addition, there is intraseasonal variability, of which the best known is the Madden-Julian Oscillation (MJO).

ENSO and MJO, respectively the main global interannual and intraseasonal climate variability modes, have been recognized as affecting significantly the rainfall over South America (SA) (GRIMM et al., 1998; GRIMM et al., 2000; GRIMM, 2003; 2004; 2011; ALVAREZ et al., 2015; GRIMM, 2019). This influence is exerted through tropics-tropics and tropics-extratropics teleconnections, especially by producing anomalous Walker circulation and Rossby waves (equatorial and extratropical) that affect SA (GRIMM and AMBRIZZI, 2009; GRIMM, 2019; CAI et al., 2020).

Therefore, it is important to analyze the ENSO-driven modulation of the MJO impacts on SA during the peak monsoon season (December-January-February, DJF), which is the rainy season over most of SA and also the season of strongest MJO and its impacts on SA. ENSO can affect the MJO impacts through the modification of the MJO convective anomalies and the atmospheric basic state through which the perturbations propagate, affecting the physical mechanisms by which the MJO influences rainfall variability in SA.

Work done on joint ENSO-MJO impacts in South America (SHIMIZU and AMBRIZZI, 2015) used an extended 5-month summer season, which mixes different spring and autumn effects, showing total accumulated anomalies of ENSO-MJO, using precipitation data sets filled in a grid, which generally underestimate extreme values. Such anomalies are shown for only 4 phases of the MJO, which decreases the temporal resolution of the ENSO-modulation analysis. Thus, the modulation of the MJO structure and propagation, the SA precipitation anomalies and teleconnections can be masked by the anomalies of ENSO superimposed on those of MJO and it is difficult to see the modulation produced by linear and nonlinear effects of ENSO.

The analysis in this study goes beyond the composites of total anomalies in some MJO phases for the three ENSO states, Neutral, El Niño and La Niña (NT, EN, LN), since it isolates the MJO impacts in each of these states, and it focuses on the more homogeneous DJF season. The proposed assessment of the modulation of the MJO impacts on SA by ENSO phases is important for subseasonal prediction (GRIMM et al., 2021) and necessary for validating the models' capability in representing the MJO impacts and its teleconnections in distinct backgrounds associated with ENSO. The low-frequency variability associated with ENSO can modify the seasonal background flow, affecting the distribution, strength and propagation of the intraseasonal oscillation and the extratropical teleconnection patterns. MJO and ENSO do not act independently and composite anomalies associated with their simultaneous action are not explained by simple linear combinations of composites based on the MJO and ENSO separately.

Another different approach proposed in this study is the inclusion of the analysis of the effects of simulated ENSO and MJO in a model, to identify the weaknesses and potentialities of the subseasonal numerical forecast of the effects of MJO in distinct states of the ENSO cycle. This type of prediction fills the gap between the weather forecast (prediction until seven days) and the seasonal climate prediction (prediction for three to nine months).

1.2. Hypothesis

The following hypothesis will be tested:

The interannual ENSO phenomenon alters the MJO impacts on SA rainfall and extremes on intraseasonal timescales.

This hypothesis defines the following research questions:

(1) How does the ENSO-MJO combination of two climate variability modes acting on distinct time scales, affect the precipitation anomalies and their extremes in SA?
(2) What are the changes in the MJO teleconnection patterns and the atmospheric circulation related to the joint influence?
(3) What are the effects of the ENSO-MJO combination reproduced in the latest version of the coupled GCM Met Office Global Ocean Mixed Layer (MetUM-GOML3, HIRONS et al., 2015)?

1.3. Objectives

1.3.1. General objective

To identify the ENSO influence on the MJO impacts on SA rainfall and its extremes through the ENSO modulation of the MJO structure, propagation and teleconnections.

1.3.2. Specific objectives

(1) Assess the ENSO influence on the MJO impacts on SA using observational datasets (in the Manuscript 1).
(2) Assess the ENSO influence on the MJO impacts on SA in simulations with the MetUM-GOML3 (HIRONS et al., 2015) (in the Manuscript 2).

1.4. Thesis Framework

The present thesis has six chapters. Chapter 2 shows the background of the ENSO and the MJO impacts on SA rainfall through their teleconnections. The data and methods are described in Chapter 3. Chapter 4 displays Manuscript 1, which shows changes in the MJO global convection, circulation anomalies, and its impacts on SA rainfall and extremes through each ENSO state in observations. Chapter 5 contains Manuscript 2, in which we verified if simulations of the MetUM-GOML3 reproduce those changes produced by the ENSO seen in Manuscript 1. Chapter 6 presents the summary of the research results, concluding remarks and recommendations for future works.

2. Background

2.1. Precipitation Climatology

Figure 1 shows the mean precipitation climatology for each season in SA. It is worth knowing about the mean precipitation behavior before analyzing the influence of the MJO and ENSO variability modes on SA rainfall. For instance, the continent has a large area in which the rainy season is the austral summer (December, January, and February, DJF) (Fig. 1b) when the South American Monsoon System (SAMS) is active (GRIMM et al., 2005; GRIMM and SILVA DIAS, 2011; LIEBMANN and MECHOSO, 2011). One of its most prominent characteristics is the South Atlantic Convergence Zone (SACZ), an extensive convective cloudiness band in the northwest-southeast direction. During the austral winter (June, July, and August, JJA) (Fig. 1d), this region displays a strong reduction in the mean precipitation climatology, which is even missing in some areas.

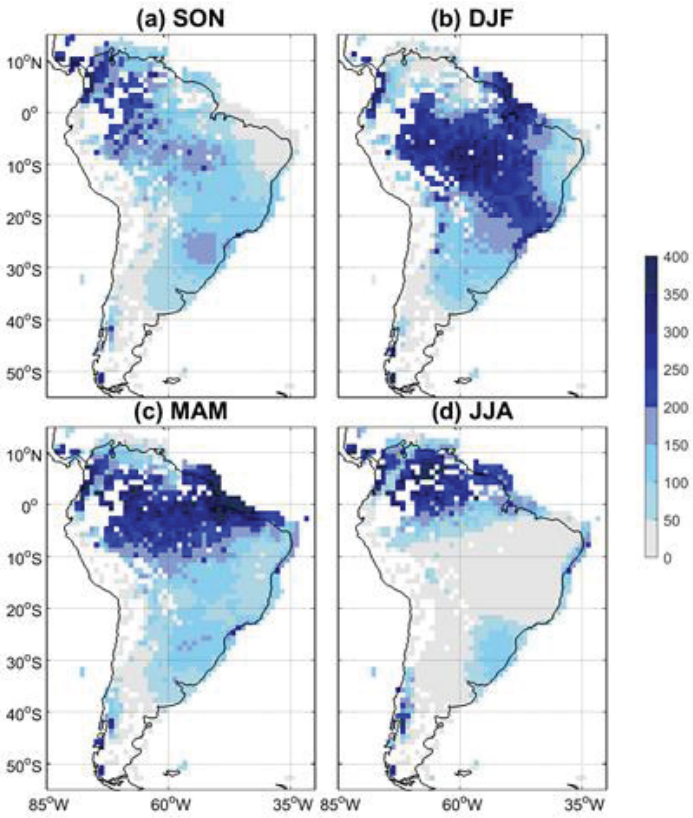

Figure 1: The seasonal precipitation climatology (mm/month) in SA, with precipitation data between 1950 and 2009.

On the other hand, in Southern Brazil and countries in the southern SA, the precipitation happens in all months during the year (GRIMM et al., 1998). In the austral winter and transition seasons (spring and autumn), the precipitation happens due to the intensification and undulation of the upper-level subtropical jet, which favors the cyclonic vorticity advection and the intensification of the synoptic systems in the mid-latitudes. In the spring season (September, October, and November, SON) (Fig. 1a), the mesoscale convective systems (MCSs), which can evolve to the mesoscale convective complexes (MCCs) (VELASCO and FRITSCH, 1987), are activated by the low-level jet which brings moisture flux from the Amazon to southeastern SA.

In North and Northeast (NE) Brazil, the increase in the precipitation climatology occurs in the austral autumn (March, April, and May, MAM) (Fig. 1c). During this season, the Intertropical Convergence Zone (ITCZ), a region of trade winds convergence, low-level pressure, and heavy rainfall, reaches its southernmost climatological position, following regions of warmest Sea Surface Temperature (SST) (KAYANO and ANDREOLI, 2009). The ITCZ migration to the north in JJA favors increased mean precipitation climatology over the northwest (NW) SA (Fig. 1d).

2.2. Interannual Climate Variability

The primary source of interannual climate variability in SA is the ENSO phenomenon. The ENSO is a coupled ocean-atmosphere system natural oscillator triggered by the weakening/strengthening of the trade winds over the equatorial Pacific Ocean, which changes SST, pressure, winds, and tropical convection (TRENBERTH, 1997; TRENBERTH and STEPANIAK, 2001). Its opposite phases are termed El Niño (EN) and La Niña (LN), with positive and negative SST anomalies, respectively, over the central-east tropical Pacific Ocean. The SST anomalies' peak happens during DJF, although an EN/LN event initiates during the austral winter and extends until the austral autumn/winter in the next year. Hence, an EN/LN event is referenced for two years, for instance, the EN 1997/98 (1997 as the first year or year 0, and 1998 as the last year or year +).

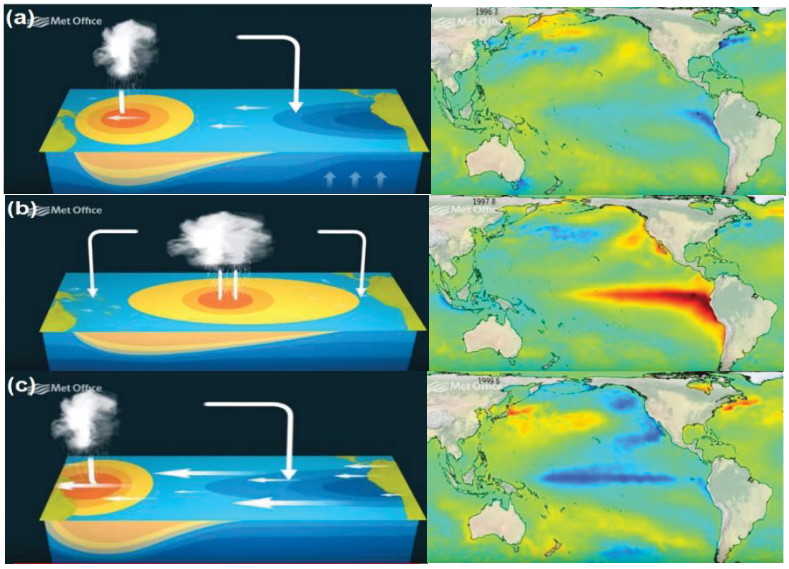

Figure 2: (Left) scheme shows the trade winds, the convection in the Walker cell and the SST anomalies over the equatorial Pacific Ocean in (a) neutral ENSO years, (b) EN, and (c) LN years. (Right) SST anomalies in (a) 1996 (neutral), (b) 1997 (EN), and (c) 1999 (LN). Red (blue) colors show positive (negative) SST anomalies. (Images from: https://www.youtube.com/watch? v=WPA-KpldDVc).

The SST anomalies cause anomalous heat and water vapor fluxes from the ocean to the atmosphere, changing the Walker and Hadley divergent circulations, directly affecting the tropics/subtropics. The anomalous convection produces Rossby waves. The ENSO extratropical teleconnections to SA produce the called Pacific South America (PSA) pattern, which is more active from September through December (MO, 2000; VERA et al., 2004). The PSA patterns are found in the Empirical Orthogonal Functions (EOFs) computed from monthly upper-level streamfunction anomalies over the SH during the austral spring (VERA et al., 2004). The main PSA mode (Fig. 3) originates to the east of the Date Line over the equatorial central Pacific, with a meridional pathway towards the Antarctic Peninsula. When it is over high latitudes, it changes its direction to the northeast, entering into SA, firstly reaching the southern portion of the continent (VERA et al., 2004). This ENSO extratropical teleconnection mechanism disturbs the atmospheric circulation and is responsible for changing the subtropical/extratropical SA rainfall (GRIMM, 2003; CAZES-BOEZIO et al., 2003).

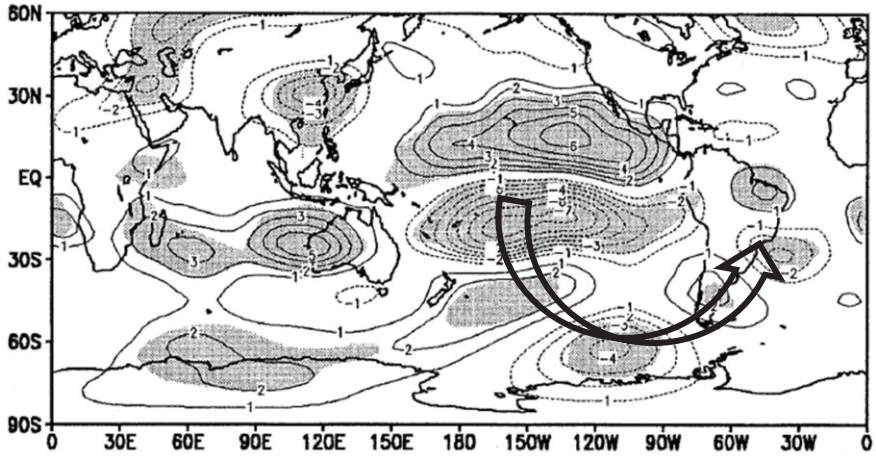

Figure 3: Upper-level streamfunction anomalies pattern which characterizes the main PSA mode in EN years. The contour interval is $1.0\,x\,10^6\,m^2s^{-1}$. Continuous (dashed) lines show positive (negative) streamfunction anomalies. Shaded areas represent areas with confidence levels better than 95%. The curved arrow shows the extratropical Rossby wave pathway. Modified from Vera et al. (2004).

The ENSO strongly influences the SA climate. Pioneer studies related geopotential height and wind (ACEITUNO, 1988), and precipitation (KOUSKY et al., 1984) with the opposite phases of the Southern Oscillation (i.e., the atmospheric pressure oscillation over the Equatorial Pacific, which characterizes the ENSO phenomenon). Ropelewski and Halpert (1987) identified two areas most affected by the positive ENSO phase (or EN), corroborating Kousky et al. (1984): the NE SA, with negative precipitation anomalies, due to the displacement of the Walker circulation, and the southeastern SA (SESA, Fig. 4), with positive precipitation anomalies, caused by the extratropical teleconnection wave train (GRIMM et al., 1998; GRIMM & AMBRIZZI, 2009). Uvo et al. (1998) found negative precipitation anomalies over the NE Brazil (Fig. 4) in EN, due to negative SST anomalies in the South Atlantic Ocean, reducing the precipitation during the austral autumn. In Marengo (1992), there is a reduction of precipitation and river levels in the Amazon (Fig. 4) in intense EN episodes when the SST anomalies exceed 1°C.

Figure 4: SA topography, available on: (https://photojournal.jpl.nasa.gov/catalog/PIA03388). The colors show the elevation, green for the lower regions, yellow for intermediate heights, purple and white for mountain regions, like the Andes Mountains. The figure also displays the main regions in the continent impacted by climate variability modes: southeastern SA (SESA, in red), and central-east SA (CESA in blue). Other regions cited in the text: Amazon and NE Brazil.

However, there was no significant quantity of rain gauge data over Brazil in most of the studies cited above. Grimm et al. (1998) was the first research to get data from 250 rain gauge stations in Southern Brazil. They showed that the positive precipitation anomalies detected in SESA (Fig. 4) by Ropelewski and Halpert (1987) in EN extended to Southern Brazil and that the impact on precipitation anomalies is more substantial during the austral spring of the year 0, especially in November.

Posterior studies have investigated the anomalous precipitation patterns in ENSO years over the entire SESA (GRIMM et al., 2000) and Brazil (GRIMM, 2003; 2004), analyzing thousands of monthly rain gauge data. Positive (negative) precipitation anomalies happen in SESA (CESA, Fig. 4) during SON of the year 0 in EN, associated with the PSA (Fig. 3). The teleconnection wave train establishes a cyclonic-anticyclonic circulation pair in the upper-levels over SA. It intensifies the South American low-level jet (arrow to the east of the Andes Mountains in Fig. 5a) and the upper-level subtropical jet (large arrow in Fig. 5a). This pair favors the cyclonic vorticity advection over SESA and the appearance of cyclones at the surface. The positive (negative) streamfunction or cyclonic (anticyclonic) circulation anomalies in Fig. 3 represent the low (high) pressure, L (H) in Fig. 5a.

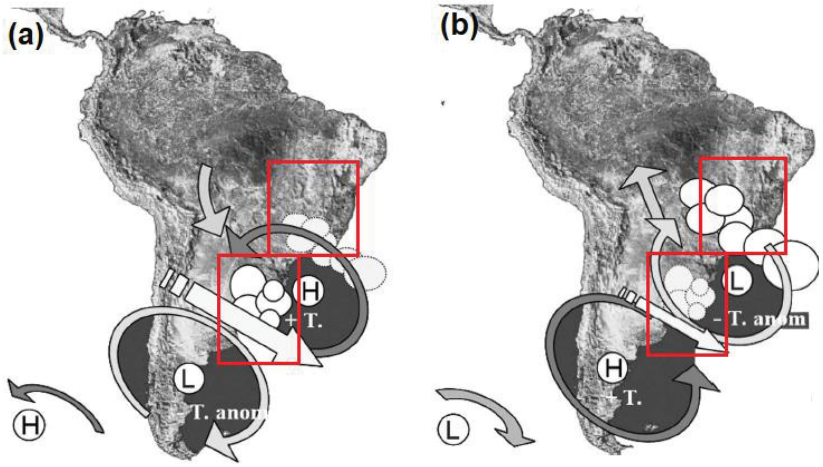

Figure 5: Circulation anomalies at 700 hPa, for periods of (a) increase (white circles) and (b) decrease (gray circles) of convective cloudiness over SESA and CESA (red squares from Fig. 4). H and L represent the anticyclonic and cyclonic circulation anomalies, respectively. The strengthening (weakening) of the subtropical jet is characterized by arrows with different sizes. The meridional arrow to the east of the Andes Mountains is the South American low-level jet. Modified from Vera et al. (2006).

During the austral spring of LN episodes, there are negative precipitation anomalies in SESA, and the circulation anomalies are opposite (Fig. 5b) to EN (Fig. 5a). In this season, the precipitation anomalies in SESA/CESA are associated with the ENSO extratropical teleconnections. However, in the austral summer, the SA anomalous precipitation dipole changes entirely over CESA and partially over SESA (GRIMM 2003; 2004) due to local mechanisms. The anomalous precipitation dipole during the austral spring is responsible for inverting the dipole in the austral summer (GRIMM et al., 2007). This condition favors the appearance of the SACZ in CESA during the austral summer in EN.

Grimm and Tedeschi (2009) have analyzed the ENSO influence on the frequency and intensity of the extreme events over SA, since the most dramatic consequences of climate variability are natural disasters, for example, floods and mudslides occasioned by intense and persistent precipitation in a short time. They have shown that the extreme events are more frequent and intense in SESA during the austral spring of the year 0 of EN, since the circulation anomalies associated with the extreme events are similar to the circulation anomalies in EN (Fig. 5a). In the austral summer, extreme events are more frequent in CESA, mainly over the SACZ. However, the condition which triggers the extreme events has a local rather than a remote forcing. Extensive SA regions show a higher frequency of extreme events in the EN episodes, highlighting that the interannual climate variability influence is more

significant on the extreme daily precipitation than on the total monthly or seasonal precipitation (GRIMM and TEDESCHI, 2009).

The studies mentioned above use the definition of ENSO years based on the SST anomalies over the Niño 3 and Niño 3.4 regions (Fig. 6). Observing the anomalous SST spatial patterns over the last decades, Ashok and Yamagata (2009) concluded that there are two main ENSO modes, the central ENSO and the east ENSO. The difference between them is the location of the most intense SST anomalies over the equatorial Pacific, in the central or east equatorial Pacific region. The extratropical teleconnection mechanisms also change between the ENSO types (YEH et al., 2009).

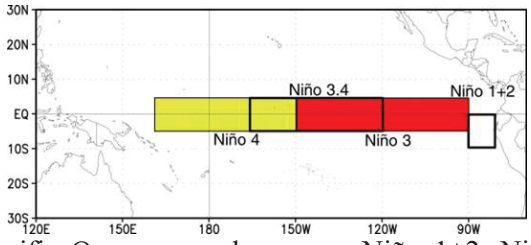

Figure 6: Equatorial Pacific Ocean areas known as Niño 1+2, Niño 3, Niño 3.4 e Niño 4. From NOAA, 2014. The Niño 3 region is analogous to the ENSO east region, and the Niño 4 region is over the ENSO central region, which reaches the Date Line.

The new findings prompted new analyzes focusing on SA precipitation anomalies (RODRIGUES et al., 2011; RODRIGUES and MCPHADEN, 2014; TEDESCHI et al., 2013), and comprehensive studies assessed the precipitation, circulation anomalies and frequency of extreme events associated with the central and east EN and LN (TEDESCHI et al., 2015; 2016). These investigations have considered the ENSO classification according to its position in the central or east equatorial Pacific rather than the Niño regions (Fig. 6). Tedeschi et al. (2015; 2016) concluded that typical patterns of anomalous precipitation and frequency of extreme events found during the east ENSO are different from those displayed during the central ENSO, although the differences vary from one season to another. The most significant difference between the two ENSO types happens during the autumn of the year (+) (TEDESCHI et al., 2015; 2016).

The NE Brazil presents the most significant impacts during the autumn. Tedeschi et al. (2016) have detected positive precipitation anomalies in the North and NE SA in central LN, while in east LN, they are restricted to the NE region. During autumn of east EN the precipitation anomalies are negative, but in central EN they are not significant, and even tend

to be positive. Besides, both LN modes (central and east) and the central EN increase extreme events in this region.

The ENSO is the most frequent climate variability mode investigated in diagnostic climate studies in SA. Besides, the phenomenon is the climate variability mode better predicted by the statistical and dynamical climate models. However, the prediction quality varies according to the year's season and the intensity of the SST anomalies in the Pacific Ocean (JIN et al., 2008). In dynamical climate models, the effect of the ENSO global teleconnections is shifted and smoothed over SA (GRIMM and ACEITUNO, 2015).

2.3. Intraseasonal Climate Variability

The MJO is the leading global intraseasonal climate variability mode (ZHANG, 2005), with an oscillation period between 30 to 60 days. It is characterized by a dipole in the outgoing longwave radiation (OLR) anomalies in the tropical region, with an eastward propagation (MADDEN and JULIAN, 1971; 1972), indicated by the red arrow in Fig. 7. The convection (subsidence) is indicated by the negative (positive) OLR anomalies that are stronger between the Indian Ocean and the western Pacific Ocean but affect the global tropical convection.

The oscillation evolution is described by eight phases defined according to the Real-time Multivariate MJO (RMM) indices (WHEELER and HENDON, 2004; GOTTSCHALCK et al., 2010). The phases show the enhanced convection over the central-eastern Pacific - America - Africa - Indian Ocean (phases 7, 8, 1, and 2) or the eastern Indian Ocean - Maritime Continent - western Pacific (phases 3, 4, 5, and 6), between 15°S and 15°N (Fig. 7). The MJO is the primary source of intraseasonal climate variability in the tropics due to the convective dipole's eastward progression (KAYANO and KOUSKY, 1999). Furthermore, this climate variability mode also affects the rainfall and circulation anomalies in the extratropics via extratropical teleconnections. Both tropical and extratropical mechanisms are detailed in the following subsection (2.3.1).

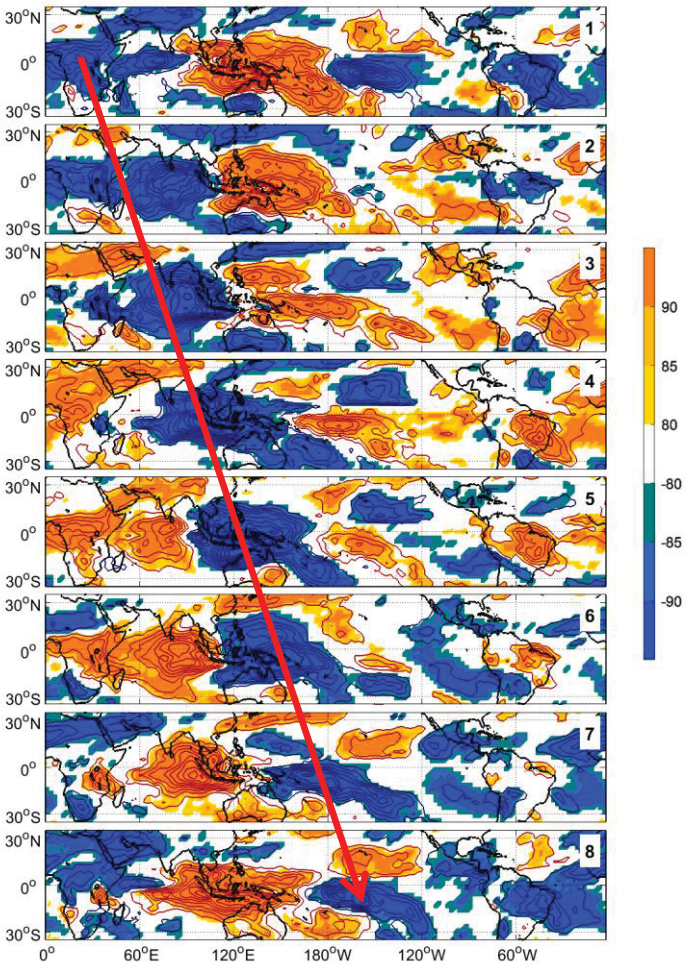

Figure 7: Composite anomalies of OLR in each MJO phase in DJF according to the Wheeler and Hendon (2004) index. Contour interval is 2.5 W/m^2. The color bar indicates confidence levels for OLR anomalies, with signs indicating positive or negative anomalies. The red arrow shows the eastward MJO propagation of the OLR anomalies (Adapted from Grimm, 2019).

Recently, the atmospheric GCMs (AGCMs) have advanced in a more realistic MJO simulation (WEISHEIMER et al., 2014), providing more coherent predictions (WALISER et al., 2003). However, many models still fail to reproduce the MJO intensity, its vertical structure, its eastward propagation, and its associated Kelvin and Rossby equatorial waves (JIANG et al., 2015). Improvements have been suggested as the inclusion of air-sea interaction for the MJO simulation in GCMs, proposed by Jiang et al. (2015). For instance, the air-sea interaction in the Met Office Unified Model (MetUM) increases the MJO intensity and improves its eastward propagation (KLINGAMAN and WOOLNOUGH, 2014a). The atmosphere-ocean coupling in GCMs improves the MJO characteristics, although further explanations remain unclear, being an area of active research (DEMOTT et al., 2015). On the

other hand, most coupled GCMs from the Coupled Model Intercomparison Project phase 5 (CMIP5) still fail in capturing the MJO amplitude and its eastward propagation (AHN et al., 2017).

Previous studies have pointed out the convective parameterization in GCMs as a primary source of errors, particularly the interaction between the convection and circulation, and the horizontal and vertical structure of the diabatic heating associated with MJO (JIANG et al., 2015; KLINGAMAN et al., 2015). Also, the MJO simulation relies on the climatological state in the models since it controls moisture horizontal distribution in the tropics (KLINGAMAN and WOOLNOUGH, 2014a; KIM et al., 2017). The moisture transport by the MJO circulation, combined with the moisture gradients, is an essential energy source to maintain the MJO convection and encourage its eastward propagation.

2.3.1. MJO Dynamical Mechanisms

The diabatic heating due to the latent heat released within the tropical precipitation regions drives the local atmospheric circulation and triggers equatorial waves, which can produce remote response. The heating is equivalent to increasing the fluid's potential temperature (GILL et al., 1979) and shows a maximum value at the non-divergent layer, or 500 hPa (GILL, 1980). The equatorial waves are trapped around the equator, with their amplitude decaying away from the equator. The vertical motion is proportional to the diabatic heating rate, and it is maximum within the convective zones, where there is convergence at low-levels and divergence at high-levels. Hence, the potential energy generated by the diabatic heating is converted into kinetic energy. The divergence term in the vorticity equation leads to cyclonic vorticity at low-levels and anticyclonic at high-levels, increasing the air layer depth (with the increase of the layer´s mean temperature), which is more prominent in the convection region than in the environment around.

The equatorial wave dynamics associated with latent heat released within cumulonimbus clouds encompasses the mutual influence of isolated convective zones with mesoscale and large-scale motions and air-sea interactions. The large-scale convergence makes the environment unstable, favoring deep convection in cumulus clouds. On the other hand, the cumulus clouds supply heating and energy for large-scale systems.

For instance, Gill (1980) shows that symmetric heating over the Indonesian region triggers equatorial Kelvin waves, which propagate eastwards as they are damped, quickly

carrying energy eastwards. The Kelvin waves generate trade winds in the Pacific Ocean, triggering a particular Walker circulation, with ascending motion over the heating region, and subsidence to the east of the upper-level westerlies. Besides the equatorial Kelvin waves, the heating excites planetary waves known as the equatorial Rossby waves, which carry energy westwards towards the Indian Ocean, generating low-level westerlies at the surface.

The MJO global circulation and its eastward propagation are associated with the trapped equatorial waves, specifically with the combination of Kelvin and equatorial Rossby waves, which are known as tropics-tropics teleconnections. The Rossby waves propagate to the west, and the Kelvin waves propagate to the east with a velocity three times faster (GILL, 1980). It explains the longer distance traveled by the Kelvin wave. In the Indian Ocean and western Pacific Ocean, the MJO phase speed is 5 m/s because the SSTs are warmer and the convection reaches its maximum intensity. In the central-eastern Pacific, colder SSTs increase the MJO phase speed to 15 m/s, and the anomalous convection weakens substantially. The Kelvin mode is visible in the low- and upper-level wind and velocity potential anomalies, which show easterly/westerly wind anomalies converging (diverging) to the heating (cooling) or mass sink (source). The equatorial Rossby wave response (LIM and CHANG, 1983) at low-level consists of a pair of cyclonic (anticyclonic) anomalies straddling the equator to the west (east) of the maximum convection (or heating).

According to Matsuno (1966), when a pair mass sink and mass source (heating and cooling) occupies the equatorial region the combination of Kelvin and Rossby equatorial waves at low-levels (850 hPa) produce a tropical quadrupole in the streamfunction anomalies. The zonal wind anomalies strengthen in the equatorial region and point out from the subsidence (or mass source) to the enhanced convection (or mass sink). Moreover, there are interactions with planetary boundary layer's convergence that affect the eastward propagation of the coupled Kelvin and Rossby equatorial waves, and atmospheric instability due to the moist static energy, which is the SST effect on intraseasonal tropical convection. For example, the Kelvin mode's amplitude enhances, and its phase speed reduces over critical SST values (29°C).

The dynamical mechanisms behind the MJO initiation in the Indian Ocean are still not well understood. Many theories, including equatorial waves, convection, and moisture, are elaborated to explain the energy source of the MJO and its eastward propagation (ZHANG, 2005; WANG et al., 2016). One important aspect is that primary MJO events initiating

without a previous MJO are less frequent than successive MJO events (SAKAEDA and ROUNDY, 2016). In a point of view of tropics-tropics teleconnections, if an equatorial Kelvin wave originated during the suppressed convection MJO phase, finds the equatorial Rossby wave response from the subsidence over the Indian Ocean, a new active MJO cycle begins (SEO and KIM, 2003; MASUNAGA, 2007; MALONEY and WOLDING, 2015). On the other hand, tropics-extratropics teleconnections characterized by extratropical Rossby waves triggered from tropical/subtropical heating sources due to previous MJO convection also can be the cause of a new MJO cycle over the Indian Ocean (GRIMM and SILVA DIAS, 1995; SAKAEDA and ROUNDY, 2016; GRIMM, 2019).

Grimm and Silva Dias (1995) firstly suggested that the tropics-extratropics teleconnections produced by the convection over the central-eastern South Pacific enhance the MJO convection on SA, a fact reaffirmed and detailed by Grimm (2019). The SA precipitation anomalies rely on the interplay between the tropics-tropics and tropics-extratropics teleconnections. The former favors the convection in Central America, equatorial SA, and north of CESA. The last favors the appearance of maximum precipitation anomalies over SA, extending the convection to the south of CESA (or the SACZ region). The teleconnection wave train reinforces the SA convection previously produced by the tropics-tropics teleconnections (GRIMM, 2019).

2.3.2. MJO impacts on SA

Some studies have analyzed the MJO impacts on precipitation anomalies and the extreme events in a global context (JONES et al., 2004), and in SA with focus on the equatorial region (SOUZA and AMBRIZZI, 2006), the SACZ (CARVALHO et al., 2004; BORGES et al., 2018), La Plata Basin, and southeast (SE) Brazil (HIRATA and GRIMM, 2015), but also over the entire continent (ALVAREZ et al., 2015; GRIMM, 2019). The MJO strongly influences the position, duration and intensity of the SACZ events (CARVALHO et al., 2004; ALVAREZ et al., 2015; GRIMM, 2019).

The main SA intraseasonal variability OLR mode during the austral summer, showing action centers with opposite signs between CESA and SESA, was first detected by Nogués-Paegle and Mo (1997). Fig. 8 shows the intraseasonal circulation anomalies associated with this dipole pattern (MECHOSO et al., 2005). The left (right) panel shows that the SACZ strengthens (weakens) due to a cyclonic (an anticyclonic) circulation over subtropical SA. The

intraseasonal variability dipole over SA is similar to the SA interannual/interdecadal variability dipole visible in the austral spring and summer (GRIMM, 2011; GRIMM and SABOIA, 2015).

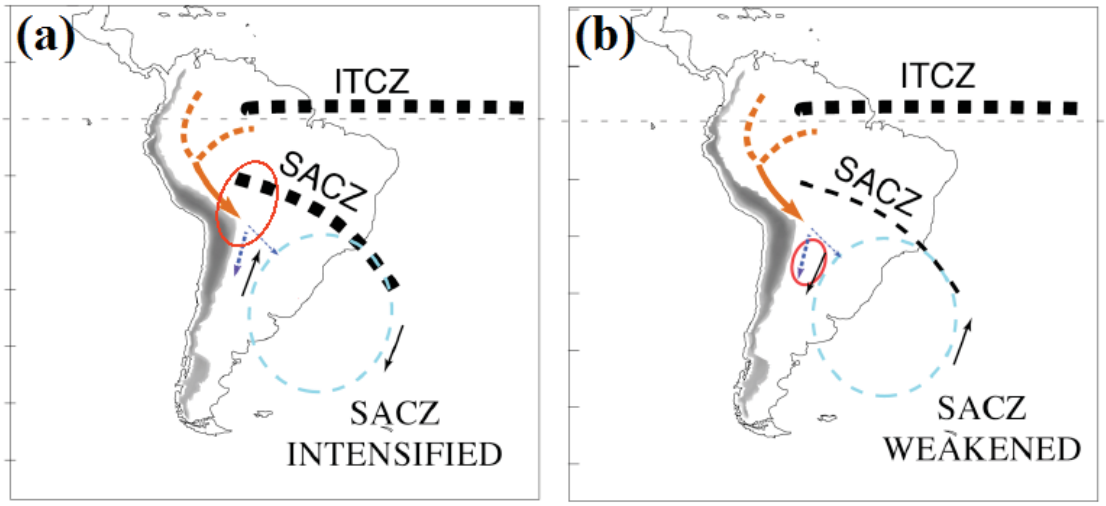

Figure 8: Circulation anomalies associated with the opposite phases of the SA intraseasonal variability dominant mode in DJF, which (a) strengthens or (b) weakens the SACZ. Orange arrows: SA low-level jet. Red circles indicate areas where mesoscale systems are intensified (From Mechoso et al., 2005).

Grimm and Silva Dias (1995) were the first to suggest the association between the MJO anomalous convection in the central-east subtropical South Pacific and the intraseasonal variability dipole (Fig. 8) of the SA rainfall in the MJO time scale, a fact reaffirmed again by Grimm (2019). Extratropical Rossby waves triggered by anomalous MJO convection in the central-east subtropical South Pacific change the upper-level circulation anomalies over SA. In phases 3 and 4 (8 and 1), there is an upper-level anticyclonic (cyclonic) circulation over subtropical SA, which brings moisture flux from Amazon into SESA (CESA), and an upper-level cyclonic (anticyclonic) circulation over the southern tip of SA. Hence, the circulation anomalies during MJO phases 3 and 4 (8 and 1) are similar to those shown in Figs. 5a-8b (Figs. 5b-8a).

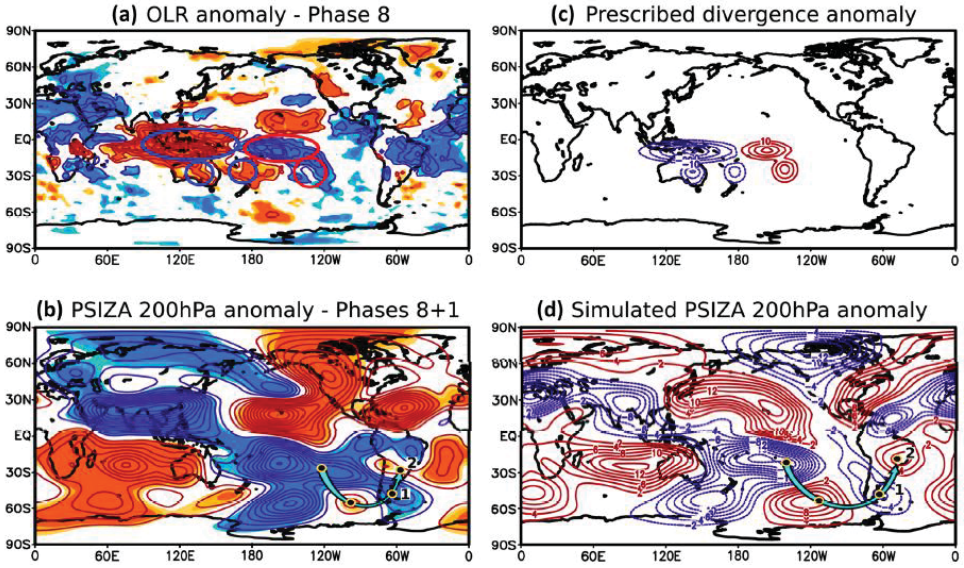

Figure 9: (a) OLR anomalies associated with the MJO phase 8. Contour interval is 2.5 W/m^2. The ellipses indicate the convection anomalies relevant to the response in the tropics and in the SH. (b) 200 hPa streamfunction anomalies combined at phases 8 and 1. Contour interval is $6 \times 10^5\ m^2 s^{-1}$; zero line omitted. (c) 200 hPa positive/negative idealized divergence anomalies prescribed for the simulation of the tropical and SH response. Contour interval is $10 \times 10^{-7}\ s^{-1}$; zero line omitted. (d) Simulated 200 hPa streamfunction anomaly response. Contour interval is $2 \times 10^6\ m^2 s^{-1}$; zero line omitted. From Grimm (2019).

CESA is the region that shows the most substantial MJO impacts, which happens in phase 1 (GRIMM, 2019), with increased precipitation anomalies and frequency of extreme events, which doubles in the SACZ. The peak of maximum precipitation anomalies in SESA is not exactly anti-symmetric, since the maximum positive precipitation anomalies occur in phase 4 rather than phase 5. The frequency of extreme events increases more substantially in phase 3 in this region.

The tropics-tropics teleconnections initiate the positive precipitation anomalies in the north of CESA in phase 8. However, the tropics-extratropics teleconnections are responsible for the most intense positive precipitation anomalies in phase 1. The teleconnection wave train originates in the central-east subtropical South Pacific, associated with the South Pacific Convergence Zone (SPCZ), shifted southeastwards in phase 8 (GRIMM, 2019). The tropics-extratropics teleconnections to SA enter the continent from the extratropics, and its genesis is indicated by the Influence Functions (GRIMM and SILVA DIAS, 1995) (Fig. 9).

The MJO presents indices since 1978, when the OLR started to be computed and monitored. There has been several studies investigating its connection with the interannual variability at global scale and in other regions (HENDON et al., 1999; SLINGO et al., 1999;

ROUNDY et al., 2010; MOON et al., 2011; GHELANI et al., 2017; LEE et al., 2019; TSENG et al., 2020). Shimizu and Ambrizzi (2015) and Shimizu et al. (2017) proposed previous studies about the ENSO-MJO interaction in the SA rainfall and the extremes over equatorial SA. However, they have considered the NDJFM (from November through March) extended period, which difficult to analyze ENSO and MJO impacts since they change between austral spring and summer (Grimm, 2003, 2004; Alvarez et al., 2015). Moreover, their results did not show all MJO phases, which difficult to identify nonlinearities in the impacts, and they showed the combined anomalies of ENSO+MJO, not the analysis of how ENSO modulates the MJO itself and its impacts over SA.

All the literature mentioned above enhanced the knowledge about the interannual (ENSO) and intraseasonal (MJO) climate variability modes and their impacts on SA associated with their teleconnections. However, there is still much to know about the interaction between them and the resulting impacts on SA. For instance, perhaps some specific ENSO phase could alter (strength/weaken) the MJO teleconnections to SA. The ENSO can influence the MJO impacts on SA by modifying the atmospheric basic state through which the perturbations propagate and the MJO itself, by changing its convective anomalies and propagation. These changes can affect the physical mechanisms responsible for the MJO-related rainfall anomalies in SA.

3. Data and methodology

3.1. Datasets

3.1.1. Observational datasets

The rain gauge daily precipitation data used to cover the period between 1979 and 2009 were generate by the Brazilian Water Agency (ANA) and other hydrometeorological institutes from Argentina, Uruguay, Paraguay, and Peru. First of all, the data were verified to detect missing data recorded as zeros, unreal high values, same values registered in stations far away from each other, and unlikely changes in the precipitation regime. The algorithm developed to detect these issues includes many tests based on seasonal climatology and climate variability phases (as EN/LN), besides comparison against neighbor stations (GRIMM and SABOIA, 2015). The code in the Meteorology Laboratory at UFPR used to identify these issues substantially increases the precipitation dataset's consistency. The Liebmann and Allured (2005) gridded precipitation data is used to cover the extreme northern SA. The final daily precipitation dataset is gridded to 1°.

Other atmospheric fields were analyzed as OLR, wind and streamfunction at 850 and 200 hPa, and velocity potential anomalies at 850 hPa, from the following datasets:

(1) Reanalysis NCEP/NCAR (KALNAY et al., 1996), available on https://psl.noaa.gov/data/gridded/data.ncep.reanalysis .html;
(2) Reanalysis ERA-Interim (DEE et al., 2011), which has higher horizontal resolution (0.7° x 0.7°) than the NCEP/NCAR reanalysis (1.8° x 1.8°), available on (https://www.ecmwf.int/en/forecasts/datasets /reanalysis-datasets/erainterim);
(3) OLR dataset (LIEBMANN and SMITH, 1996) from the National Oceanic and Atmospheric Administration (NOAA) / National Center for Atmospheric Research (NCAR), available on https://www.esrl.noaa.gov/psd/data/ gridded/data.interp_OLR.html);

3.1.2. Model output datasets for different MetUM-GOML3 set-ups

Model output data were also used, from simulations with the coupled GCM (CGCM) Met Office Global Ocean Mixed Layer (MetUM-GOML3; HIRONS et al., 2015). The MetUM-GOML3 comprises the MetUM atmospheric model coupled to a simplified one-dimensional ocean model, the Multi-Column *K* Profile Parameterization boundary-layer

model (MC-KPP, based on Large et al. 1994), via the Ocean Atmosphere Sea Ice Soil (OASIS) coupler (Craig et al. 2017). One MC-KPP column is placed under each atmospheric gridpoint. MC-KPP has a 1000 m vertical domain with 100 unevenly spaced points, with the highest vertical resolution near the surface (~1 m) increasing to 25 m below 300 m.

MetUM is used in short (weather forecast prediction) and long (seasonal and subseasonal predictions and climate projections) time scales. Besides, it works as a regional and global model, to investigate atmospheric driving mechanisms. A general description of the model is available in Walters et al. (2019) and https://www.metoffice.gov.uk/research/approach/modelling-systems/unified-model/index.

As MC-KPP simulates only vertical mixing, temperature and salinity corrections are required in climate-length simulations to account for missing ocean dynamics and to adjust for biases in atmospheric surface fluxes (Hirons et al. 2015). The flux-correction technique constrains the mean seasonal cycle of temperature and salinity throughout the ocean column, without damping variability. The corrections are applied throughout each coupled ocean column and at each time step. The corrections are computed from an initial "tendency simulation" in which the MetUM-GOML3 is relaxed towards the target ocean climatology, with a timescale of 15 days. We use the 1980-2009 climatology from the Met Office (UKMO) ocean analysis (Smith and Murphy 2007), with the addition of a repeating ENSO cycle in some simulations. The daily climatology of temperature and salinity corrections is computed from the output of this "tendency simulation", smoothed with a 31-day running mean to remove high-frequency variability, and applied in a subsequent "free simulation" to constrain the basic state temperature and salinity. The free simulation has no relaxation and can be integrated effectively infinitely without drift. We analyse the output of these free simulations.

MetUM-GOML3 differs from MetUM-GOML1 (Hirons et al., 2015) and MetUM-GOML2 (Peatman and Klingaman, 2018) only by the atmospheric GCM: MetUM-GOML3 uses the MetUM Global Atmosphere 7.0 (GA7; Walters et al. 2019), whereas MetUM-GOML1 uses Global Atmosphere 3.0 and GOML2 uses Global Atmosphere 6.0. GA7 has 85 levels in the vertical and a model lid at 85 km. Further details on MetUM-GOML can be found in Hirons et al. (2015) and Peatman and Klingaman (2018).

3.1.2.1. *N96 and N216 simulations*

MetUM-GOML3 has shown improvements in the MJO depiction compared to previous versions, mainly considering the higher horizontal resolution (90 km) proposed in this study. Recent investigations developed in the University of Reading, United Kingdom, have shown that the air-sea interaction and increased spatial resolution are essential to produce a robust MJO in the MetUM model.

Simulations are performed at two horizontal resolutions: 1.875° lon x 1.25° lat, the lower resolution (called N96 in MetUM), with 200 km spacing between each longitude at the equator; and 0.83° lon x 0.56° lat, the higher resolution (called N216), with 90 km spacing between each longitude at the equator. A control MetUM-GOML3 simulation is performed at each resolution, with MC-KPP constrained to the 1980-2009 ocean climatology: 30 years long at N96 and 60 years long at N216. There is no ENSO in these simulations, as MC-KPP does not simulate ocean dynamics. Temperature and salinity corrections for these control simulations are computed from a 10-year tendency simulation at each resolution.

3.1.2.2. *N96-ENSO and N216-ENSO simulations*

To assess the effect of ENSO on the MJO (Section 5), we impose ENSO cycles in MetUM-GOML3 in similar experiments to those described in Klingaman and DeMott (2020). We compute one-year climatologies (May-April, to mimic the "ENSO year") from the Smith and Murphy (2007) dataset for NT, EN, and LN conditions, based on terciles of the Niño 3.4 index in 1980-2009. These climatologies are concatenated (in order EN, LN, NT) to form a three-year composite ENSO cycle. At each resolution, we perform a 31-year tendency simulation, nudging to this three-year repeating ENSO cycle, to derive ten-year climatologies (May-April) of corrections for each ENSO state. Then, at each resolution we perform a 61-year free simulation imposing the corrections to obtain 20 complete 3-year cycles of May-April data. These free simulations provide robust statistics of simulated MJO impacts on SA across many ENSO events. For more information on this technique, refer to Klingaman and DeMott (2020).

Simulations with ENSO are named "N96-ENSO" and "N216-ENSO". N96-ENSO and N216-ENSO are partitioned into EN and LN composites (e.g., N96-EN), according to simulated EN and LN years.

Comparisons between simulations with and without ENSO make visible the ENSO effect on the MJO teleconnections to SA in this model. The simulations are 60 years long, generating robust statistics of the MJO impacts on SA across many simulated ENSO events. Assessments about the MJO impact on SA in N96 and N216 simulations (subsection 3.1.2.1.) are meaningful since we expect that the models employed in the SA subseasonal predictions, reproduce the observed MJO impacts on SA rainfall found without discrimination of ENSO state (GRIMM, 2019). On the other hand, it is noteworthy to analyze the MJO impacts in different ENSO states (EN/LN) (in N96-ENSO and N216-ENSO), in order to refine the skill assessments, and identify regions where the model reproduces the ENSO-MJO impacts on SA rainfall more adequately.

3.2. Methods

3.2.1. Definition of ENSO phases

The Principal Component Analysis (PCA, or EOFs) (JOLLIFFE, 2002) of global SST data is used to classify the observed ENSO states. It reduces the original dataset, which contains many variables, to a set originated by linear combinations from the original variables. Each group is chosen to represent the maximum fraction possible of the data variability (WILKS, 2006). The input data are global monthly SST anomalies (RAYNER et al., 2003), between 1950 and 2009, gridded to 5°. The PCA is based on a correlation matrix, considering the Varimax rotation to obtain orthogonal rotated variability modes. If the modes are unrotated, each mode can contain mixed variations influenced by many physical processes, mainly in the first mode (WILKS, 2006).

The Factor Loadings (FL) and Factor Scores (FS) describe the variability modes' spatial and temporal distribution, respectively. The first mode corresponds to the ENSO phenomenon and explains the largest fraction of variability within the global SST anomalies. From the FS, we have defined the positive (EN) (FS > +0.75), negative (LN) (FS < -0.75), and NT (FS between -0.74 and +0.74) ENSO phases. We have used this threshold to separate active MJO days in each MJO phase during different ENSO states.

As MetUM-GOML3 is forced with a 3-yr repeating ENSO cycle, it is straightforward to partition N96-ENSO and N216-ENSO by terciles of the DJF mean monthly 1.5-meter temperature anomalies in the Niño 3.4 region (averaged 5°S-5°N, 170°-120°W, Fig. 1). From

the 60 DJF periods in the 61-year simulations (Table 1), the warmest twenty seasons are selected as EN, the coldest twenty as LN, and the remaining twenty as NT.

3.2.1 Definition of MJO phases

Climate studies focusing on the MJO usually begin their analyzes in 1979 because the zonally-averaged OLR in the tropics started to be available at the end of 1978. Also, the reanalysis datasets become more reliable in 1979, when satellite observations began. The MJO phases in the observational datasets are defined according to the Wheeler and Hendon (2004) indices, which are available on http://www.bom.gov.au/climate/mjo/graphics/rmm.74toRealtime.txt. The definition includes the following steps.

(1) Multivariate EOF analysis, between 15°S and 15°N, of averaged OLR and zonal wind data at 850 and 200 hPa, after removal of the annual cycle, interannual variability, and normalization by the standard deviation.

(2) Computation of the Real-time Multivariate MJO indices RMM1 and RMM2 through the projection of the OLR and zonal wind data (at 850 and 200 hPa) onto the two first combined EOFs.

(3) Definition of the eight MJO phases, each corresponding to a 45° interval, between 0° and 360°, of the phase angle:

$$\theta = tan^{-1}\left(\frac{RMM2}{RMM1}\right) \quad (1)$$

(4) Inactive MJO periods correspond to the MJO amplitude smaller than one:

$$A = [(RMM1)^2 + (RMM2)^2]^{\frac{1}{2}} < 1 \quad (2)$$

In observations, the OLR dataset used to calculate the RMM indices is from NOAA satellite data (LIEBMANN and SMITH, 1996). The wind reanalysis dataset is from the NCEP/NCAR (KALNAY et al., 1996) in Manuscript 1 and from the ERA-Interim (DEE et al., 2011) in Manuscript 2, to match with the reanalysis dataset used in each manuscript as "observations". The method above is also applied to the OLR and zonal wind obtained from the simulations to evaluate their RMM indices.

3.2.2 Frequency of MJO phases in each ENSO state

The number of days in each MJO phase for all DJF seasons are computed considering the distinct ENSO states (EN, LN, and NT), as well as the percentage of days in each MJO phase and ENSO state.

Probabilities of MJO activity, propagation (transition to the next phase anti-clockwise), and decay (transition to the unit circle) are computed for all RMM phases and each phase separately in Manuscript 2, following Klingaman and Woolnough (2014a) and Klingaman and Woolnough (2014b). We compute the probabilities as follows: (i) Phase frequency: computation of frequency in each active MJO phase. We sum the number of days in which $A > 1$, in each active MJO phase, in DJF. Then, we divide by the total number of days in DJF; (ii) Inactive phase frequency: computation of frequency of inactive MJO. We sum the number of days in which $A < 1$, in DJF. Then, we divide by the total number of days in DJF; (iii) Frequency of decay in each MJO phase: computation of frequency of decay in each active MJO phase. We sum the number of days in DJF in which, in the subsequent day, $A < 1$, for each active MJO phase. Then, we divide by the number of days in which $A > 1$, in each active MJO phase, in DJF; (iv) Frequency of active MJO transitions to the next phase: computation of frequency an active MJO evolves to the next phase. We sum the number of days in DJF in which, in the subsequent day, $A > 1$, for each active MJO phase. Then, we divide by the number of days in which $A > 1$, in each active MJO phase, in DJF.

3.2.3 Daily filtered anomalies

The daily anomalies for observed and simulated data are obtained from the difference between the original data and the mean climatological daily data for each day of the year. The mean climatological daily data are computed for each ENSO state (EN, LN, NT) in order to evaluate the daily anomalies. However, the mean climatology in each ENSO state does not change the mean daily anomalies in each MJO phase evaluated in the composites (following subsection). To obtain the daily climatology, a 31-day running mean is applied to the average calculated for each day, which filters the spurious variance due to the sample size. The anomalies are submitted to the Lanczos Filter (DUCHON, 1979), with 211 weights, which retains the intraseasonal variability in the 20-90 day band. The filtered anomalies are related exclusively to intraseasonal variability, since the filter removes the other climate variability modes (interannual and interdecadal). Only the DJF season is separated after the filtering,

since it is the rainy season in most of SA, with the strongest MJO impacts over the continent (ALVAREZ et al., 2015; GRIMM, 2019).

3.2.4 Composites

Composites of daily anomalies in each MJO phase as in Grimm (2019) are constructed, including new categories of ENSO states (EN, LN, and NT) for each MJO phase. The composites represent the mean anomalies of the atmospheric variables in each MJO phase. For instance, the composite in phase 1 shows the mean anomalies for all DJF days during phase 1. The statistical significance in the composites is assessed with the Student's *t*-test, which tests the difference between means of independent samples, assuming that the samples' variance comes from the same population (WILKS, 2006). The null hypothesis is rejected if the sample means are similar. For instance, if sample 1 is the daily precipitation anomalies during phase 1 in EN, and sample 2 the daily precipitation anomalies for all DJF days between 1979 and 2009, the t value is:

$$t = \frac{x_1 - x_2}{\left[\left(\frac{1}{n_1} + \frac{1}{n_2}\right)\left\{\frac{(n_1 - 1)s_1^2 + (n_2 - 1)s_2^2}{n_1 + n_2 - 2}\right\}\right]^{1/2}} \quad (3)$$

where $x_1 \; e \; x_2$ are the means of sample 1 and sample 2, respectively, $s_1 \; e \; s_2$ are the standard deviations, and $n_1 \; e \; n_2$, the sample size. The number of degrees of freedom is:

$$v = n_1 + n_2 - 2 \quad (4)$$

As series have time dependency, characterized by the autocorrelation coefficient at lag 1, termed ρ_1, due to application of the Lanczos filter, it is necessary to estimate the effective sample size:

$$n = N\left(\frac{1 - \rho_1}{1 + \rho_1}\right) \quad (5)$$

where N is the original sample size and n the effective sample size (WILKS, 2006). The Student's t-test indicates the SA regions with the most significant MJO impacts. The sample 2 in the Student's t-test, was considered as the total DJF days in each ENSO state (EN, LN, NT), which shows the same results as using all DJF days between 1979 and 2009.

3.2.5 Frequency of extreme precipitation events

The frequency of extreme precipitation events is computed with the method proposed by Grimm and Tedeschi (2009):

(i) Computation of the 3-day running means of precipitation, attributing the mean values to the central days;

(ii) Computation of the 90^{th} percentile from the gamma distribution fitted to the daily precipitation data, one percentile for each day of the year, for each grid point;

(iii) Identification of daily extreme events when the daily precipitation exceeds the 90^{th} percentile for the same day.

The daily average number of extreme events (or the probability occurrence of extreme events) in DJF is computed for each MJO phase, in each ENSO state (EN, LN, NT). The same Student's t-test of Equation 3 is using for assessing statistical significance. For instance, now the sample 1 in the Equation 3 is the average number of extreme events in phase 1 in EN, and the sample 2 is the average number of extreme events for all DJF days, between 1979 and 2009. Maps represent, through background colors, the ratio between these two probabilities of extreme events occurrence (or the average number of extreme event days). It shows by which factor the climatology probability of extreme events occurrence changes in each phase of MJO, considering each ENSO state (EN, LN, and NT). For instance, ratio equal 2 means that the frequency of extreme events doubles in some specific region. The effective sample size n is again used because the number of extreme events is based on a 3-day running mean and the daily data present an intrinsic correlation.

4. Manuscript 1

Global ENSO modulation of MJO and its impacts on South America

Laís G. Fernandes [1] and Alice M. Grimm [1,2*]

[1] Postgraduate Program in Water Resources and Environmental Engineering, Federal University of Parana (UFPR), Curitiba, Brazil

[2] Department of Physics, Federal University of Parana (UFPR), Curitiba, Brazil

Laís G. Fernandes ORCID ID: https://orcid.org/0000-0001-7228-6464

Alice M. Grimm ORCID ID: https://orcid.org/0000-0002-9056-4656

[*] *Corresponding author address*: Department of Physics, UFPR, Caixa Postal 19044, CEP 81531-980, Curitiba, Brazil. E-mail: grimm@fisica.ufpr.br

Global ENSO modulation of MJO and its impacts on South America

Laís G. Fernandes [1], and Alice M. Grimm [1,2*]

[1] Postgraduate Program in Water Resources and Environmental Engineering, Federal University of Parana (UFPR), Curitiba, Brazil

[2] Department of Physics, Federal University of Parana (UFPR), Curitiba, Brazil

Abstract

Changes in the Madden-Julian Oscillation (MJO) and its impacts on the South American monsoon season during different El Niño-Southern Oscillation (ENSO) states (El Niño – EN, La Niña – LN, neutral – NT) are analyzed in the global context of the MJO propagating anomalies of convection and circulation. The background ENSO-related anomalies influence several aspects of MJO (relative occurrence of phases, propagation, convection and teleconnections), and therefore modify the MJO impacts on South America (SA), such as precipitation anomalies and frequency of extreme events, as well as their temporal distribution throughout the MJO cycle. Changes include: (1) a delay in the peak of the teleconnections between central-eastern Pacific and SA, from MJOphase8 in LN to MJOphase1 in EN; (2) enhanced MJO convection in the central-east subtropical South Pacific in MJO_{LN}phases7+8 and a little further east in MJO_{EN}phases8+1, in a region efficient in generating tropics-extratropics teleconnections to SA, producing rainfall anomalies over Central-East SA (CESA), especially the South Atlantic Convergence Zone (SACZ), strongest one phase earlier in LN (MJO_{LN}phase8) than in EN (MJO_{EN}phase1), and a little shifted east in the latter than in the former; (3) predominant increase (or reduction) in the frequency of extreme events over densely populated SA regions where both ENSO and MJO contribute in the same direction, with the greatest increase over CESA (including SACZ) during EN, in MJO_{EN}phase1, and over Southeast SA (SESA), in MJO_{EN}phase3; (4) enhanced amplitude in both states, EN and LN, of the first continental intraseasonal dipole-like mode of precipitation variability between CESA and SESA, with maximum opposite anomalies in CESA, the center with largest amplitude, in phases 1 and 4 for EN, and phases 8 and 5 for LN. Significant effects can also be observed in other regions, as northeast and northwest SA.

Keywords: ENSO-MJO Interaction, South American monsoon, Precipitation, Extreme events, Teleconnections.

1 Introduction

Corresponding author address: Department of Physics, UFPR, Caixa Postal 19044, CEP 81531-980, Curitiba, Brazil. E-mail: grimm@fisica.ufpr.br

El Niño-Southern Oscillation (ENSO) and Madden-Julian Oscillation (MJO), respectively the main global interannual and intraseasonal climate variability modes, have been recognized as affecting significantly the rainfall over South America (SA). This influence is exerted through tropics-tropics and tropics-extratropics teleconnections, especially by producing anomalous Walker circulation and Rossby waves (equatorial and extratropical) that affect SA (Grimm and Ambrizzi 2009; Grimm 2019; Cai, McPhaden, Grimm et al. 2020).

The influence of ENSO on the South American climate has been analyzed by many studies, some on a continental scale, others over Brazil or specific regions in SA (e.g., Ropelewski and Halpert 1987; Aceituno 1988; Rao and Hada 1990; Grimm, Ferraz and Gomes 1998; Grimm, Barros and Doyle 2000; Grimm 2003, 2004, 2011). On an annual average, it produces an anomalous precipitation dipole between northeast and southeast SA, with the former (latter) region displaying negative (positive) rainfall anomalies during El Niño episodes. However, the impacts show great seasonal and spatial variation throughout the ENSO cycle (e.g., Grimm 2011). They may also depend on the position of the largest sea surface temperature (SST) anomalies in the equatorial Pacific (Central or East ENSO), although the largest differences between these two different ENSO types happen in austral autumn of the year following the beginning of an event (Tedeschi, Grimm and Cavalcanti 2015; 2016; Cai et al. 2020). ENSO is the main source of interannual climate variability in SA and has been associated with extreme rainfall events, floods and droughts in several regions of the continent (Grimm and Tedeschi 2009; Grimm 2018).

The impacts of the MJO in the austral summer on the South American monsoon season, have been recently analyzed in the global context of the MJO propagating anomalies of convection and circulation, regarding precipitation anomalies, extreme events and the teleconnections that produce and are produced by the South American MJO-related anomalies, besides its possible role in the MJO cycle (Grimm 2019). There are very significant impacts in certain MJO phases, producing average precipitation anomalies that exceed one third of the climatological precipitation in the SA monsoon core region and doubling the frequency of extreme precipitation events in very populated regions. The influence of tropical and extratropical teleconnections and effect of topography were described. Previous studies have shown aspects of the MJO impacts on the South Atlantic Convergence Zone (SACZ, e.g., Paegle, Byerle and Mo 2000; Carvalho, Jones and Liebmann

2004; Hirata and Grimm 2015), on equatorial Brazil (Souza and Ambrizzi 2006), or on the probability of weekly-averaged rainfall exceeding the upper tercile (Alvarez et al. 2015).

Although there are studies showing that the MJO activity can influence ENSO by initiating El Niño events (e.g., Zhang and Gottschalck 2002; Hendon et al. 2007; Pohl and Matthews 2007), here the focus is on the modulation of the intraseasonal MJO and its impacts by the interannual ENSO. Some studies have analyzed the ENSO-driven variations in the characteristics of MJO itself. While some of them suggest that the amplitude of the MJO activity is not significantly affected by ENSO (Slingo et al. 1999; Hendon, Zhang and Glick 1999; Kessler 2001), there are results indicating that El Niño events shift the MJO activity eastward into the central Pacific, expanding the longitudinal domain of its convective activity and changing propagation speed (Fink and Speth 1997; Hendon, Zhang and Glick. 1999; Kessler 2001; Tam and Lau 2005; Wei and Ren 2019). Other studies have analyzed the ENSO-driven modulation of the MJO impacts on several regions and of its teleconnections (Roundy et al. 2010; Moon et al. 2011; Ghelani et al. 2017; Lee et al. 2019; Arcodia, Kirtman and Siqueira 2020; Tseng, Maloney and Barnes 2020). It is convenient to remind that the modulation of the MJO impacts by ENSO can change the characteristics of the MJO itself, especially in regions with stronger MJO-related anomalies, since the modulation of its convection anomalies and teleconnections may modify some MJO characteristics such as its propagation and structure.

The present analysis includes an assessment of the global changes produced by ENSO in the MJO cycle in terms of anomalous convection and circulation, since these are useful to understand the reasons of the changes produced by ENSO in the MJO impacts on SA. Then the investigation addresses the ENSO-driven modulation of the MJO impacts on SA during the peak monsoon season (December-January-February, DJF), which is the rainy season over most of SA and also the season of strongest MJO and its impacts on SA. These impacts are characterized with regard to circulation and convection (OLR) anomalies, precipitation anomalies, frequency of extreme events, and the main MJO-related teleconnections affecting SA. Furthermore, changes in the amplitude of the rainfall response to MJO in the action centers of the dipolar mode representing the largest intraseasonal variance over SA are also assessed.

ENSO can affect the MJO impacts through the modification of the MJO convective anomalies and the atmospheric basic state through which the perturbations propagate, affecting the physical mechanisms by which MJO influences rainfall variability in SA. The

analysis goes beyond the composites of total anomalies in some MJO phases for the three ENSO states, Neutral, El Niño and La Niña (NT, EN, LN), since it isolates the MJO impacts in each of these states.

Although some studies use extended 6 months warm or cold season for analysis, we chose to focus on the peak monsoon season in SA (DJF), not including parts of spring and autumn, since the ENSO impacts on SA in spring, summer and autumn vary significantly. For instance, the precipitation anomalies associated with EN and LN tend to reverse their sign between spring and following summer due to land-atmosphere interactions in Central-East Brazil, a region very affected by MJO in SA (Grimm 2003, 2004; Grimm et al. 2007; Grimm and Zilli 2009). Furthermore, also MJO has different rainfall responses over SA in spring, summer and autumn (e.g., Alvarez et al. 2015). As this may produce significant differences in the ENSO modulation of the MJO-rainfall relationship, it is convenient to focus on a season with more homogeneous behavior regarding rainfall variability related to MJO and ENSO. Another distinctive aspect of the present study is the use of observed daily rainfall gauge data. Gridded precipitation data over SA may underestimate extreme precipitation events (Hirata and Grimm, 2018).

The proposed assessment of the modulation of the MJO impacts on South American by ENSO phases is important for subseasonal prediction (Grimm, Hakoyama and Scheibe 2021) and necessary for validating the models' capability in representing the MJO impacts and its teleconnections in distinct backgrounds associated with ENSO. The low-frequency variability associated with ENSO can modify the seasonal background flow, affecting the distribution, strength and propagation of the intraseasonal oscillation and the extratropical teleconnection patterns. MJO and ENSO do not act independently and composite anomalies associated with their simultaneous action are not explained by simple linear combinations of composites based on the MJO and ENSO separately (as also shown by Roundy et al. 2010; Ghelani et al. 2017). ENSO acts to modulate interannually the intraseasonal response of rainfall due to the MJO and the associated teleconnections. To emphasize the modulation by the ENSO influence on the basic state, we analyze the MJO cycle and its impacts on SA for different ENSO states: NT, EN, and LN, and remove the ENSO-related anomalies from the analyzed composite anomalies.

Section 2 describes the data and methodology used. Section 3 defines the ENSO states and the changes they introduce in the basic state, besides a statistics of the MJO phases in each ENSO state. Section 4 shows the MJO impacts in ENSO NT state, while Section 5

shows them in EN and LN states. Section 6 assesses the ENSO-driven changes in the amplitude of the rainfall response to MJO in the action centers of the dipolar mode representing the largest intraseasonal variance of the summer monsoon precipitation over SA. The summary and conclusions are presented in Section 7.

2 Data and Methodology

2.1 Data

A vast set of rain gauge daily precipitation data between 1979 and 2009, from the Brazilian Water Agency (ANA) and other hydrometeorological institutes in SA, is used in the analysis (Grimm 2019). The data are verified to find aleatory and systematic errors, and tested regarding seasonal climatology, ENSO phases and comparison with neighbor stations (Grimm and Saboia 2015). The Liebmann and Allured (2005) gridded precipitation data is also used to cover the extreme northern SA. Both precipitation datasets are gridded to 1°.

The other atmospheric variables analyzed are the outgoing longwave radiation (OLR) (Liebmann and Smith 1996) and wind data at 850 hPa and 200 hPa from NCEP/NCAR reanalysis (Kalnay et al. 1996), which was chosen for displaying circulation anomalies very consistent with the observed precipitation anomalies in Grimm (2019). Data from ERA-Interim reanalysis (Dee et al. 2011) give very similar results. The wind data are used to compute the zonally asymmetric streamfunction and the velocity potential (Dawson 2016). The streamfunction represents better the rotational wind component in the tropics than the geopotential height, and the velocity potential shows tropical convergence/divergence centers, which are key features of the tropical MJO circulation. The analysis starts at 1979 to avoid biases in the zonally-averaged OLR in the deep tropics (10°N-20°S). Besides, the MJO patterns are better represented in NCEP/NCAR reanalysis after mid-1970s, when satellite observations began to be added (Slingo et al. 1999).

Global sea surface temperature (SST), used to characterize ENSO events, are from HadISST1 data set (Rayner et al. 2003) between 1950 and 2009.

2.2 Methodology

2.2.1 ENSO states

The ENSO states are classified according to the first Principal Component Analysis (PCA) rotated mode of the global SST anomalies in DJF, between 1950 and 2009, gridded to

5°. The PCA is based on a correlation matrix, and the Varimax rotation is used to obtain orthogonal rotated variability modes. The rotation facilitates the separation of modes associated with different physical processes (Richman 1986; Wilks 2006). The factor scores and the factor loadings for the first mode describe, respectively, the temporal evolution and spatial distribution of the ENSO variability mode. Factor scores above (below) 0.75 (-0.75) define positive (negative) ENSO phases, or EN (LN) states. Neutral ENSO state (NT) is defined by factor scores in between.

Using the first global SST variability mode for representing the occurrence of ENSO opposite phases is probably a more complete way of describing the ENSO effect on MJO, since this mode also includes other SST anomalies besides the Niño 3 or Niño 3.4 SST, which are frequently used as indexes to characterize the occurrence of ENSO extreme phases. For instance, the ENSO-related anomalies in the Indian and western Pacific may be relevant for changes in convective activity there, as they occur on top of the already warm temperatures in the warm pool (Hendon, Zhang and Glick 1999). Using this mode as an index represents more completely the global anomalies associated with ENSO.

2.2.2 MJO phases

The MJO phases are defined according to the Wheeler and Hendon (2004) realtime multivariate MJO (RMM) index, computed by multivariate empirical orthogonal function (EOF) analysis of OLR and zonal wind at 850 hPa and 200 hPa averaged between 15°S and 15°N, after subtracting the annual cycle and removing the variability associated with ENSO and lower frequency. The RMM1 and RMM2 indices are evaluated by projection of the OLR and zonal winds at 850 hPa and 200 hPa onto the first combined EOFs.

The amplitude of the MJO ($A = [(RMM1)^2 + (RMM2)^2]^{\frac{1}{2}}$) defines the occurrence of the oscillation: when A ≥ 1 the MJO is active and when A < 1 the MJO is in a neutral phase (inactive). The eight MJO phases are determined by the 45° intervals from 0° to 360° of a phase angle $\theta = \tan^{-1}\left(\frac{RMM2}{RMM1}\right)$. The active MJO days in each MJO phase for DJF are determined for the different ENSO states (EN, LN, NT). Since the number of EN, LN and NT years is not the same, the number of active MJO days in each MJO phase is expressed as a percentage of the total number of days in each ENSO category (Section 3).

2.2.3 Anomaly composites for MJO phases in different ENSO states

The methods for calculating composite anomalies for different MJO phases are the same described in Grimm (2019), with the only difference that each ENSO state (EN, LN, NT) adds a new category of composites. The daily climatological means are calculated smoothing the daily means with a 31-day moving average, which acts as a filter to remove the spurious variance due to the 31-year sample. The daily anomalies are obtained from the difference between the observed data in each day and the daily climatological mean for the same day. These anomalies are submitted to a bandpass Lanczos filter (Duchon 1979) with 211 weights, retaining only the intraseasonal variability in the 20-90 day band. After this filtering, only the anomalies in DJF are used in the composites. The filtered anomalies do not include the direct effect from other climate variability modes (interannual, interdecadal), since we are interested in the ENSO effect on the MJO, and not in the sum of the MJO and ENSO-related anomalies over SA. Therefore, the ENSO-related anomalies are removed from the composite anomalies.

The statistical significance of the composite anomalies is assessed with the Student's t-test used to identify different means from two samples (Wilks 2006). The null hypothesis is rejected if the sample means are different, for instance, the sample mean for MJO phase 1 in EN, and the sample mean from all DJF days in 1979-2009. As the samples may exhibit serial dependence, characterized by the autocorrelation coefficient at lag 1, termed ρ_1, it is necessary to estimate the effective sample size $n = N\left(\frac{1-\rho_1}{1+\rho_1}\right)$, in which N is the original sample size (Wilks 2006).

2.2.4 Frequency of extreme precipitation events

The frequency of extreme precipitation events is also analyzed, since they are related to potential natural disasters over SA, as floods and mudslides in populous regions. The methods are similar to Grimm and Tedeschi (2009), which involve the computation of:

- the 3-day running means of precipitation, which are attributed to the central days, so that persistence is also taken into account;
- the 90th percentile of the gamma distribution adjusted to the daily precipitation data, one value for each day of the year;
- the precipitation percentile in each day of the year, for each grid point.

When this percentile exceeds the 90th percentile, it characterizes an extreme event. The proportion of extreme events (or probability of extreme event occurrence) is computed for each MJO phase and ENSO state, besides the average number of extreme events for all DJF days between 1979 and 2009. The Student's t-test is applied to assess the significance of the difference between these sample means, using the effective sample size mentioned before, since the number of extreme events is evaluated based on a 3-day running mean, and the daily data present autocorrelation. Instead of representing this difference, the ratio between these two probabilities of extreme events occurrence is displayed. It informs by which factor the climatological probability changes in each MJO phase, within each ENSO state. When it is larger (smaller) than 1, it means that the frequency of extreme events increases (decreases) by that factor in a specific MJO-ENSO scenario.

3 ENSO: changes of mean state and frequency of MJO phases

3.1 ENSO states

Figure 1 shows the factor loadings and the factor scores of the first rotated variability mode of global SST anomalies, obtained from PCA. Its temporal evolution and spatial distribution represent the ENSO behavior. The factor loadings show a pattern similar to the canonical ENSO events, with strong SST anomalies over central-eastern equatorial Pacific and opposite anomalies over western Pacific and the Pacific subtropics. Using the factor score threshold 0.75 (-0.75) to classify the positive (negative) ENSO phases resulted in 8 EN, 10 LN and 14 NT years (Table 1) within the 32 years analyzed.

Table 1: Dates of El Niño (EN), La Niña (LN) and neutral (NT) years, obtained from the factor score classification in Figure 1

El Niño (EN)	1982/83, 1986/87, 1991/92, 1994/95, 1997/98, 2002/03, 2006/07, 2009/10
La Niña (LN)	1984/85, 1985/86, 1988/89, 1995/96, 1998/99, 1999/00, 2000/01, 2005/06, 2007/08, 2008/09
Neutral (NT)	1978/79, 1979/80, 1980/81, 1981/82, 1983/84, 1987/88, 1989/90, 1990/91, 1992/93, 1993/94, 1996/97, 2001/02, 2003/04, 2004/05

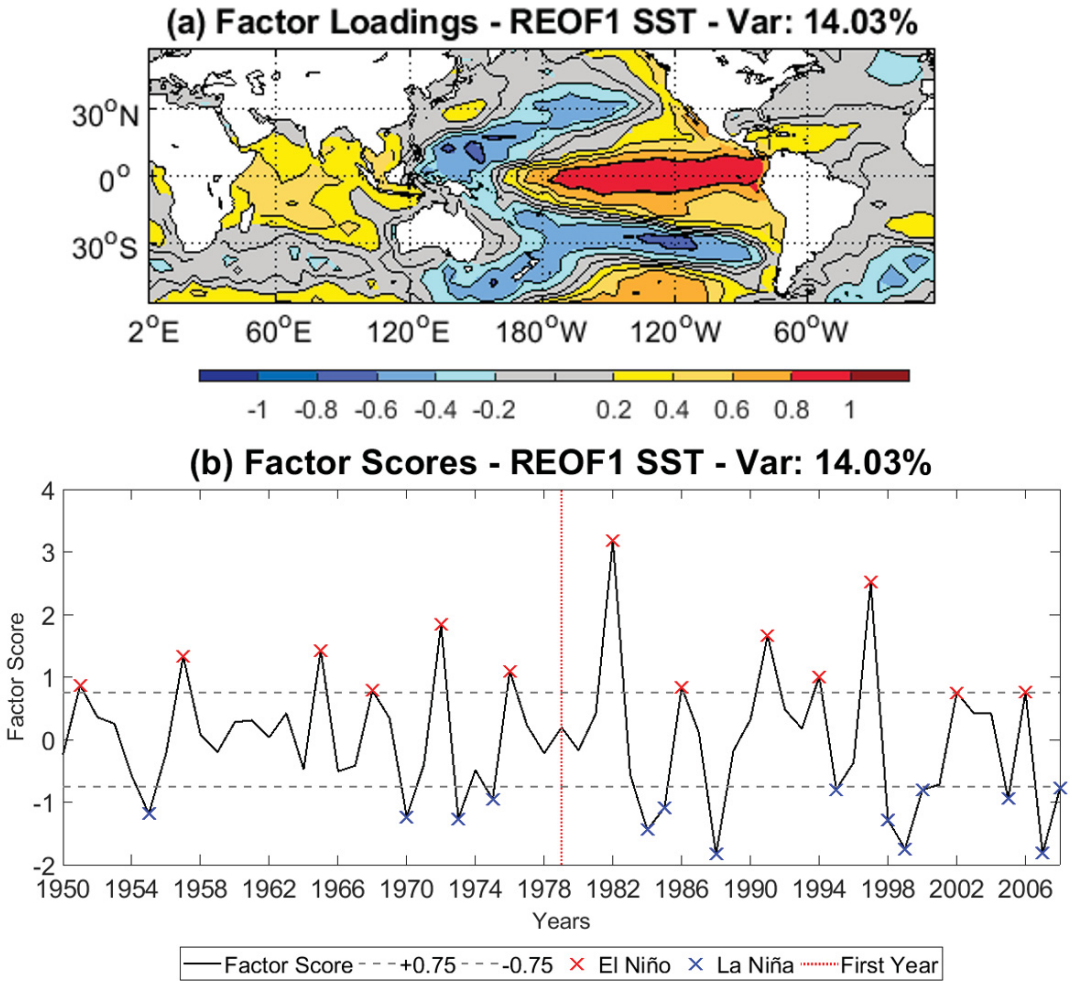

Fig. 1 (a) Factor Loadings and (b) Factor Scores of the first rotated variability mode obtained from PCA analysis of SST anomalies in DJF, representing ENSO. Red (blue) crosses indicate the years classified as EN (LN). The vertical dotted red line indicates the initial date of the present analysis (1979)

The EN (LN) list thus obtained is similar to the strongest events, obtained with the Oceanic Nino Index (ONI), equal or greater than 0.8°C (equal or smaller than –0.8°C). This index is based on the 3-month running mean of SST anomalies in the Niño 3.4 region (5°N-5°S, 120°-170°W). ENSO events using ONI threshold of +/- 0.5°C are listed in https://origin.cpc.ncep.noaa.gov/products/analysis_monitoring/ensostuff/ONI_ v5.php. Therefore, the ENSO classification obtained here is validated by two different methods, with the advantage that the PCA technique extracts the first variability mode taking into account the global SST anomalies, instead of restricting the classification to the Niño 3.4 region. The only event in Table 1 not qualified by the ONI index is the 1985/86 LN, although it is qualified by the Niño 3 index.

This ENSO categorization is used in the next sections, to separate the active MJO days according to the ENSO states.

3.2 ENSO-related changes in the mean state

It is convenient to recapitulate the ways the basic state (or background fields) is changed by the opposite ENSO states in which the MJO is analyzed, since they affect the intensity of MJO convective anomalies, their propagation and the teleconnections they produce. Therefore, to facilitate future discussion, some of the changes in the basic state produced by EN and LN are briefly reviewed and displayed in Fig. 2. Also shown are contours of some composite reference values for each ENSO state (purple lines), such as 28°C SST (indicating the warm pool), 225 W/m^2 OLR (indicating intense convective activity), and 25 m/s U200 contours (indicating strong zonal wind). For reference, the upper left panel shows the climatological average daily precipitation in DJF, with the white grid boxes indicating areas void of data (Fig. 2a). It also shows the main regions cited in the text: Central-east SA (CESA) and Southeast SA (SESA) (pink boxes), and the dipole action centers of the first continental intraseasonal summer precipitation variability mode, analyzed in Section 6 (blue squares). Figures 2b and 2c show the composite daily precipitation anomalies produced by EN and LN.

The ENSO-induced seasonal mean anomalies show approximately opposite signs between EN and LN events. During EN the positive equatorial central-east Pacific SST anomalies extend the warm pool and strong convection eastward to the central equatorial Pacific, while the negative west Pacific SST anomalies weaken the climatological strong convection over the Maritime Continent (Figs. 2d, 2f). Coherently, the equatorial vertical motion anomalies and the equatorial upper-level easterlies are enhanced in the central-east Pacific (Figs. 2h, 2j), and the Southern Hemisphere (SH) subtropical jet is enhanced in subtropical central Pacific (Fig. 2j),

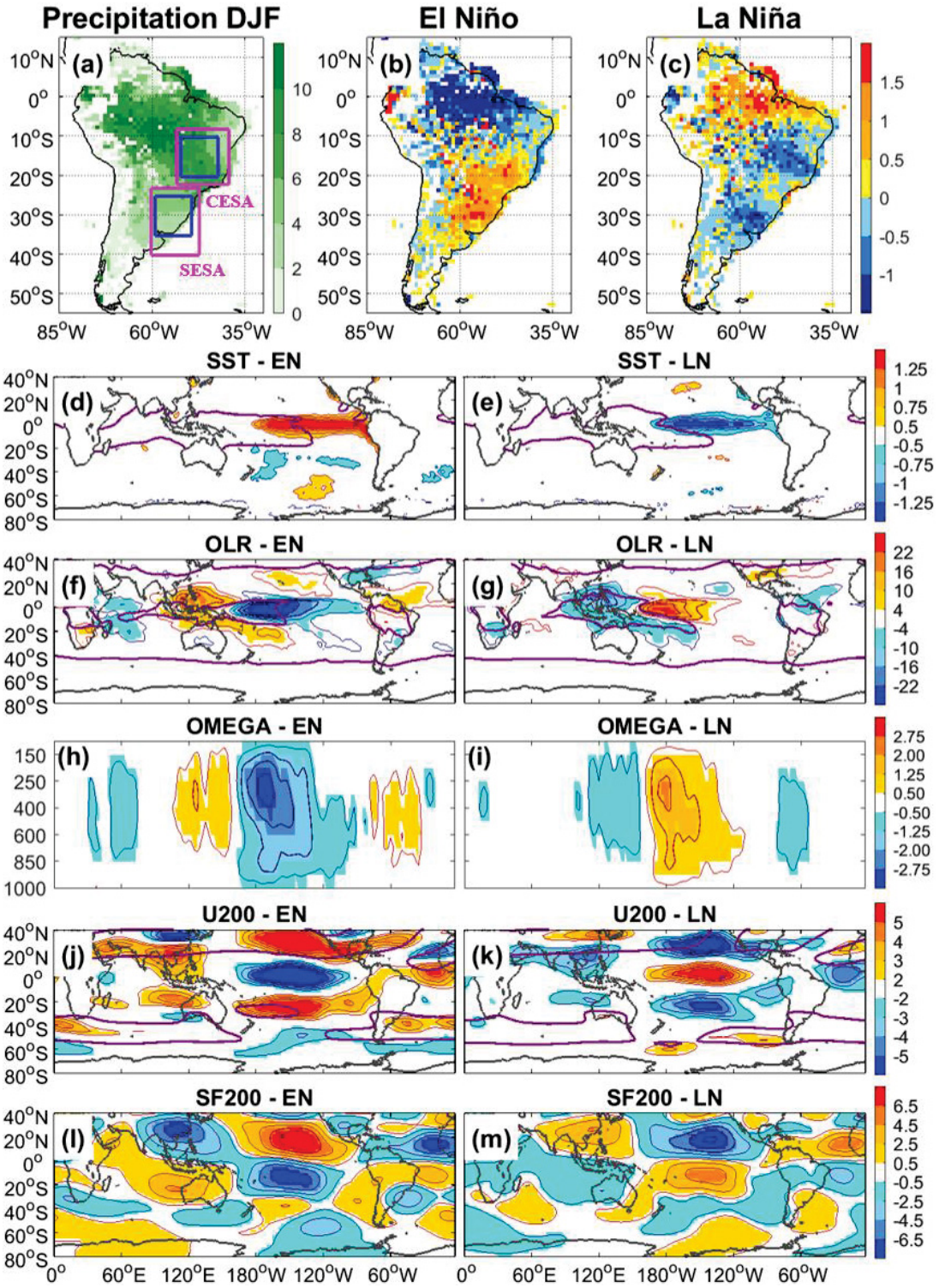

Fig. 2 Top panels: (a) DJF climatological daily precipitation in South America and its anomalies for (b) EN and (c) LN (mm day^{-1}). The first map shows, delimited by pink lines, regions cited in the text, and by blue lines the dipole action centers of the first continental intraseasonal summer precipitation variability mode. The other panels show changes in the DJF basic state produced by (left) El Niño and (right) La Niña: (d,e) SST (°C); (f,g) OLR (Wm^{-2}); (h,i) Longitude-height section of omega averaged over 0-15°S (hPa s^{-1}); (j,k) 200 hPa zonal wind (ms^{-1}); (l,m) 200 hPa eddy streamfunction (10^6 m^2 s^{-1}). Reference values for SST, OLR and U200 for EN and LN are indicated by purple contours (see text)

while an anomalous anticyclonic pair straddles the equator in central Pacific and a cyclonic/anticyclonic upper-level circulation pair covers subtropical SA (Fig. 2l). On the other hand, during LN the warm pool expands its latitudinal extent over the West Pacific, but reduces its longitudinal domain in the equatorial Pacific, shifting it to the southern subtropics (Fig. 2e). The convection in the West Pacific and the Maritime Continent is enhanced and also shifted to the subtropics of the Central Pacific, while the equatorial convection is weakened (Fig. 2g), coherent with the equatorial vertical motion anomalies (Fig. 2i). The climatological upper-level equatorial westerlies in central eastern Pacific are enhanced (Fig. 2k), while an anomalous cyclonic pair straddles the equator in central Pacific and an anticyclonic/cyclonic upper-level circulation pair covers subtropical SA (Fig. 2m). The longitude-height section of omega (Figs. 2h, 2i) is coherent with the SST and convection (OLR) anomalies, displaying in EN (LN) enhanced ascending motion (subsidence) in central-east Pacific and opposite anomalies over SA, western Pacific and eastern Indian Ocean.

It is interesting to point out that for both, EN and LN, the convection is enhanced in the subtropical central-east South Pacific, although with less intensity and more to the east during EN (Figs. 2f, 2g). The features in Fig. 2 are consistent with the interannual variability of the South Pacific Convergence Zone (SPCZ) associated with ENSO (Vincent et al. 2009; Lorrey et al. 2012). In general, during EN the SPCZ is north and east of its average position and surface pressure is lower in the central South Pacific. During LN, the SPCZ usually lies south and west of its average position, consistent with a warmer SST in this region. However, an important aspect is that in both cases, EN and LN, there is more rainfall in the central subtropical South Pacific than during NT years, in EN a little more to the east than in LN.

3.3 Statistical relationship between MJO phases and ENSO states

The most numerous active MJO phases in DJF are 7 and 3 (Fig. 3a), which represent 17% and 16% of the total active MJO days, respectively (Fig. 3b). However, when the MJO phases are separated with respect to the ENSO states (Figs. 3c, 3d), it is possible to note that the higher occurrence of the MJO phase 3 is more noticeable in EN (20%), although it is also frequent in the other ENSO states, while the frequency of the MJO phase 7 is relatively greater in NT (20%) and LN (16%). It seems that the background ENSO-related anomalies influence the relative occurrence of MJO phases with similar patterns of circulation / convection anomalies. Considering the strongest anomalies of Walker circulation and convection over the equatorial eastern Indian Ocean/western Pacific Ocean and central Pacific

Ocean, there are similarities between ENSO states (Fig. 2) and some MJO phases in DJF (Fig. 4, and Figs. 2, 3 in Grimm 2019). Phases 8, 1, 2, 3, which are relatively more frequent in EN (Fig. 3d), share some common features with EN: suppressed convection over the equatorial eastern Indian Ocean, Maritime Continent/western Pacific, and subtropical central-west South Pacific, while enhanced convection predominates over the equatorial central Pacific. On the other hand, phases 5, 6, 7, which are relatively more frequent in LN (Fig. 3d), display common features with LN. The MJO phases that are relatively most frequent in category NT (LN) have the second highest relative frequency in LN (NT) (Fig. 3d), consistent with the fact that anomalous LN features approximately intensify NT features.

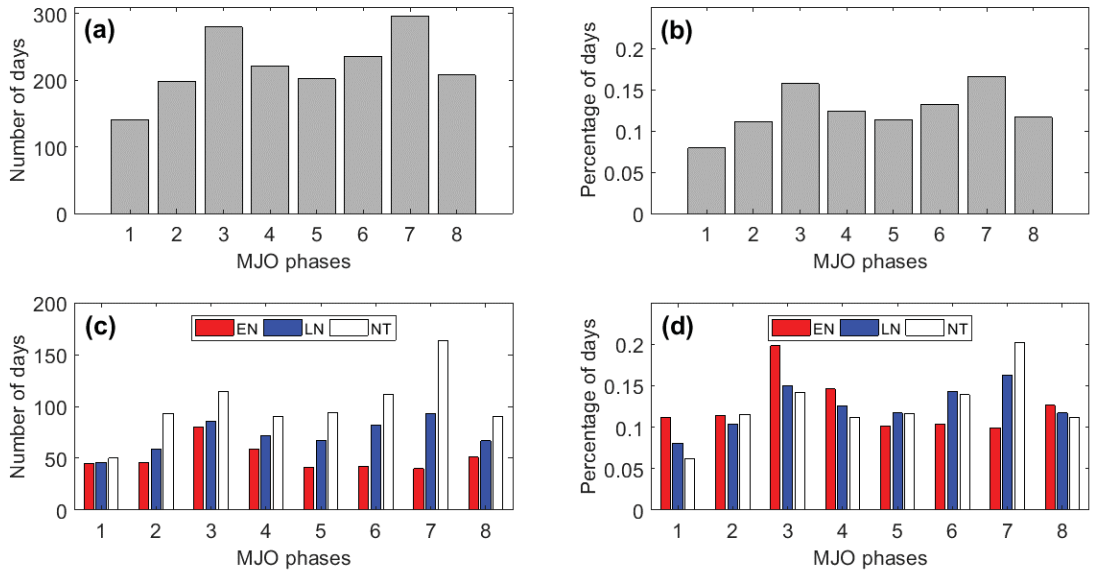

Fig. 3 (a) Number of MJO active days in each MJO phase, and (b) the respective percentage of MJO active days in each MJO phase. (c) Number of active MJO days in each ENSO state, and (d) the respective percentage, considering the total of days in each ENSO phase (red for EN, blue for LN, and white for NT)

Although this study does not investigate in detail the reasons of differences in the frequency of MJO phases during different ENSO states, it is possible to hypothesize that the mean circulation and convection changes during the different states of ENSO alter the MJO related convection anomalies and moisture distribution over the equatorial region. This can change the intensity and propagation of the MJO patterns, favoring the intensity and frequency of certain MJO phases during the ENSO state with background patterns most similar to those MJO phases.

There have been analyzed 2790 days in 31 DJF seasons. From these days, 1782 (64%) were active MJO days. From the active MJO days, 404 occurred in EN, 572 in LN, and 806 in

NT years. Hence, there are more active MJO days in NT years because they are more numerous (14) than EN (7) and LN (10) years. Consequently, the samples used in the composites for NT years are larger than for EN and LN years, although the number of MJO active days per year is not very different for the different ENSO states: 57.6 (NT), 57.7 (EN) and 57.2 (LN). Therefore, the year-to-year variations of MJO activity seem to be unrelated to ENSO (Slingo et al. 1999; Hendon, Zhang and Glick 1999). Notwithstanding, there are variations of the anomalous convection and circulation patterns associated with MJO. For instance, during EN the anomalous equatorial zonal winds and convection tend to increase near and east of the Date Line and decrease in the far western Pacific (Gutzler 1991; Fink and Speth 1997). Changes in the MJO-related global patterns of convection, circulation and precipitation produced by different ENSO states are described in the next sections, with more focus on SA.

4 MJO impacts in ENSO neutral state

4.1 Global anomaly patterns associated with MJO in neutral years

Basic background on the MJO dynamical mechanisms, the global evolution of the MJO tropical convection and associated circulation, and the description of the MJO impacts on SA are provided in Grimm (2019). Therefore, this information will not be duplicated here, where the focus is on the ENSO modulation of MJO characteristics and impacts.

Although the global mean evolution of MJO and its impacts is well known, it is not exactly equal to the MJO evolution during ENSO NT state, since there are some nonlinear effects of ENSO on MJO that are not smoothed out in a mean over all ENSO states. Figure 4, which shows the low-level velocity potential and wind, besides OLR anomalies, for years with no ENSO signal (NT state), displays some differences with respect to Figures 2 and 3 of Grimm (2019), computed for all years in the same period. For instance, anomalous convection over the climatological SACZ in phase 1 and winds in some places are stronger in the composites including all years, indicating that the EN and LN effects do not just combine linearly with the MJO effects. Therefore, a separate analysis for different ENSO states can be helpful in terms of subseasonal prediction and validation of models.

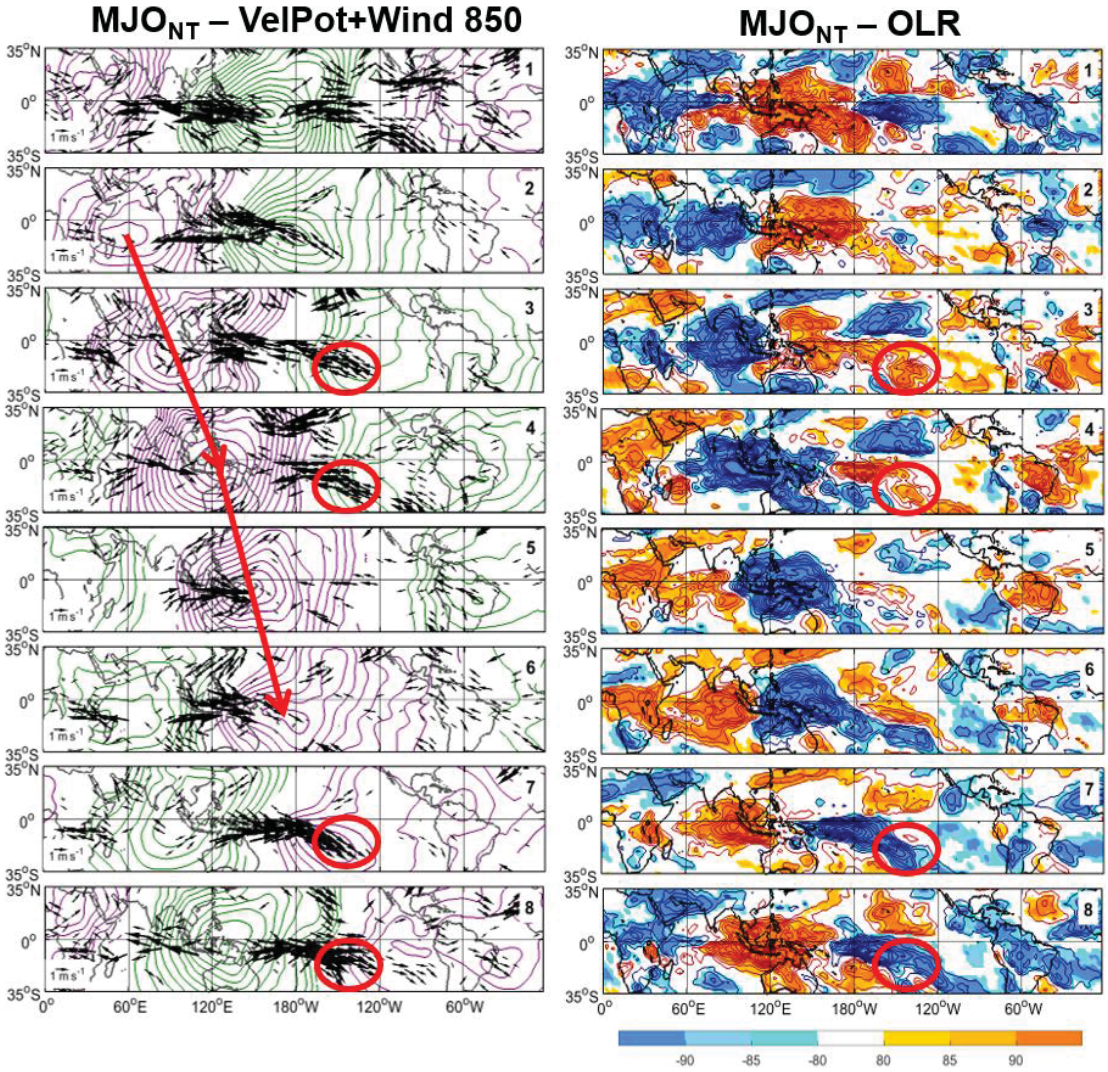

Fig. 4 (Left) Composite anomalies of 850 hPa winds and velocity potential filtered in the 20–90 day band for each MJO phase during the austral summer in NT years. Contour interval is 2×10^5 m^2s^{-1}. Velocity potential negative anomalies are in green and positive anomalies are in purple, with their maximum absolute values indicating centers of anomalous divergence and convergence, respectively. Only wind anomalies (ms^{-1}) with confidence levels better than 80% are shown. (Right) Composite anomalies of OLR in each MJO phase for austral summer in NT years. Contour interval is 2.5 W/m^2. The color bar indicates confidence levels for OLR anomalies, with signs indicating positive or negative anomalies.

The general MJO patterns during an ENSO NT state are broadly consistent with the observational analysis in Grimm (2019) considering all years of the period. Notwithstanding, focusing on the phases with most extensive impacts on SA, phases 1 and 4, it is possible to detect differences. Comparing Fig. 4 (right column) with Figs. 2 and 3 in Grimm (2019), it is possible to see that in MJO_{NT}phase1 the OLR anomalies over the climatological SACZ position crossing the Brazilian coast are approximately -5.0 W/m^2, while in the all-year

composite in Grimm (2019) they reach -10.0 W/m^2. In the equatorial NE Brazil the MJO$_{NT}$phase1 displays anomalous OLR -10.0 W/m^2, while the all-year composite reaches -12.5 W/m^2. On the other hand, in the middle of CESA the difference is small. In SESA, the MJO$_{NT}$phase1 presents some significant anomalies, reaching -7.5 W/m^2, while in the all-year composite they are weaker and of opposite sign. In phase 4 there are no great differences in CESA, but in SESA the negative anomalies in MJO$_{NT}$phase4 reach -10.0 W/m^2, while in the all-year composite they are below -5.0 W/m^2.

Figure 4 (left column) displays the anomalous MJO propagating low-level divergence and convergence centers and wind anomalies for NT state, for the sake of comparison with corresponding maps for EN and LN states. There are some low-level wind divergence/convergence features highlighted in subtropical central-east South Pacific, which are related with upper-level anomalous convergence/divergence anomalies (indicated by tropical OLR anomalies in Fig. 4 (right column)). They are efficient in producing the extratropical Rossby wave trains (indicated by curved arrows in Fig. 5) associated with precipitation anomalies over SA, according to Grimm (2019). There is a lag (around one phase) between the appearance of the upper-level divergence and the establishment of the wave train over SA.

Also the streamfunction anomalies at 200 hPa (Fig. 5, right column) show differences between anomaly composites for MJO phases in NT years and in all years. Grimm (2019) pointed the importance of extratropical teleconnections in contributing to the strongest and most extensive positive (negative) precipitation anomalies over SA in phase 1 (phases 4-5) by creating a cyclonic (anticyclonic) anomaly over the subtropical continent that favored these anomalies over CESA (and opposite ones over SESA). While in MJO$_{NT}$phase1 this cyclonic center over subtropical SA responsible for the enhanced convection anomalies over CESA (and SACZ) is weak and not significant (Fig. 5, 200 hPa), in the all-year composite it is significant (Fig. 5 of Grimm 2019). Also in the Northern Hemisphere (NH) the extratropical teleconnections are affected: for instance, while in MJO$_{NT}$phase7 the extratropical teleconnection over North Pacific / North America is very weak (Fig. 5, 200 hPa), it is stronger and significant in the all-year composite (Fig. 5 of Grimm 2019). At low levels, the cyclonic anomaly over the extratropical North Pacific extends further north and in the equatorial Pacific further east in the all-years composite (Fig. 4 of Grimm 2019).

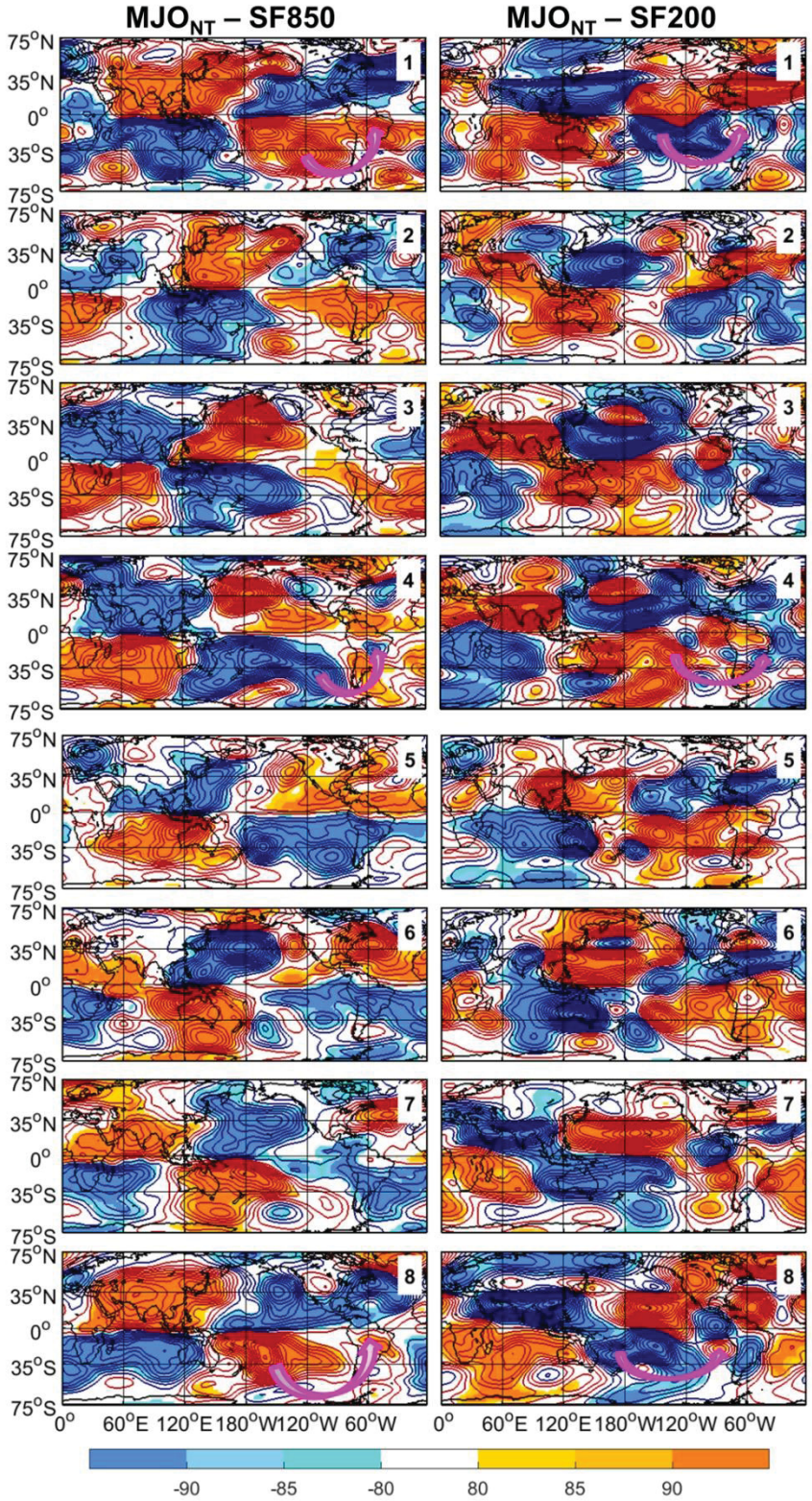

Fig. 5 Composite anomalies of (left) 850 hPa and (right) 200 hPa eddy streamfunction filtered in the 20-90 day band, for each MJO phase during the austral summer (DJF) in NT years. Contour interval is 3×10^5 m^2s^{-1} at 850 hPa and 6×10^5 m^2s^{-1} at 200 hPa; zero line is omitted. The color bar indicates confidence levels, with signs indicating positive or negative anomalies.

These global composites for MJO_{NT} phases will be mentioned later again, as a reference for the MJO composites in EN and LN states.

4.2 Precipitation and its extremes over SA associated with MJO in neutral years

Figure 6 shows the MJO-related precipitation behavior in SA for NT years. While the main anomaly patterns for precipitation and frequency of extreme events for NT years maintain the general characteristics of the all-years composites in Grimm (2019), some details are different, consistently with the differences already pointed out in OLR and circulation anomalies. In phase 1 of the all-years composite there are strong and significant precipitation anomalies over the climatological SACZ and a little south of it (Fig. 7 of Grimm 2019). Also the frequency of extreme events is significantly increased in this region (Fig. 8 of Grimm 2019). The composites for MJO_{NT}phases8+1 show weaker or no significant positive anomalies in these regions, since they are shifted northward, to central CESA and north of it (Fig. 6), as also shown in OLR negative anomalies (Fig. 4). The same happens with less intensity to opposite anomalies in MJO_{NT}phases4+5.

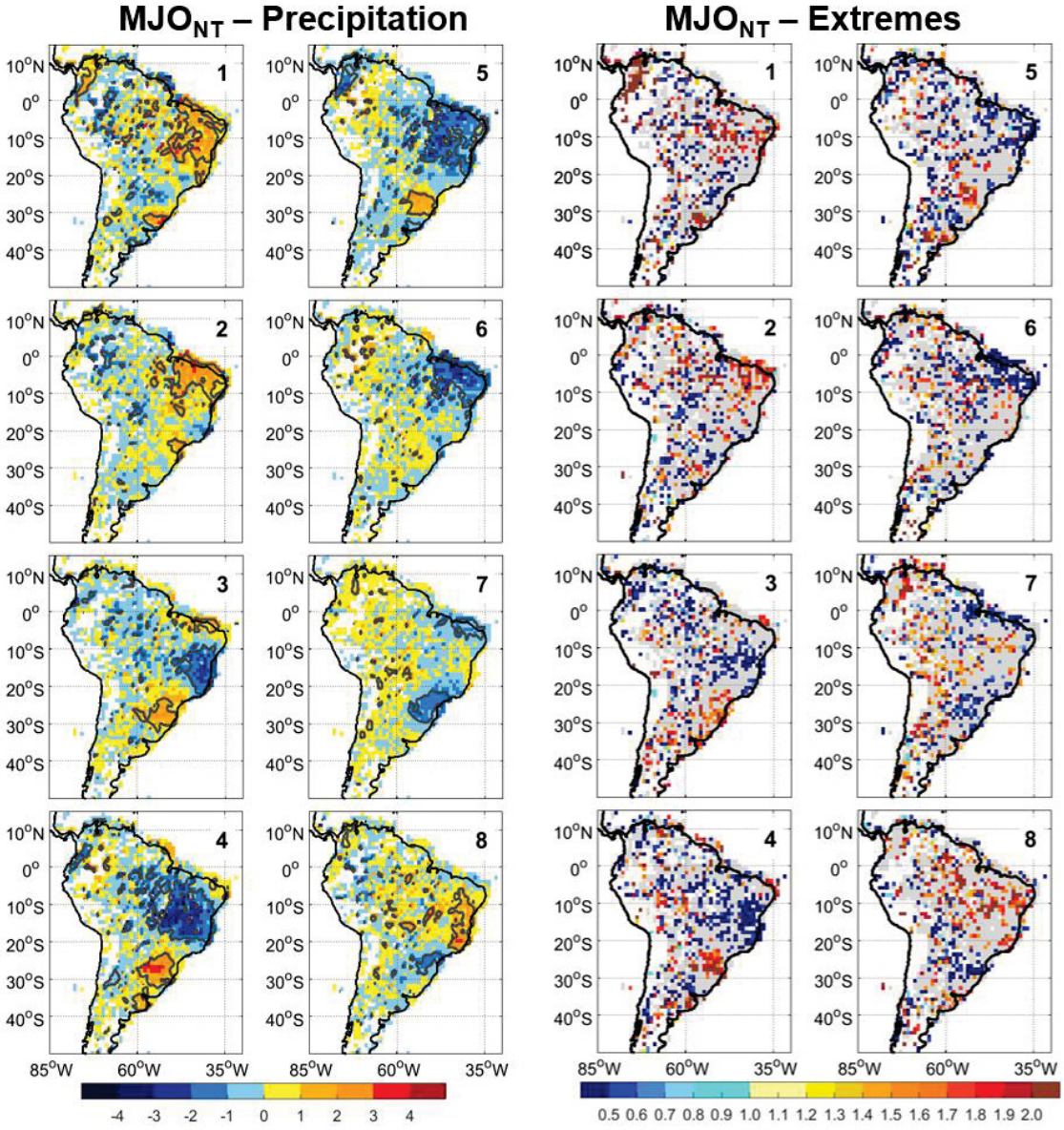

Fig. 6 (Left) Composite anomalies of daily precipitation rate (color bar, mm day−1) filtered in the 20–90 day band, for each MJO phase during the austral summer (DJF) in NT years. Gray lines delimit anomalies with confidence levels better than 85%. (Right) Ratio between the probability of extreme precipitation events in each of the MJO phases in NT years and the mean probability for DJF. Only ratios corresponding to statistically significant difference between the probability of occurrence for each MJO phase and the mean probability with confidence levels better than 85% are shown in color. Grey indicates regions with lower confidence level, and white indicates regions void of observed gauge daily data

5 MJO impacts during El Niño and La Niña states

5.1 Global anomaly patterns associated with MJO in EN and LN years

5.1.1 Why expect ENSO to influence MJO and its impacts?

There are several reasons to expect that the ENSO-related changes in the background state influence MJO and its impacts on SA. The background changes produced by opposite ENSO states in the SST warm pool, tropical convection and circulation (Fig. 2) are able to change not only the frequency of MJO phases, as already shown, but also the intensity, position, size, and propagation of the MJO most notable convection features, as well as the associated circulation and teleconnections (e.g., Fink and Speth 1997; Moon, Wang and Ha 2011). For instance, the characteristic equatorial MJO eastward propagating convective anomalies are coupled with a pair of large-scale anomalous Walker cells, which can be affected by the Walker circulation changes produced by opposite ENSO states (Figs. 2h, 2i). Besides, the region with strongest MJO-related anomalous convection (subsidence), in phases 4 and 5 (8 and 1), over the Maritime Continent, around 130°E (Fig. 4 for NT years, and Fig. 2 of Grimm 2019), is also a region with strong ENSO-related convection anomalies in the West Pacific (Figs. 2f, 2g). Another region with significant MJO and ENSO-related convection anomalies is Central-East Pacific, around and east of the Date Line, where the MJO-related anomalies are of much interest to SA, since in their eastward propagation they start to weaken in this region and shift southeastward, entering a region where anomalous convection is very efficient in producing teleconnections to SA (Grimm 2019).

5.1.2 Influence of EN and LN states on MJO-related convection and circulation

The next figures show the MJO global anomalous convection and circulation patterns (Figures 7, 8, 9, 10) during EN and LN states.

When the MJO-related anomalies are favored by oceanic and atmospheric background ENSO-related changes (Fig. 2), their intensity tends to be enhanced. Figures 7 and 8 show that in MJO phases 8, 1, 2, 3 reduced convection and low-level anomalous divergence over the eastern Indian Ocean-Maritime Continent/west Pacific and enhanced convection and low-level anomalous convergence in central Pacific are more intensified on the equatorial belt during EN than during LN. This is consistent with the EN prevalent anomalous subsidence over the former regions and dominant anomalous convection over the latter (Fig. 2 and Figs. 7 and 8). It is more visible in the anomalous OLR field (Fig. 8), and for phases 8 and 1. On the

other hand, during MJO phases 5, 6, 7 the low-level anomalous convergence and enhanced convection over the eastern Indian Ocean-Maritime Continent/west Pacific and low-level anomalous divergence and subsidence in central Pacific are more enhanced during LN, because these anomalies are also prevalent in LN (Fig. 2 and Figs. 7 and 8).

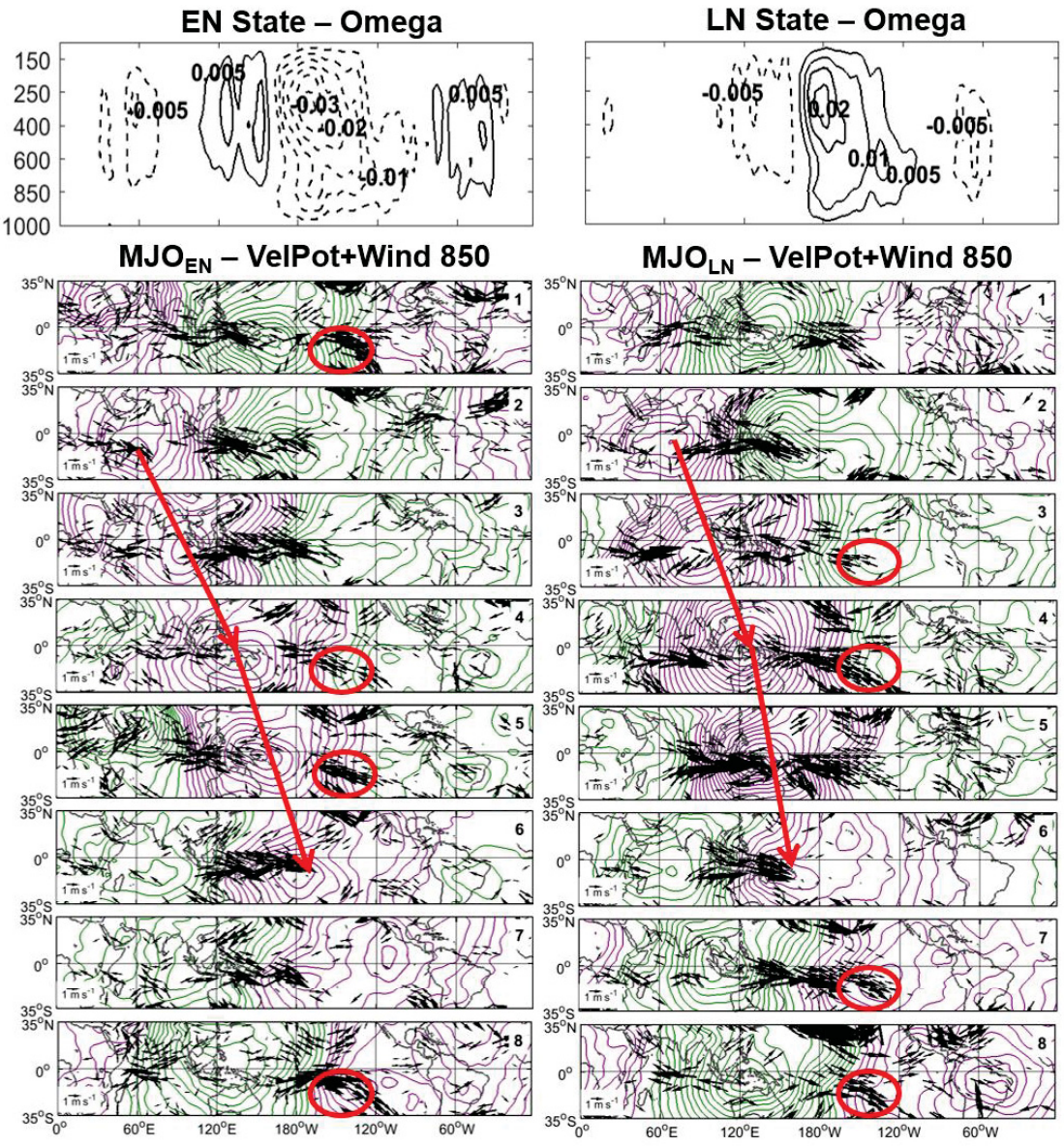

Fig. 7 (Upper panels) Composite anomalies of omega (Pa s^{-1}) for (left panel) EN state and (right panel) LN state. (Other panels) Composite anomalies of 850 hPa winds and velocity potential filtered in the 20–90 day band for each MJO phase during the austral summer in (left) EN state and (right) LN state. Contour interval is 2×10^5 m^2s^{-1}. Velocity potential negative anomalies are in green and positive anomalies are in purple, with their maximum absolute values indicating centers of anomalous divergence and convergence, respectively. Only wind anomalies (ms^{-1}) with confidence levels better than 80% are shown

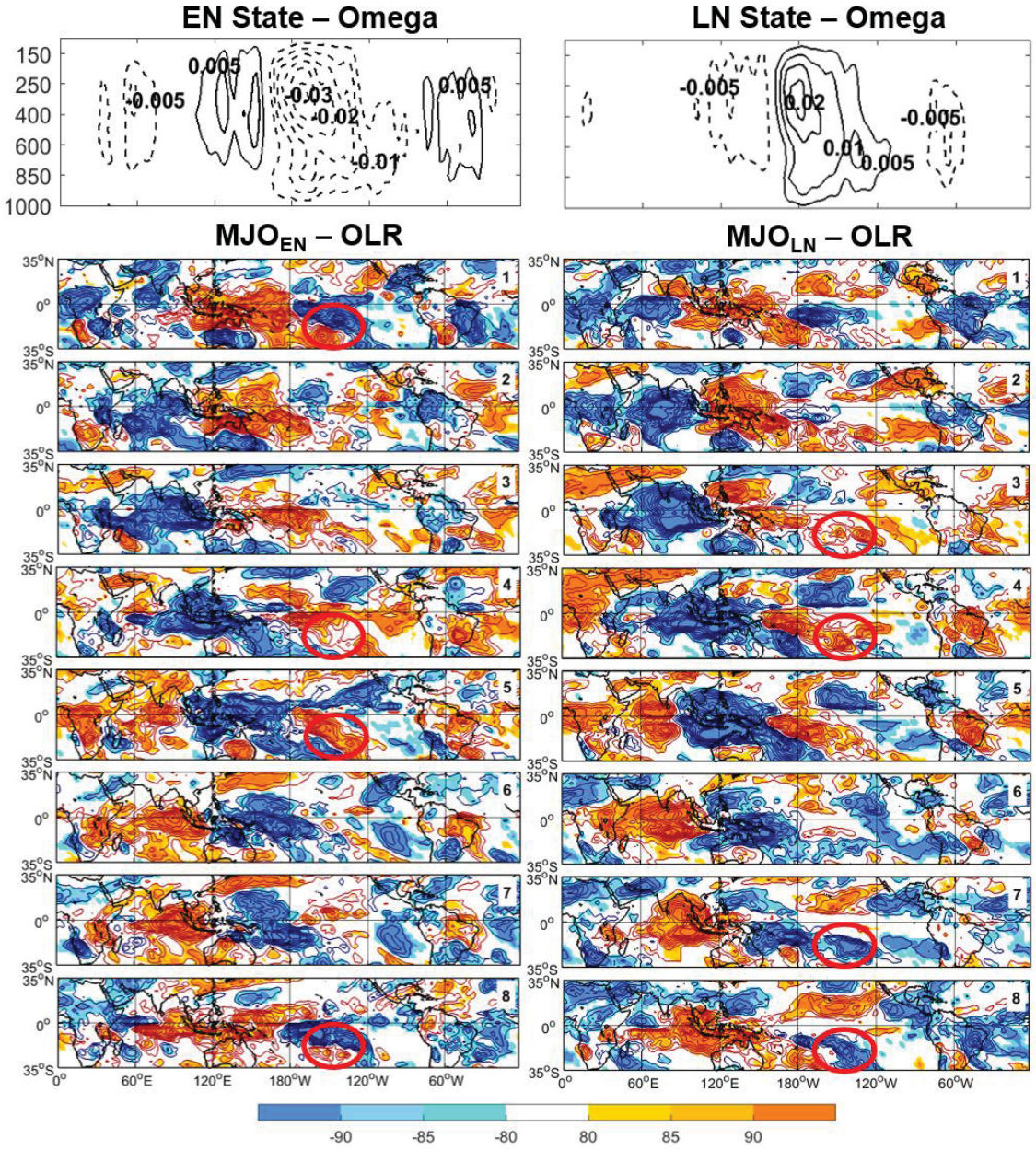

Fig. 8 (Upper panels) Composite anomalies of omega (Pa s^{-1}) for (left panel) EN state and (right panel) LN state. (Other panels) Composite anomalies of OLR filtered in the 20–90 day band for each MJO phase during the austral summer in (left) EN state and (right) LN state. Contour interval is 2.5 W/m^2. The color bar indicates confidence levels, with signs indicating positive or negative anomalies

The position and size of MJO-related anomalies is also altered by ENSO opposite states. For instance, when the MJO enhanced convection is near/over the Maritime Continent, in phases 4, 5, and 6, it is more intense and extensive during LN than EN (Fig. 8), since ascending motion is enhanced in this region and the warm pool occupies a larger latitudinal extension (Figs. 2e, 2i). On the other hand, the MJO equatorial convection reaches and crosses the Date Line already in phases 5 and 6 during EN, favored by the SST and Walker

circulation background conditions in this ENSO state (Fig. 2), while in NT state this only occurs in phases 6 and 7 (Figs. 4 and 8). This is consistent with the eastward shift of MJO activity during EN events reported by Hendon, Zhang and Glick (1999). On the other hand, in LN state the MJO convection is suppressed in equatorial central-east Pacific in phases 7 and 8 (Figs. 4 and 8), but appears in subtropical central-east South Pacific, which is coherent with the background in this ENSO state. As in LN the equatorial SST in the Pacific is colder east of the Date Line and the subsidence is enhanced, the tropical enhanced convection is shifted south of the equator (Fig. 2g).

In another example, when the equatorial MJO enhanced convection crosses the Date Line (phases 6+7), and MJO and EN (LN) anomalies have same (opposite) sign east of the Date Line, the MJO-related low-level divergence (and subsidence) over the equatorial northeast SA is enhanced (weakened) in MJO_{EN}phases6+7 (MJO_{LN}phases6+7) and the enhanced convection (or negative OLR) in MJO_{EN}phases8+1+2 (MJO_{LN}phases8+1+2) is weakened (increased) in this region (Fig. 8) with respect to NT state (Fig. 4). This is consistent with the effects of ENSO on the equatorial northeast SA (or eastern Amazon), shown in the upper panels of Fig. 2. In NT years, without EN or LN influence, the MJO-related subsidence observed in phases 4+5+6 over northeastern SA weakens in MJO_{NT}phases6+7+8, when the MJO convection crosses the Date Line (Fig. 4). However, there is EN-related background subsidence over northeastern SA during EN years due to the EN-related enhanced convection in central-east equatorial Pacific (Fig. 2d, 2f, 2h), which is further increased in MJO phases 6+7+8 (Fig. 8, left column). Therefore, during MJO_{EN}phases6+7+8, the subsidence over northeastern SA stays longer, since the positive OLR anomalies are much stronger in MJO_{EN}phases6+7, and the negative ones are weaker during MJO_{EN}phases8+1 than during the NT state. During the LN state, the opposite occurs (cf. Figs. 4 and 8).

5.1.3 Influence of EN and LN states on MJO propagation and teleconnections

Propagation speeds of MJO features are approximately indicated by the inclination of the arrows in Figs. 4 and 7, but are also visible in the displacement of the convection and circulation anomalies (Figs. 4, 5, 8, 9 and 10), especially in the low-level streamfunction quadrupoles, associated with the Rossby and Kelvin wave responses to the dipole of mass sink and source (heating and cooling) over the equatorial region (Matsuno 1966; reviews in Zhang 2005; Grimm 2019).

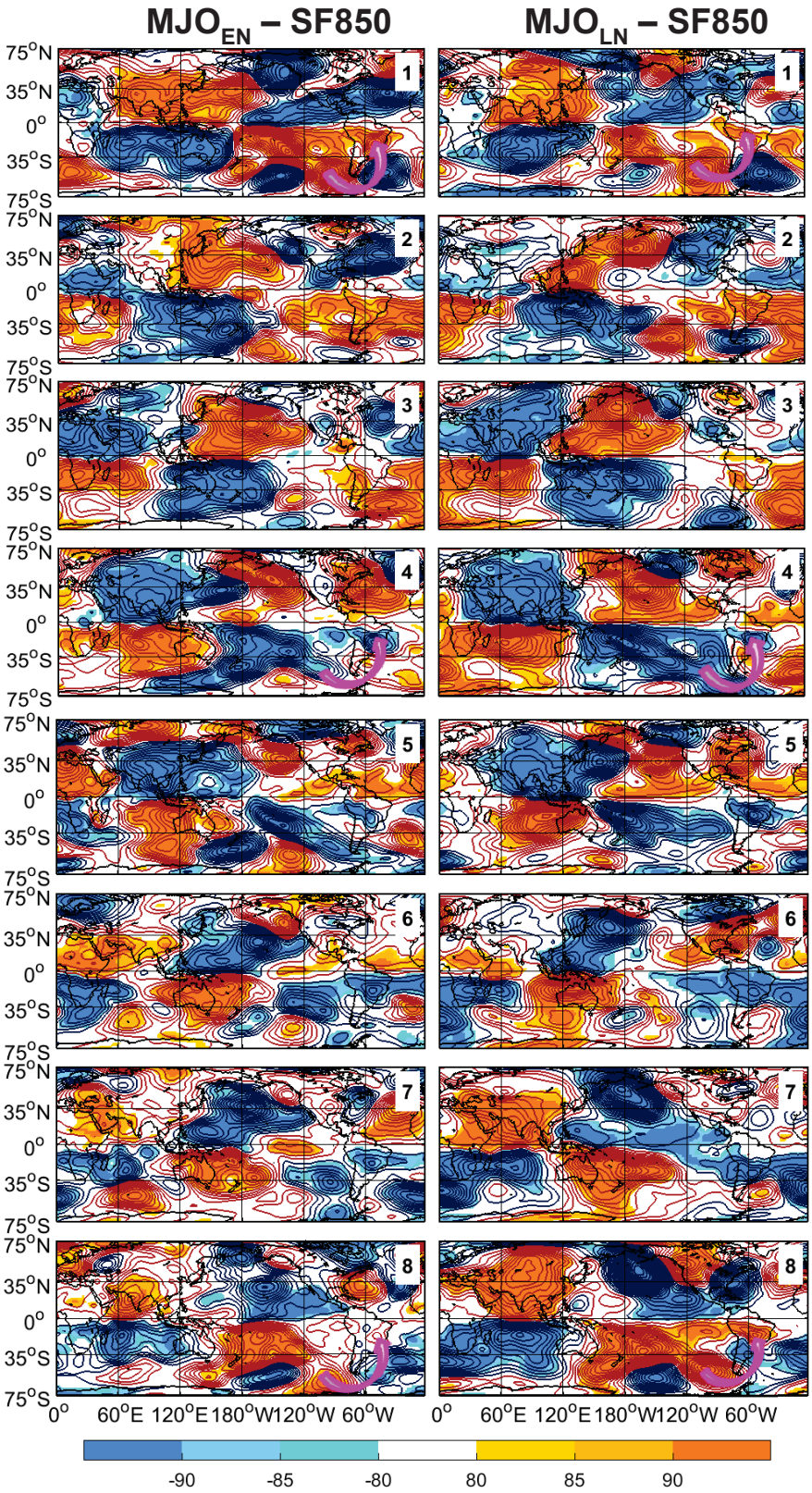

Fig. 9 Composite anomalies of 850 hPa streamfunction filtered in the 20-90 day band, for each MJO phase during the austral summer (DJF) in (left) EN state and (right) LN state. Contour interval is 3×10^5 m^2s^{-1}; zero line is omitted. The color bar indicates confidence levels, with signs indicating positive or negative anomalies

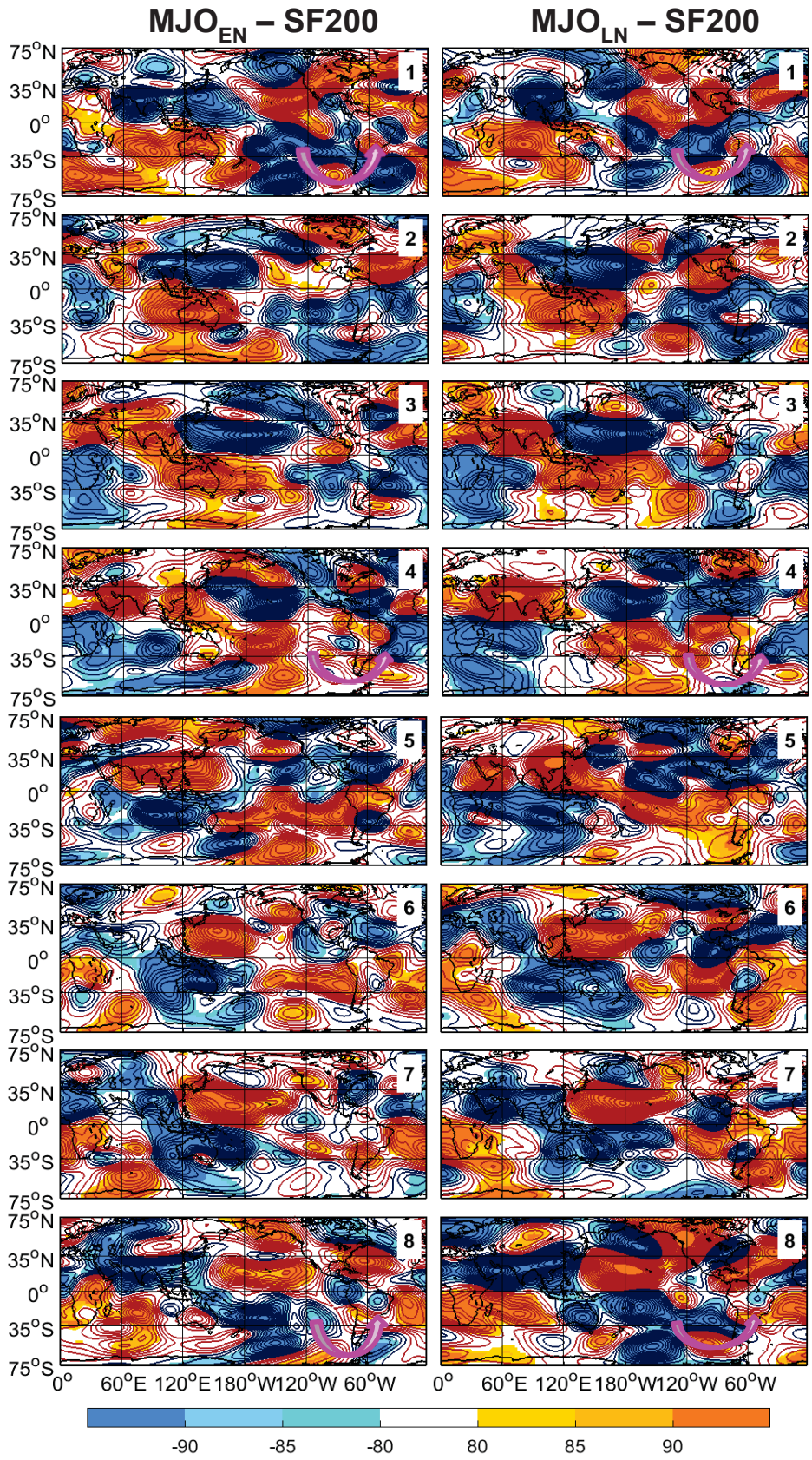

Fig. 10 Composite anomalies of 200 hPa streamfunction filtered in the 20-90 day band, for each MJO phase during the austral summer (DJF) in (left) EN state and (right) LN state. Contour interval is 6×10^5 m^2s^{-1}; zero line is omitted. The color bar indicates confidence levels, with signs indicating positive or negative anomalies

The circulation anomalies are presented to facilitate discussion of the teleconnections and precipitation anomalies over SA observed in each ENSO phase. The equatorial propagation characteristics are also summarized in Fig. 11.

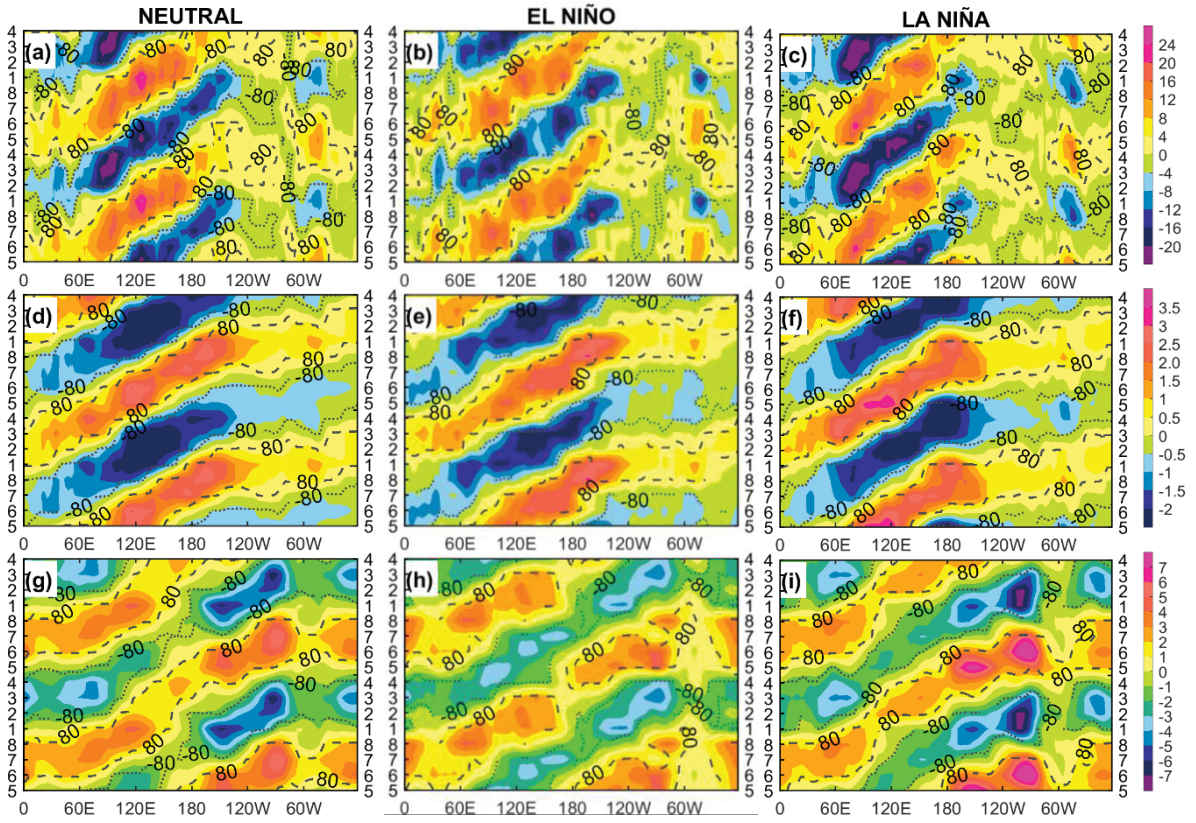

Fig. 11 (a, b, c) MJO phase-longitude Hovmoller diagrams of OLR anomalies (Wm^{-2}); (d, e, f) zonal wind anomalies at 850 hPa (ms^{-1}), and (g, h, i) 200 hPa (ms^{-1}), averaged over 0°-15°S, during the austral summer. Left panels for NT, middle panels for EN and right panels for LN. The dotted and dashed lines delimit the significant values with confidence levels better than 80%

Since higher (lower) phase propagation speed is expected for weaker (stronger) convection (Zhang 2005; Pohl and Matthews 2007), the stronger and more extensive anomalous convection over the Maritime Continent in phase 5 during LN is consistent with much slower eastward propagation over this region (Figs. 7, 8). Besides, there is great weakening of the convection when it moves from over the Maritime Continent to the western Pacific, which is consistent with the barrier effect of the Maritime Continent (Zhang and Ling 2017). On the other hand, during EN, the anomalous convection over the Maritime Continent is weaker and does not reduce much when it moves from the Maritime Continent to the western Pacific Ocean, with higher propagation speed (Fig. 7). It crosses the Date Line in phase 6, extending further eastward in the equatorial band than in LN state (Figs. 7, 8), since

the equatorial warm pool is extended further eastward during EN than during LN (Figs. 2d, 2e). On the other hand, during LN there is a quicker eastward propagation of anomalous convection on the subtropical central-eastern South Pacific, from phase 6 to 7, probably favored by the warm pool features during LN (Fig. 2e).

After the MJO convection crosses the Maritime Continent and approaches the Date Line (phase 6) (Figs. 4, 7, 8), the propagation speed over the climatologically colder ocean waters shows considerable differences between EN and LN. During EN, although stronger equatorial anomalous convection extends eastward of the Date Line, there is little propagation from phase 6 to 7 (Figs. 7, 8), and this aspect also appears in the circulation anomalies, since there is little propagation of the equatorial streamfunction anomalies over the Pacific between these phases (Figs. 9, 10). On the other hand, during LN there is no enhanced convection on the equatorial central-east Pacific, but subtropical convection is extended eastward from phase 6 to 7 into central-east South Pacific (Fig. 8). The equatorial wind perturbation propagates faster eastward and the low-level convergence and westerly winds are already strong over the eastern Pacific and SA in phase 8, while during EN they reach the maximum in phase 1 (Figs. 7, 9, 11). The same is true for the upper-level easterlies, which are stronger and propagate eastward faster over the central-east Pacific during LN than during EN (Figs. 10, 11), favoring stronger and earlier equatorial convection in the Western Hemisphere, over SA, Atlantic Ocean and Africa in phases 8 through 1 during LN.

Therefore, the tropics-tropics teleconnection between the Pacific and SA during LN state, favoring the enhancement of precipitation in northeast SA and tropical CESA, is already established in MJO_{LN}phase8, but during EN state is only well established in MJO_{EN}phase1 (Figs. 7, 8, 9, 10). The differences between EN and LN in the propagation of the equatorial convection anomalies across the Date Line and in the propagation of the zonal wind signal is also clear in the Hovmoller diagrams (Fig. 11). This difference between propagation speeds in the Western Hemisphere is consistent with the reduction (increase) of the MJO phase velocity over warmer (colder) SSTs and associated with stronger (weaker) convection (Zhang 2005). Also the subtropical low-level wind convergence and associated OLR anomalies in central-east South Pacific, which are important for the extratropical teleconnection with SA, are first established in phase 7 (8) during LN (EN) (Figs. 7, 8). This subtropical convection is an important aspect related to the extratropical teleconnection between the central-east Pacific and SA (indicated schematically by the curved arrows in Figs. 5, 9, 10), since the associated upper-level divergence in this region is shown to be very efficient in triggering such

teleconnection (Grimm and Silva Dias, 1995; Grimm, 2019). This region is indicated by the ellipses in Figs. 4, 7, 8. The anomalous convection in it is stronger in MJO_{EN}phases8+1 and MJO_{LN}phases7+8 (Figure 8) than in MJO_{NT}phases8+1 (Figure 4). The Influence Functions of Fig. 11 in Grimm (2019) shows that the upper-level divergence anomalies in the subtropics of the central-east South Pacific lead to a teleconnection pattern that produces an anticyclonic-cyclonic circulation anomaly over the extratropics-subtropics of SA that enhances precipitation in CESA in the phases indicated above. The subtropical cyclone favors moisture flux from the Amazon into CESA (and the SACZ), where there is moisture convergence, and divergence of moisture flux from the middle/lower Parana/La Plata Basin (SESA), tending to form a convective dipole between CESA and SESA (Grimm 2019).

The extratropical teleconnection pattern is approximately indicated on the streamfunction patterns of Figs. 5, 9 and 10, in phases 8 and 1, and, with opposite sign in phase 4. It is more visible at 200 hPa, and at 850 hPa it is only indicated on the barotropic actions centers. The MJO phase in which it is more clearly established varies with the ENSO state. While it is still developing in MJO_{EN}phase8 (and strongest at MJO_{EN}phase1), it is already fully established in MJO_{LN}phase8 (Figs. 9 and 10). In NT years it is more consistently established with the precipitation anomalies over CESA in phase 1 (Fig. 5). The maximum enhancement of the pair extratropical anticyclone-subtropical cyclone over SA, and the strongest negative OLR anomalies in CESA, produced by the cyclonic circulation, happens earlier in the MJO cycle during LN (MJO_{LN}phase8) with respect to EN (MJO_{EN}phase1) and NT (MJO_{NT}phase1). However, the highest impact on the southern edge of the SACZ in LN occurs in MJO_{LN}phase1, associated with the subtropical cyclonic anomaly a little displaced westward, with respect to MJO_{EN}phase1. The same advancement during LN happens to the propagation of velocity potential anomalies (Fig. 7), as well as to anomalies of precipitation and frequency of extreme events, as will be detailed later.

It is interesting to point out that there are some similar effects of EN and LN states, compared to NT state, regarding the MJO-related extratropical teleconnection from subtropical central-east South Pacific to SA. Taking phase 1 as reference (although phase 8 could also be used for the LN state), there are great differences between the MJO circulation anomalies over the continent in NT years and those in EN and LN years (cf. Fig. 5 and Figs. 9 and 10). While EN and LN years show a strong anomalous pair extratropical anticyclone-subtropical cyclone over SA (Figs. 9 and 10), in NT years it is weaker and shifted northwestward, as is also the extratropical teleconnection (Fig. 5). This teleconnection fades

in MJO phase 2 (Figs. 5, 10), due to the reduction of convection in that subtropical region in South Pacific (Figs. 4, 8), weakening the positive (negative) precipitation anomalies in CESA (SESA) (next section).

Besides the similarity over SA, the circulation anomalies during MJO_{EN}phase1 and MJO_{LN}phase1 are also similar over the South Atlantic Ocean (Fig. 10). One of the notable features is the strong anomalous barotropic anticyclonic circulation near the southeastern coast of SA, which merges with the extratropical anticyclone over southern SA that is part of the teleconnection pattern from the Pacific. This does not appear in MJO_{NT}phase1 (Fig. 5), since it is probably partially produced by the enhanced convection in the southern edge of the SACZ during EN and LN MJO phase 1 (Figs. 4, 8).

Thus far, emphasis has been put on the circulation and convection anomalies associated with the most extensive enhanced convection over SA, in phases 8 through 2, especially phases 8 and 1. However, in phases 3 through 6, especially phases 4 and 5, the anomalous convection displays approximately opposite signs compared to that in phases 8 and 1 (Figs. 4, 8). The convection in the equatorial central Pacific and in the subtropical central-east South Pacific, important for the teleconnection towards SA, is suppressed, and the precipitation dipole is reversed on SA, enhancing the positive (negative) OLR anomalies in CESA (SESA) (Figs. 4, 8). Approximately opposite anomaly patterns have been shown in all ENSO states between phases8+1 and phases4+5, in convection (Figs. 4, 6, 8, 11) and circulation anomalies (Figs. 5, 9, 10), suggesting that the region of subsidence in the subtropical central-east South Pacific can trigger tropics-extratropics teleconnections, suppressing convection in the SACZ. This teleconnection is schematically represented in phase 4 (Figs. 5, 9, 10), when the wave train is best defined, especially in NT state, but in case of EN the subtropical anticyclonic circulation is strongest in phase 5 (Fig. 10).

In phases 8 and 1 the enhanced convection is strongest and shifted east in subtropical central-east South Pacific in EN with respect to LN, and therefore the teleconnection pattern towards SA is also shifted east with respect to LN, and so is the enhanced convection over SA (Figs. 8, 10) and precipitation (next section). On the other hand, enhanced subsidence over central-east subtropical South Pacific is stronger and shifted east in LN with respect to EN in phases 3 and 4, and therefore this teleconnection pattern is stronger and slightly shifted eastward, and so is anomalous convection over SA (Figs. 8, 10). It also starts earlier, in phase 3, while in EN it is more visible in phase 4, as is more clearly seen at 850 hPa (Fig. 9).

The MJO most intense and extensive dry anomalies over SA (which peak in phases 4 and 5) take longer to be established and last longer in EN state (Fig. 8). The tropical teleconnection is slower and in EN it takes longer for the enhanced convection to move to the subtropical central-east South Pacific and reverse the convection dipole over SA, because of the slower propagation between phases 6 and 7 over the Pacific, mentioned before. During these phases in EN state positive OLR anomalies still predominate in subtropical central-east South Pacific, while in LN already negative anomalies predominate (Fig. 8). Therefore, the teleconnection pattern leading to an inverse dipole over SA starts being established in phase 8 in EN, while in this phase it is already fully established in LN. Furthermore, in the equatorial belt the enhanced subsidence during EN over the northern part of CESA also contributes to extend the dry anomalies over SA. Hence, the interannual circulation anomalies extend (shorten) the intraseasonal circulation anomalies over SA in EN (LN) during the MJO phases with dryness in CESA.

Extratropical teleconnection patterns over other regions of the globe also change between EN and LN states, as shown by Moon, Wang and Ha (2011), especially in the Northern Hemisphere, where the winter basic state favors the extratropical teleconnections triggered by tropical convection. For instance, in extratropical North Pacific, North America and North Atlantic there are noticeable differences between EN and LN in phases 7, 8, 1, such as the anomalies over northern Pacific and eastern US (Figs. 9 and 10). Yet during phases 8 and 1 the differences in Southern Hemisphere are not great, especially in the Western Hemisphere, probably because the regions with more influence on the extratropical teleconnection reaching SA are in the subtropics of central-east South Pacific and anomalous MJO convection is not that different between EN and LN in those regions.

Some features pointed out thus far in the equatorial belt are visible and summarized in the MJO Hovmoller diagrams for the three ENSO states. The quicker and more eastward propagation of the OLR anomalies over the Indian Ocean/western Pacific in EN (Fig. 11b) than LN (Fig. 11c) is clearly visible in the lower slope of the OLR diagram for EN in this range of longitudes (between 60°E-120°E). The equatorial convection stays longer a little east of the Date Line during EN (phases 6 and 7), which is coherent with the anomalous Walker circulation with ascending motion over this region, and then extends eastward (and southward) till 120°W (cf. Figs. 11b and 8 left). Yet in LN the equatorial propagation of convection is slower till a little west of the Date Line (although it extends southeastward in the subtropics) (cf. Figs. 11c and 8 right). Therefore, the equatorial propagation of anomalous

convection ends near the Date Line in LN, also coherent with the Walker circulation basic state in this category. The equatorial enhanced convection only reappears over equatorial SA in phases 8-1-2, and is stronger during LN than EN (cf. Figs.11b, 11c and 8). The MJO eastward propagation over colder SSTs in the central-eastern equatorial Pacific is better represented in the upper-level zonal winds (Figs. 11g, 11h, 11i). They have a higher phase velocity since they are associated with free Kelvin waves uncoupled with convection and quicker/stronger for LN than for EN. They propagate faster and are more intense in the region near SA (a little east of 120°W) during LN, when SSTs are colder, there is no deep convection over the eastern Pacific, and the convection over tropical SA is stronger. The anomalous positive SSTs over central-eastern equatorial Pacific in EN decrease the phase velocity of the MJO (Figs. 11e, 11h, between 180°W-160°W, phases 6-7), slowing its convection across the region (Fig. 8), and causing a delay in the inversion of the intraseasonal dipole over SA until MJO_{EN}phase7.

5.2 Precipitation and its extremes over SA associated with MJO in EN and LN states

In the previous section, the global patterns of MJO convection (OLR anomalies) and circulation were analyzed. In this section a more detailed and reliable picture of the South American anomalies of precipitation and frequency of extreme events, obtained from rain gauge data, is presented. The focus is on the differences between MJO impacts in EN and LN states because the differences between the composite anomalies for NT years and all years have been briefly described in section 4.2, and the main mechanisms behind these anomalies are explained in Grimm (2019).

5.2.1 Precipitation anomalies

As in Grimm (2019), it is convenient to start the analysis from phase 7, when the anomalous precipitation dipole between CESA and SESA starts inverting polarity over SA in NT years, entering the phase with strongest precipitation in CESA (Fig. 6). In EN state, the dipole reversal is delayed compared to LN and NT years, as already seen in the OLR anomaly composites (Figs. 4, 8). While in NT and LN the CESA-SESA dipolar characteristic is lost in phase 7, it is still clear in the EN state, in which the transition takes place in phase 8 (Fig. 12) and the highest difference between the dipole centers happens in phase 1, fading in phase 2. In LN the transition starts in phase 7, the highest difference lasts from phase 8 through phase 1,

and the dipole is still discernible in phase 2. Therefore, the transition from maximum negative anomalies to maximum positive anomalies in CESA happens later and this polarity lasts for a shorter time in EN than in LN, making the precipitation dipole antisymmetric with respect to the time distribution of its phases. While the positive precipitation anomalies during EN are strong only over CESA, during LN they also extend over Central SA and other parts of the Amazon. During LN, they are stronger over northern CESA in phase 8 and enhanced in its southern part in phase 1 (Fig. 12). These differences are consistent with the different EN and LN basic states and circulation anomalies, and with the extratropical teleconnection eastward shift in EN and westward shift in LN, discussed previously.

Hence, the most significant positive precipitation anomalies in CESA happen in MJO_{EN}phase1 and MJO_{LN}phase8. Moreover, the spatial rainfall distribution in CESA is different in this enhanced precipitation period during EN, LN and NT years. In EN (Fig. 12), the positive precipitation anomalies are weak in phase 8, but very prominent in phase 1, extending from the SACZ region, where they are supported by the extratropical teleconnection from the subtropical central-east South Pacific, to NE Brazil, where they are supported by strong westerly wind anomalies at lower levels, associated with Kelvin wave tropical teleconnection (Fig. 7). The contribution of the filtered precipitation anomalies related to the MJO in EN years reaches more than 5 mm/day, which is equivalent to 50% of the daily precipitation climatology in DJF over extensive regions of the SA monsoon core region in central SA (Fig. 2a). In MJO_{LN}phase1, the positive precipitation anomalies are enhanced over central Brazil and in the southern edge of the SACZ, with significant positive precipitation anomalies extending beyond 20°S, reaching the northern part of SESA (Fig. 12).

The most intense positive precipitation anomalies over CESA are observed in MJO_{EN}phase1, from SACZ to northern CESA and Northeast Brazil (Fig. 12). On the other hand, the negative precipitation anomalies in SESA are stronger in MJO_{LN}phases8+1 (Fig. 12) and weaker in MJO_{EN}phases8+1, because of the favorable conditions to subsidence in SESA during LN and enhanced precipitation during EN (Grimm 2003, 2004).

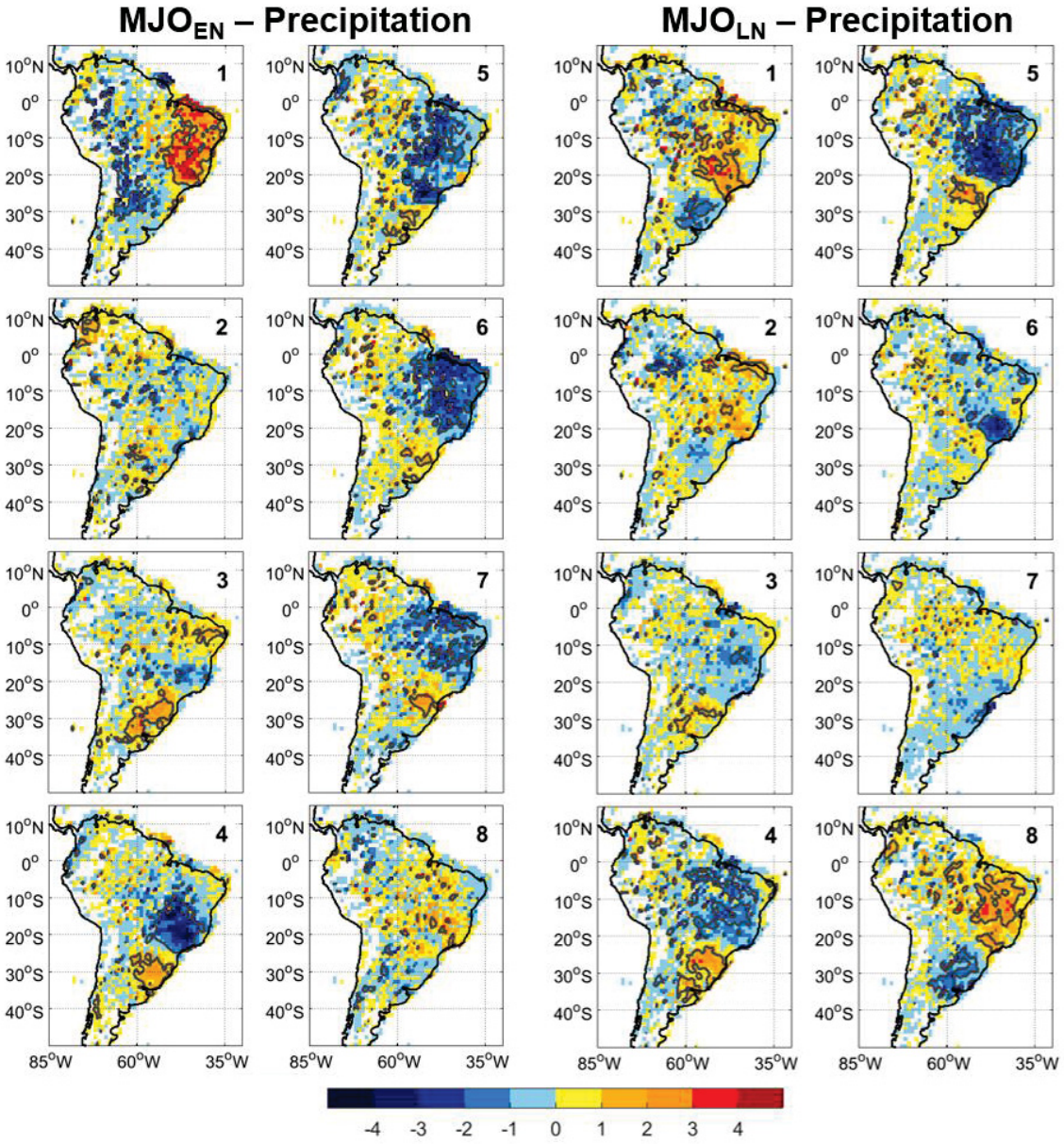

Fig. 12 Composite anomalies of austral summer daily precipitation rate (color bar, mm day^{-1}) filtered in the 20–90 day band, for each MJO phase during the austral summer (DJF) in (left) EN state and (right) LN state. Gray lines delimit anomalies with confidence levels better than 85%

When the positive precipitation anomalies retract towards NE Brazil in phase 2, they remain significant in NT years (Fig. 6) and LN years (Fig. 12), but fade in EN years (Fig. 12), due to the unfavorable EN basic state with subsidence over Northeast Brazil. The OLR anomalies show that when convection is enhanced (weakened) in central equatorial Pacific due to combined effect of EN (LN) and MJO the enhanced convection over the equatorial northeast SA in phases 8, 1 and 2 is stronger in LN than in EN (Fig. 8).

Following the MJO phases 4, 5 and 6, when the precipitation anomalies are reversed over CESA and SESA, in EN the negative precipitation anomalies in CESA are enhanced between phases 4 and 7, while in LN they are most enhanced in phases 4 and 5, especially the latter. ENSO plays a role in enhancing the strongest MJO precipitation anomalies in CESA. At the same time, it influences the precipitation anomalies in SESA, where the positive precipitation anomalies are more frequent in EN than in LN (Fig. 12), which is coherent with the ENSO effect on SESA (Grimm 2003; 2004). In MJO_{EN}phases3-7 only in MJO_{EN}phase5 negative anomalies occupy part of southern Brazil, because the subtropical anticyclonic anomaly in MJO_{EN}phase5 is shifted south, but there are still positive anomalies in the southern part of SESA (Fig. 12) (Figs. 5, 9, 10). Yet only in MJO_{LN}phases3-5 there are significant positive anomalies over SESA, coherent with the LN effect on this region (Fig. 12).

5.2.2 Extreme precipitation frequency

As the ENSO and the MJO are known to increase significantly the frequency of extreme events on SA (Grimm and Tedeschi 2009; Hirata and Grimm 2015; Grimm 2019), it is important to verify how the ENSO states modulate the MJO impacts on extreme events. In the previous section it was shown that ENSO impacts strongly on average daily precipitation anomalies in certain MJO phases. Therefore, it is relevant to check if the ENSO-MJO effect on the frequency of extreme events is consistent with the impact on the daily mean precipitation, since the social impact of changes in extremes is more dramatic than changes in average precipitation. Here this analysis is exhibited in detail using observed rain gauge data, since gridded datasets underestimate extreme precipitation events on SA in areas much affected by the MJO (Hirata and Grimm, 2018), highlighting the importance of this analysis.

Figures 6 and 13 exhibit the ratio between the probability of occurrence of extreme precipitation events for each combination of ENSO state and MJO phase and the mean probability. Although the effect on the frequency of extremes follows approximately the effect on daily precipitation (Figs. 5 and 12), there are instances in which the effect on the extremes is strong, but does not affect the average daily precipitation significantly, and vice-versa.

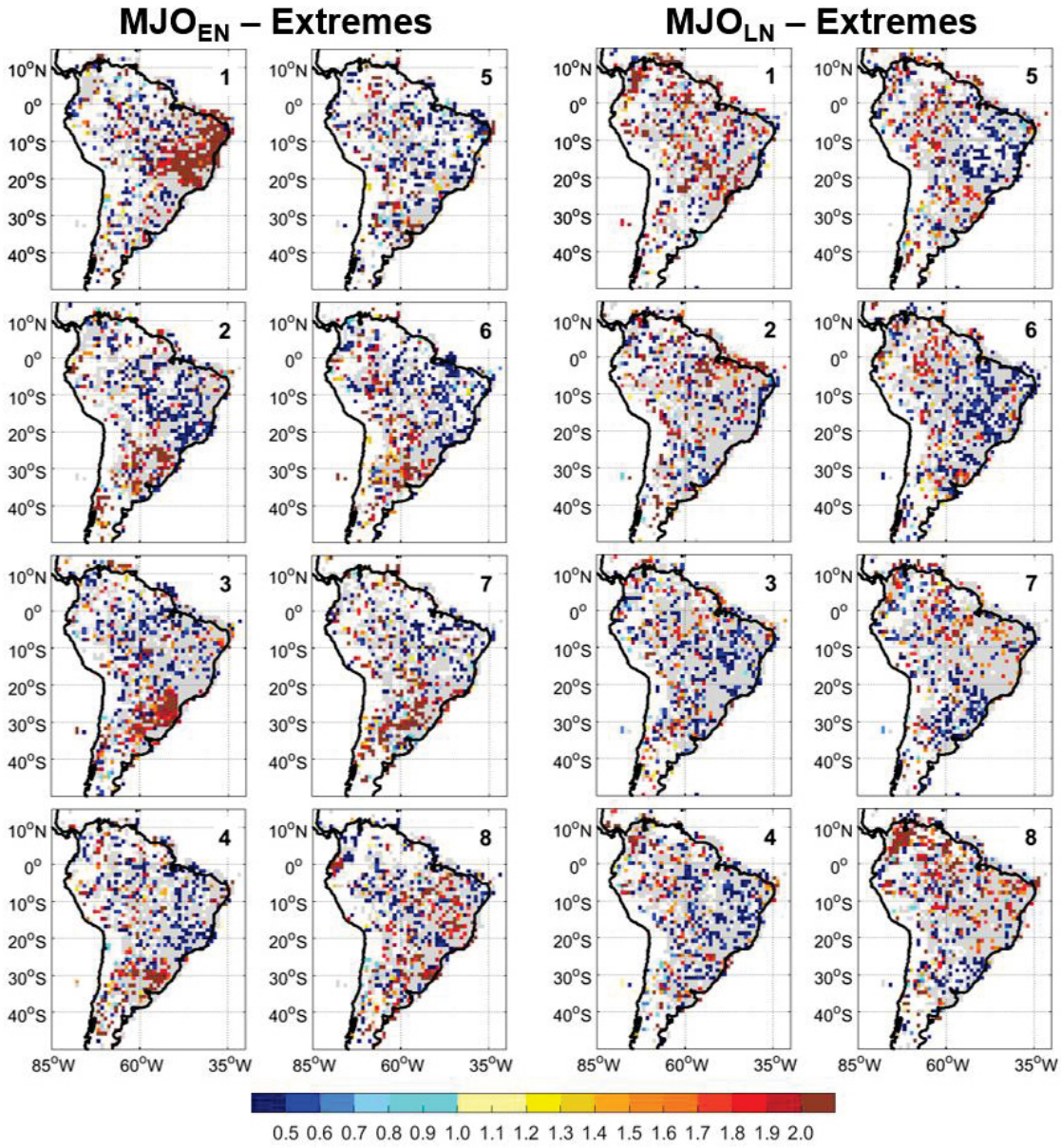

Fig. 13 Ratio between the probability of extreme precipitation events in each of the MJO phases and the mean probability, for each MJO phase during the austral summer (DJF) in (left) EN state and (right) LN state. Only ratios corresponding to statistically significant difference between the probability of occurrence for each MJO phase and the mean probability with confidence levels better than 85% are shown in color. Grey indicates regions with lower confidence levels, and white indicates regions void of observed gauge daily data

During EN, this happens in MJO$_{EN}$phase2, when changes in the average daily precipitation display little significance (Fig. 12) while extremes are impacted significantly over CESA and SESA (Fig. 13). On the other hand, in MJO$_{EN}$phases5+6 the effect on the extremes is weaker than over the average rainfall. In MJO$_{EN}$phase1 and 3 there is consistency between these effects, and the EN influence is responsible for the strongest and most

extensive MJO impacts on CESA (and SACZ) in phase 1 and SESA in phase 3 (Figs. 12, 13), much stronger than in NT (Fig. 6). The streamfunction anomalies for MJO_{EN}phase1 (Fig. 10) show favorable anomalies to enhance the circulation associated with extremes in the SACZ (cf. Fig. 10 with Fig. 13 of Tedeschi, Grimm and Cavalcanti 2015), while phase 3 shows a reversed dipole over SA, which favors higher precipitation in SESA. The frequency of extreme rainfall events in MJO_{EN}phase1 more than doubles over the SACZ, the eastern edge of monsoon core region, and the NE Brazil, very populated regions of Brazil.

During LN, in MJO_{LN}phase6 the effect on the extremes in CESA is stronger than on the average rainfall, except on the southern edge of the SACZ (cf. Figs. 12 and 13). Another example is the extreme northwest of SA in MJO_{LN}phases8+1, since in MJO_{LN}phase8 the average rainfall over CESA increases more significantly and extensively than its extreme events. During MJO_{LN}phase1, as also happens during EN, there is consistent increase in rainfall and its extreme events in the SACZ, especially its southern edge, corroborating Hirata and Grimm (2015), who found an increase in extreme events under the same scenario in the southeast Brazilian coast. Albeit the frequency of extreme events doubles, this region is smaller and to the south of that observed in MJO_{EN}phase1 (Fig. 13).

The EN state contributes significantly to increase the frequency of extreme events in SESA during MJO_{EN}phases2-8 with respect to states LN and NT, with only a weakening in phase 5. In some cases there is increase even in phases when in LN and NT there is decrease of extreme events in SESA, such as phases 7 and 8 (Figs. 13 and 6). The enhancement of the occurrence of extreme events by factors greater than 2.0 during several MJO phases in EN occurs in vast regions of SESA, as Southern Brazil, Paraguay, Uruguay and Argentina, corroborating Hirata and Grimm (2015), who found similar results over the La Plata Basin. Hence, the EN modulates MJO impacts on extreme events in SESA, enhancing and prolonging these impacts, because of the EN enhancement of anomalous Hadley circulation and regional circulation that favor the precipitation in this region (Grimm, Barros and Doyle, 2000; Grimm, 2003).

Regarding the LN state, coherently with the LN teleconnections to SESA, it causes a decrease of the number of extreme events in SESA with respect to NT (cf. Figs. 13 and 6) in MJO_{LN}phases2-8, even when average precipitation is increased, with only a weakening in phase 5, but it is less intense than the increase produced by EN.

The changes in the frequency of extreme events during MJO phases in NT years (Fig. 6) resemble the patterns described by Grimm (2019) (its Fig. 8) using all the years in the same

period, with the greatest difference residing in phases 1 and 5. In NT years (Fig. 6) the dominant changes of the frequency of extreme events in CESA are limited to north of 15°S, with insignificant changes or even isolated opposite changes over the SACZ. Yet when using all years, the dominant changes extend southward, to the SACZ region. This means that both, EN and LN years contribute to change the frequency of extreme events in this region (as was already reported for the average precipitation), which is clearly visible in Fig. 13. This corroborates Hirata and Grimm (2015), who identified a weakening of the extreme events on intraseasonal scales in the SE Brazilian coast during neutral ENSO years.

The highest impact on the frequency of extreme events in SESA in NT years takes place in phase 4, followed by phase 3, consistently with the most intense precipitation anomalies (Fig. 6). In a composite using all years, Grimm (2019) emphasizes the increase in the frequency of extreme events in phase 3 over SESA, which has a more significant contribution from EN (Fig. 13) than NT (Fig. 6). Hence, the highest growth in the frequency of extreme events in SESA happens in MJO_{EN}phase3 (Fig. 13), while in NT it occurs in phase 4 (Fig. 6).

The strongest modulation of MJO impacts on extremes happens during the EN state, probably because the LN state represents an enhancement of climatological conditions over the Pacific.

6 ENSO modulation of the MJO impact on the first intraseasonal precipitation variability mode in SA

There is a dipolar mode of monsoon precipitation intraseasonal variability in SA featuring opposite anomalies between CESA and SESA, which is present in all intraseasonal time scales (Grimm 2019, its Fig. 9, REOF1, partially adapted in Fig. 14, upper left panel, in order to define the areas of the action centers of this dipole). This intraseasonal dipole oscillation over SA has been detected long ago (e. g., Casarin and Kousky 1986; Nogués-Paegle and Mo 1997; Diaz and Aceituno 2003). Recently the potential of its subseasonal prediction was assessed (Grimm, Hakoyama and Scheibe 2021), since the major MJO impacts on SA daily precipitation project strongly on this mode, as shown for MJO_{NT}phase4 in Fig. 14 (upper right panel).

Since both action centers of this dipolar oscillation are in very populated regions, with great agricultural activity and hydroelectric energy generation, it is interesting to analyze how this mode is affected by ENSO modulation of the MJO impacts on SA monsoon precipitation.

Figure 14 (bottom panels) represents the DJF average daily precipitation anomalies stratified by ENSO state and MJO phase over the regions representing the northern and southern centers of this mode, in CESA and SESA, respectively (see also Fig. 2a).

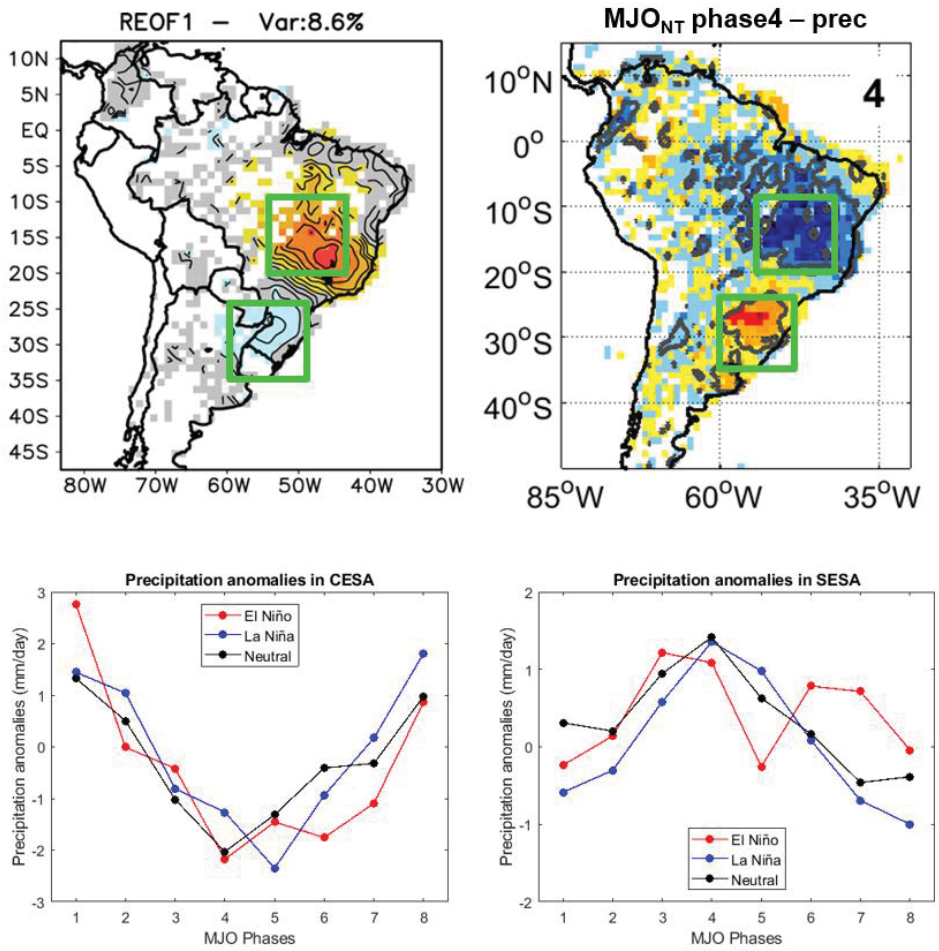

Fig. 14 Upper panels: (Left) Factor loadings of the first intraseasonal variability mode of daily precipitation in the 20-90 day band for South America (from Grimm 2019), and (Right) composite anomalies of daily precipitation rate filtered in the 20–90 day band, for MJO phase 4 during the austral summer (DJF) in NT years, taken from Fig. 6. In both maps are indicated the regions representing the dipole centers of that mode, used for averaging the daily precipitation in each MJO phase and ENSO state shown in the bottom panels. Bottom panels: (Left) average daily precipitation anomalies observed during DJF and stratified by ENSO state and MJO phase over the region representing the northern center of the first variability mode (in CESA), and (Right) over the region representing the southern center of the first variability mode (in SESA)

It is worth emphasizing that the northern center of this dipole (in CESA) displays much stronger intraseasonal variability than the southern one (in SESA). On the other hand, the ENSO impact in summer is stronger over SESA than over CESA (Figs. 2b, 2c), as shown by the interannual precipitation mode associated with ENSO (Grimm and Zilli 2009; Grimm 2011). This is coherent with the fact that the differences between the curves for EN and LN in

Fig. 14 are larger for SESA than for CESA and that for SESA the prevalent differences with respect to NT years are positive for EN years and negative for LN years in Fig. 14, while for CESA there is no obvious preference.

This analysis shows results coherent with the observed changes in precipitation discussed in section 5.2.1. Considering the strongest Walker circulation and convection anomalies over the equatorial eastern Indian Ocean/western Pacific Ocean and the central/eastern Pacific Ocean associated with ENSO and MJO, the MJO phases that most project on the ENSO states in DJF are MJO8+1 (onto EN state) and MJO4+5 (onto LN state) (cf. Figs. 2 and 4). Therefore, we would expect the anomalous convection and circulation in MJO_{EN}phases8+1 and MJO_{LN}phases4+5 to be reinforced in EN and LN, respectively. As there is a lag between forcing and precipitation response, strongest enhancement of the MJO-related anomalies in CESA would be expected in MJO_{EN}phase1 and MJO_{LN}phase5. This is confirmed in Fig. 12 and Fig. 14. On the other hand, anomalies in CESA would be expected to weaken in MJO_{EN}phase5 and MJO_{LN}phase1, with respect to the opposite ENSO state. These reduced anomalies are reflected in Fig. 14 (bottom left panel). Comparison of the anomalies in Fig. 12 with those in Fig. 6 shows that really the CESA anomalies are weakened in MJO_{EN}phase5 and MJO_{LN}phase1 with respect to the corresponding MJO phases in the opposite ENSO state, with the exception of the anomalies in the southern edge of the SACZ, which are enhanced in both EN and LN states, due to extratropical teleconnections triggered by subtropical convective anomalies in central-east South Pacific, as mentioned in section 5.1.3. This enhancement of SACZ in MJO phase 1 during both EN and LN probably represents a nonlinear ENSO effect on MJO anomalies over SA.

Although the evolution through the MJO phases of the average daily precipitation anomalies over SESA (Fig. 14 bottom right panel) is approximately opposite to that over CESA (Fig. 14 bottom left panel), there is a larger influence of EN in increasing precipitation with respect to NT years in this region and of LN in decreasing it. The greatest deviation from this behavior occurs in phase 5, when the anomalies in SESA during EN are greatly reduced in relation to those obtained in LN (and even NT), which is consistent with the fact that the phase 5 pattern of MJO is weakened in EN and strengthened in LN. This is also consistent with the fact that also in CESA the anomalies in MJO_{EN}phase5 the anomalies are weaker than in MJO_{LN}phase5. Since the SESA center of the dipole is a subtropical/extratropical region, the influence of MJO is not so direct as in CESA, and there are different sources of variability, sometimes with contrasting effects: extratropical teleconnections produced by Rossby waves,

anomalous Hadley circulation, the subsidence associated with the enhanced convection in the CESA center of the dipole, which happens to southwest of the enhanced convection (Gandu and Silva Dias 1998).

The MJO drives more precipitation variability in ENSO than in NT years, and stronger in EN than in LN. The amplitude of variation in EN is around 5.0 mm/day in the CESA center and 1.5 mm/day in the SESA center, while during LN the amplitudes are, respectively, 4.0 mm/day and 2.3 mm/day (Fig. 14). In CESA, the EN state is able to more strongly modulate MJO-related rainfall anomalies by increasing the maximum (phase 1) during the wet period rather than by reducing the minimum (phase 4) during the dry period, although this dry period in EN state is more persistent than in NT state. On the other hand, the opposite occurs during LN state, with strongest reduction of the minimum in the dry period (phase 5) and weaker increase in the wet period (phase 8) (Fig. 14).

7 Conclusions

This investigation has addressed the modulation of the MJO and its main impacts on SA precipitation by the ENSO states (EN, LN, NT) in observational datasets. Although the MJO activity, expressed by the intraseasonal variance of some fields, does not show great connection with ENSO (e.g., Hendon, Zhang and Glick 1999), the ENSO modulation of the MJO-related anomalies can produce significant changes in their impacts over SA. The equatorial eastward propagating MJO convective anomalies, coupled with a pair of large-scale anomalous Walker cells, are affected by the significant changes in the basic Walker circulation produced by the EN and LN states. Furthermore, the background ENSO-related SST, convection and circulation anomalies (Fig. 2) influence the relative occurrence of MJO phases (Fig. 3), the eastward MJO propagation (Figs. 4, 7, 11), the position and intensity of the MJO-related convection (Figs. 4, 8), the MJO-related teleconnections (Figs. 5, 9, 10), and the impacts on precipitation and extremes over SA (Figs. 6, 12, 13, 14).

It is worth reminding that the results do not simply show the added anomalies produced by ENSO and MJO. The anomalies displayed are filtered in the 20-90 day band. Therefore, they show the effect of the ENSO states on the MJO itself and its impacts, since the basic state in which the MJO develops is altered by these states (background SST warm pool, circulation, most intense tropical convection (Fig. 2)). Changes in these impacts in opposite ENSO states with respect to the NT state are not always opposite, indicating the existence of both linear and nonlinear effects.

The different propagation speeds over the Indian Ocean and the Pacific Ocean observed in Figs. 4, 7 and 11 have been explained in previous studies as a change in the phase speed of the equatorial Kelvin wave component of the MJO in a moist convective regime as in the Indian Ocean or in a dry regime (as over the central-east Pacific) (e.g., Zhang 2005; Pohl and Matthews 2007; Wei and Ren 2019). The changes in the MJO propagation speed over the Maritime Continent-western Pacific sector between EN and LN states may be due to the fact that during EN (LN), conditions over this area are drier (wetter) than normal, related to the suppression (enhancement) of mean convection there. Hence, there will be a weak "dry" regime (enhanced moist convective regime) over the sector, and the MJO would be expected to speed up (slow down) there in EN (LN), as observed. On the other hand, over the central-eastern Pacific, the MJO propagation speed decreases (increases) in EN (LN) due to warmer (colder) SSTs (Zhang 2005). The wind perturbation propagates faster eastward and the low-level convergence and westerly winds are already strong over the eastern Pacific and SA in MJO phase 8 during LN, while during EN they reach the maximum in phase 1 (Figs. 7, 9, 11). The same is true for the upper-level easterlies, which are stronger and propagate eastward faster over the central-east Pacific during LN than during EN (Figs. 10, 11). This effect may be responsible for the earlier appearance of anomalous convection over SA in LN (phase 8) than in EN (phase 1) (Figs. 8, 11).

Concerning MJO-related convection, the main features of MJO phases that are similar to characteristics of the EN and LN states are enhanced during these states, as shown by the peaks of enhanced convection over the Maritime Continent in phase 5 during LN and enhanced convection in central equatorial Pacific in phase 1 during EN. Besides, the influence of ENSO opposite background states can also shift, extend, reduce, enhance or weaken MJO-related anomalous patterns. For instance, over northeast SA, the MJO-related anomalous subsidence and dryness that occurs mainly in phases 5 and 6 are enhanced during EN and extended to phase 7, while anomalous wetness in phases 1 and 2 is reduced, thanks to the EN background anomalies of Walker circulation subsidence over that region. During the LN state, the opposite occurs (cf. Figs. 4 and 8).

ENSO can modify the MJO-rainfall relationship in SA not only because it modifies the MJO characteristics regarding convective anomalies and their propagation, but also because it creates different basic states through which the perturbations propagate toward SA, affecting the physical mechanisms by which the MJO influences rainfall variability in SA.

The anomalous precipitation composites for MJO phases in NT ENSO conditions (Fig. 6) show some differences with respect to the composites for all years in Grimm (2019) (its Fig. 7). This indicates that ENSO enhances some aspects, with EN and LN favoring anomalies with same sign in important regions and MJO phases. The most prominent example refers to the anomalies in southern CESA, over the SACZ. CESA displays the most intense and extensive anomalies, positive in phases 8+1 and negative in phases 4+5 (Fig. 12). It is noticeable that the NT precipitation anomalies are weaker over its southern part, over the SACZ and its southern edge (Fig. 6). Figure 12 shows that in both EN and LN states there is enhanced precipitation in this region in phases 8+1 and reduced precipitation in phases 4+5 with respect to NT state. Since Grimm (2019) showed that an important part of these anomalies in southern CESA is due to tropics-extratropics teleconnections with the subtropical central-east South Pacific, and both ENSO states provide forcing in this region efficient in producing this teleconnection, it seems that nonlinear effects are acting and ENSO has an important role in this regard.

The slower (faster) eastward propagation of the MJO signal over the equatorial central-eastern Pacific, probably due to warmer (colder) SSTs and enhancement (suppression) of convection in this region during EN (LN) (Figs. 2, 7 and 11), delays (anticipates) the MJO phase in which there is inversion of the intraseasonal precipitation dipole over CESA in EN (LN) (Fig. 14), making the distribution of positive and negative precipitation anomalies in CESA less (more) symmetric in EN (LN) than in NT. This effect is more noticeable in the second half of the MJO cycle (phases 6, 7, 8), since in this period there is the strongest difference between EN and LN equatorial anomalous convection in central-east Pacific, between 180°-120°W (Fig. 8). The decreased (increased) MJO phase velocity leads to the peak of the tropics-tropics teleconnections between the central-eastern equatorial Pacific and SA in MJO_{LN}phase8, while it happens later in MJO_{EN}phase1 (Figs. 9, 10). Besides, since the different EN/LN OLR background states affect the enhanced MJO convection over the subtropical central-eastern South Pacific, favoring it in MJO_{LN}phases7+8 and, a little further east, in MJO_{EN}phases8+1 (Fig. 8), these differences affect the evolution, strength, and propagation of the tropics-extratropics teleconnections to SA in ENSO years (Fig. 10). They are stronger one phase later and are shifted east in MJO_{EN}phases8+1 with respect to MJO_{LN}phases8+1.

Therefore, the strongest impact over CESA in SA is advanced by one phase in LN with respect to EN, since both, the tropics-tropics and the tropics-extratropics teleconnections

that connect the MJO to SA are established one phase before in LN (Figs. 9 and 10). Notwithstanding, the impact on subtropical CESA (and in the SACZ) rainfall and its extremes is still strong in MJO_{LN}phase1, being a little displaced westward in MJO_{LN}phases8+1 with respect to MJO_{EN}phases8+1 (Figs. 8, 9, 10, 12).

Observations also show that MJO_{EN}phase4 and MJO_{LN}phase4 favor suppressed MJO convection in the central-eastern subtropical South Pacific (Fig. 8), stronger and a little further east in MJO_{LN}phase4 than MJO_{EN}phase4. It shifts the tropics-extratropics teleconnections to SA eastward in MJO_{LN}phase4 with respect to MJO_{EN}phase4 (Fig. 10). This behavior is analogous to the teleconnection wave train displaced eastwards in MJO_{EN}phases8+1 with respect to MJO_{LN}phases8+1 due to enhanced convection over the central-eastern subtropical South Pacific stronger and more to the east in MJO_{EN}phases8+1 than MJO_{LN}phases7+8. Therefore, the ENSO seems to modulate the MJO teleconnections to SA in complex ways due to its widespread influence on both the basic state and the MJO convective anomalies.

The ENSO-driven changes in the MJO impacts on SA are more significant and extensive in the frequency of extreme events than in the precipitation anomalies. It could be argued that the frequency of extreme events (Fig. 13) is extensively and significantly much enhanced (or reduced) with respect to NT (Fig. 6) in regions where the effects of both ENSO and MJO contribute to enhance (or reduce) them. The strongest modulation of MJO impacts on extremes happens during the EN state, probably because it represents a stronger deviation from the climatology, since the LN state represents an enhancement of climatological conditions over the Pacific. The most striking impacts increase more than twice the frequency of extreme events in CESA during MJO_{EN}phase1 and in SESA during MJO_{EN}phase3. Since these are highly populated regions in SA, and summer is the rainy season in CESA and part of SESA, it is relevant to know these effects.

Additional ongoing research is focused on linear and nonlinear ENSO effects on MJO and analysis of models' skill in simulating the observed results, since they are important for subseasonal prediction during the summer monsoon (Grimm, Hakoyama and Scheibe 2021).

Acknowledgements A. M. G. received financial support from the National Council for Scientific and Technological Development (CNPq-Brazil) and L. G. F. was partially supported by Coordination for the Improvement of Higher Education Personnel (CAPES-Brazil).

References

Aceituno P (1988) On the Functioning of the Southern Oscillation in the South American Sector. Part I: Surface Climate. Mon Weather Rev 116:505–524. https://doi.org/10.1175/1520-0493(1988)116<0505:OTFOTS>2.0.CO;2

Alvarez MS, Vera CS, Kiladis GN, Liebmann B (2015) Influence of the Madden Julian Oscillation on precipitation and surface air temperature in South America. Clim Dyn 46:245–262. https://doi.org/10.1007/s00382-015-2581-6

Arcodia MC, Kirtman BP, Siqueira LSP (2020) How MJO teleconnections and ENSO interference impacts U.S. precipitation. J Clim 33:4621–4640. https://doi.org/10.1175/JCLI-D-19-0448.1

Cai W, McPhaden MJ, Grimm AM et al (2020) Climate impacts of the El Niño–Southern Oscillation on South America. Nature Reviews Earth & Environment 1:215–231. https://doi.org/10.1038/s43017-020-0040-3

Carvalho LMV, Jones C, Liebmann B (2004) The South Atlantic Convergence Zone: Intensity, Form, Persistence, and Relationships with Intraseasonal to Interannual Activity and Extreme Rainfall. J Clim 17:88–108. https://doi.org/10.1175/1520-0442(2004)017<0088:TSACZI>2.0.CO;2

Casarin DP, Kousky VE (1986) Precipitation anomalies in Southern Brazil and variations of the atmospheric circulation. Rev Bras Meteor 1:83–90

Dawson A (2016) Windspharm: A High-Level Library for Global Wind Field Computations Using Spherical Harmonics. Journal of Open Research Software 4. https://doi.org/10.5334/jors.129

Dee DP et al (2011) The ERA-Interim reanalysis: configuration and performance of the data assimilation system. Q J Roy Meteor Soc 137:553–597. https://doi.org/10.1002/qj.828

Díaz A, Aceituno P (2003) Atmospheric Circulation Anomalies during Episodes of Enhanced and Reduced Convective Cloudiness over Uruguay. J Clim 16:3171–3185. https://doi.org/10.1175/1520-0442(2003)016<3171:ACADEO>2.0.CO;2

Duchon CE (1979) Lanczos Filtering in One and Two Dimensions. J Appl Meteor 18:1016–1022. https://doi.org/10.1175/1520-0450(1979)018<1016:LFIOAT>2.0.CO;2

Fink A, Speth P (1997) Some potential forcing mechanisms of the year-to-year variability of the tropical convection and its intraseasonal (25-70-day) variability. Int J Climatol 17:1513–1534. https://doi.org/10.1002/(SICI)1097-0088(19971130)17:14<1513::AID-JOC210>3.0.CO;2-U

Gandu AW, Silva Dias PL (2018) Impact of tropical heat sources on the South American tropospheric upper circulation and subsidence. J Geophys Res 103:6001–6015. https://doi.org/10.1029/97JD03114

Ghelani RPS et al (2017) Joint Modulation of Intraseasonal Rainfall in Tropical Australia by the Madden-Julian Oscillation and El Niño-Southern Oscillation. Geophys Res Lett 44:10754–10761. https://doi.org/10.1002/2017GL075452

Grimm AM (2003) The El Niño Impact on the Summer Monsoon in Brazil: Regional Processes versus Remote Influences. J Clim 16:263–280. https://doi.org/10.1175/1520-0442(2003)016<0263:TENIOT>2.0.CO;2

Grimm AM (2004) How do La Niña events disturb the summer monsoon system in Brazil? Clim Dyn 22:123–138. https://doi.org/10.1007/s00382-003-0368-7

Grimm AM (2011) Interannual climate variability in South America: impacts on seasonal precipitation, extreme events, and possible effects of climate change. Stoch Environ Res Risk Assess, 25:537–554. https://doi.org/10.1007/s00477-010-0420-1

Grimm AM (2018) South American Monsoon and its Extremes. In: Vuruputur VJ, Sukhatme R, Murtugudde R, Roca (eds) Tropical Extremes: Natural Variability and Trends, Elsevier, Amsterdam, pp 51–93. https://doi.org/10.1016/B978-0-12-809248-4.00003-0

Grimm AM (2019) Madden–Julian Oscillation impacts on South American summer monsoon season: precipitation anomalies, extreme events, teleconnections, and role in the MJO cycle. Clim Dyn 53:907–932. https://doi.org/10.1007/s00382-019-04622-6

Grimm AM, Ambrizzi T (2009) Teleconnections into South America from the Tropics and Extratropics on Interannual and Intraseasonal timescales. In: Vimeux F, Sylvestre F, Khodri (eds) M. Past climate variability in South America and Surrounding Regions: from the last glacial maximum to the Holocene, 14ª ed. Springer, USA, pp 159–191

Grimm AM, Barros VR, Doyle ME (2000) Climate Variability in Southern South America associated with El Nino and La Nina events. J Clim 13:35–58. https://doi.org/10.1175/1520-0442(2000)013<0035:CVISSA>2.0.CO;2

Grimm AM, Ferraz SET, and Gomes J (1998) Precipitation Anomalies in Southern Brazil Associated with El Nino and La Nina Events. J Clim 11:2863–2880. https://doi.org/10.1175/1520-0442(1998)011<2863:PAISBA>2.0.CO;2

Grimm AM, Hakoyama LR, Scheibe LA (2021) Active and break phases of the South American summer monsoon: MJO influence and subseasonal prediction. Clim Dyn 56:3603–3624. https://doi.org/10.1007/s00382-021-05658-3

Grimm AM, Pal JS, Giorgi F (2007) Connection between Spring Conditions and Peak Summer Monsoon Rainfall in South America: Role of Soil Moisture, Surface Temperature,

and Topography in Eastern Brazil. J Clim 20:5929–5945. https://doi.org/10.1175/2007JCLI1684.1

Grimm AM, Saboia JPJ (2015) Interdecadal Variability of the South American Precipitation in the Monsoon Season. J Clim 28:755–775. https://doi.org/10.1175/JCLI-D-14-00046.1

Grimm AM, Silva Dias PL (1995) Analysis of tropical-extratropical interactions with influence functions of a barotropic model. J Atmos Sci 52:3538–3555. https://doi.org/10.1175/1520-0469(1995)052<3538:AOTIWI>2.0.CO;2

Grimm AM, Tedeschi RG (2009) ENSO and Extreme Rainfall Events in South America. J Clim 22:1589–1609. https://doi.org/10.1175/2008JCLI2429.1

Grimm AM, Zilli MT (2009) Interannual Variability and Seasonal Evolution of Summer Monsoon Rainfall in South America. J Clim 22:2257–2275. https://doi.org/10.1175/2008JCLI2345.1

Gutzler DS (1991) Interannual Fluctuations of Intraseasonal Variance of Near- Equatorial Zonal Winds. J Geophys Res 96:3173–3185. https://doi.org/10.1029/90jd01831

Hendon HH, Wheeler MC, Zhang C (2007) Seasonal Dependence of the MJO-ENSO Relationship. J Clim 20:531–543. https://doi.org/10.1175/JCLI4003.1

Hendon HH, Zhang C, Glick JD (1999) Interannual Variation of the Madden-Julian Oscillation during Austral Summer. J Clim 12:2538–2550. https://doi.org/10.1175/1520-0442(1999)012<2538:ivotmj>2.0.co;2

Hirata FE, Grimm AM (2015) The role of synoptic and intraseasonal anomalies in the life cycle of summer rainfall extremes over South America. Clim Dyn 46:3041–3055. https://doi.org/10.1007/s00382-015-2751-6

Hirata FE, Grimm AM (2018) Extended-range prediction of South Atlantic convergence zone rainfall with calibrated CFSv2 reforecast. Clim Dyn 50:3699–3710. https://doi.org/10.1007/s00382-017-3836-1

Kalnay E et al (1996) The NCEP/NCAR 40-year reanalysis project. Bull Am Meteor Soc 77: 437–471. https://doi.org/10.1175/1520-0477(1996)077<0437:TNYRP>2.0.CO;2

Kessler WS (2001) EOF Representations of the Madden-Julian Oscillation and Its Connection with ENSO. J Clim 14:3055–3061. https://doi.org/10.1175/1520-0442(2001)014<3055:EROTMJ>2.0.CO;2

Lee RW et al (2019) ENSO Modulation of MJO Teleconnections to the North Atlantic and Europe. Geophys Res Lett 46:13535–13545. https://doi.org/10.1029/2019GL084683

Liebmann B, Allured D (2005) Daily Precipitation Grids for South America. Bull Am Meteor Soc 86:1567–1570. https://doi.org/10.1175/BAMS-86-11-1567

Liebmann B, Smith CA (1996) Description of a Complete (Interpolated) Outgoing Longwave Radiation Dataset, Bull Am Meteor Soc 77:1275-1277. https://www.jstor.org/stable/26233278

Lorrey A et al (2012) Reconstructing the South Pacific Convergence Zone Position during the Presatellite Era: A La Niña Case Study. Mon Weather Rev 140:3653–3668. https://doi.org/10.1175/MWR-D-11-00228.1

Matsuno T (1966) Quasi-Geostrophic Motions in the Equatorial Area. J Meteorol Soc Jpn 44:25–43. https://doi.org/10.2151/jmsj1965.44.1_25

Moon JY, Wang B, Ha K (2011) ENSO regulation of MJO teleconnection. Clim Dyn 37:1133–1149. https://doi.org/10.1007/s00382-010-0902-3

Nogués-Paegle J, Mo KC (1997) Alternating Wet and Dry Conditions over South America during Summer. Mon Weather Rev 125:279–291. https://doi.org/10.1175/1520-0493(1997)125<0279:AWADCO>2.0.CO;2

Paegle JN, Byerle LA, Mo KC (2000) Intraseasonal Modulation of South American Summer Precipitation. Mon Weather Rev 128:837–850. https://doi.org/10.1175/1520-0493(2000)128<0837:IMOSAS>2.0.CO;2

Pohl B, Matthews AJ (2007) Observed Changes in the Lifetime and Amplitude of the Madden-Julian Oscillation Associated with Interannual ENSO Sea Surface Temperature Anomalies. J Clim 20:2659–2674. https://doi.org/10.1175/JCLI4230.1

Rao VB, Hada K (1990) Characteristics of Rainfall over Brazil: Annual Variations and Connections with the Southern Oscillation. Theor Appl Clim 42:81–91. https://doi.org/10.1007/BF00868215

Rayner NA et al (2003) Global analyses of sea surface temperature, sea ice, and night marine air temperature since the late nineteenth century. J Geophys Res D: Atmos 108. https://doi.org/10.1029/2002jd002670

Richman MB (1986) Rotation of Principal Components. J Climatol 6:293–335

Ropelewski CF, Halpert MS (1987) Global and Regional Scale Precipitation Patterns Associated with the El Niño/Southern Oscillation. Mon Weather Rev 115:1606–1626. https://doi.org/10.1175/1520-0493(1987)115<1606:garspp>2.0.co;2

Roundy PE et al (2010) Modulation of the Global Atmospheric Circulation by Combined Activity in the Madden-Julian Oscillation and the El Niño-Southern Oscillation during Boreal Winter. J Clim 23:4045–4059. https://doi.org/10.1175/2010JCLI3446.1

Slingo JM et al (1999) On the predictability of the interannual behaviour of the Madden-Julian Oscillation and its relationship with El Nino. Q J R Meteorol Soc 125:583–609

Souza EB, Ambrizzi T (2006) Modulation of the intraseasonal rainfall over tropical Brazil by the Madden-Julian oscillation. Int J Climatol 26:1759–1776

Tam CY, Lau NC (2005) Modulation of the Madden-Julian Oscillation by ENSO: Inferences from Observations and GCM Simulations. J Meteorol Soc Jpn 83:727–743. https://doi.org/10.2151/jmsj.83.727

Tedeschi RG, Grimm AM, Cavalcanti IFA (2015) Influence of Central and East ENSO on extreme events of precipitation in South America during austral spring and summer. Int J Climatol 35:2045–2064. https://doi.org/10.1002/joc.4106

Tedeschi RG, Grimm AM, Cavalcanti IFA (2016) Influence of Central and East ENSO on precipitation and its extreme events in South America during austral autumn and winter. Int J Climatol 36:4797–4814. https://doi.org/10.1002/joc.4670

Tseng KC, Maloney E, Barnes EA (2020) The Consistency of MJO Teleconnection Patterns on Interannual Time Scales. J Clim 33:3471–3486. https://doi.org/10.1175/JCLI-D-19-0510.1

Vincent EM et al (2009) Interannual variability of the South Pacific Convergence Zone and implications for tropical cyclone genesis. Clim Dyn 36:1881–1896. https://doi.org/10.1007/s00382-009-0716-3

Wei Y, Ren H-L (2019) Modulation of ENSO on Fast and Slow MJO Modes during Boreal Winter. J Clim 32:7483-7506. https://doi.org/10.1175/JCLI-D-19-0013.1

Wheeler MC, Hendon HH (2004) An All-Season Real-Time Multivariate MJO Index: Development of an Index for Monitoring and Prediction. Mon Weather Rev 132:1917–1932. https://doi.org/10.1175/1520-0493(2004)132<1917:AARMMI>2.0.CO;2

Wilks DS (2006) Statistical methods in the atmospheric sciences. Academic Press, London

Zhang C (2005) The Madden-Julian Oscillation. Rev Geophys 43:RG2003

Zhang C, Gottschalck J (2002) SST anomalies of ENSO and the Madden-Julian Oscillation in the Equatorial Pacific. J Clim 15:2429–2445. https://doi.org/10.1175/1520-0442(2002)015<2429:SAOEAT>2.0.CO;2

Zhang C, Ling J (2017) Barrier Effect of the Indo-Pacific Maritime Continent on the MJO: Perspectives from Tracking MJO Precipitation. J Clim 30:3439–3459. https://doi.org/10.1175/JCLI-D-16-0614.1

Declarations

Funding:
A. M. G. received financial support from the National Council for Scientific and Technological Development (CNPq-Brazil) and L. G. F. was partially supported by Coordination for the Improvement of Higher Education Personnel (CAPES-Brazil).

Conflicts of interest/Competing interests:
There are no conflicts of interest.

Availability of data and material:
The data used in this research are available at the websites of the institutions cited in the text.

Code availability:
Not applicable.

Authors' contributions:
Both authors contributed equally to the study.

5. Manuscript 2

MJO impacts on South America and their modulation by ENSO in MetUM-GOML3 model

Laís G. Fernandes, Alice M. Grimm and Nicholas P. Klingaman

The impacts of the Madden-Julian Oscillation (MJO) on the South American monsoon season (December, January, and February – DJF) and possible changes during positive (El Niño – EN) and negative (La Niña – LN) phases of the El Niño-Southern Oscillation (ENSO) are analyzed in the UK Met Office Unified Model Global Ocean Mixed Layer configuration (MetUM-GOML3). Experiments with and without ENSO cycle, considering lower (200 km) and higher (90 km) spatial resolution, are performed to assess if the ENSO influences MJO characteristics such as the phase distribution, propagation, convection, and teleconnections to South America (SA). Simulations without ENSO show (1) an established MJO extratropical teleconnection triggered by enhanced convection in the central-east subtropical South Pacific (SP) (source region), and its strongest impact on precipitation over SA in phase 8, earlier than in observations (phase 1); (2) an extratropical teleconnection, triggered by suppressed convection over the same region, with strongest impact on precipitation over SA in phase 4, with opposite sign; (3) increased horizontal resolution enhances the MJO convection and the circulation-precipitation dipole over SA, mainly over subtropical SA. However, the extratropical teleconnections at upper levels are slightly shifted east at higher resolution due to an enhanced SA westerly jet with respect to the lower resolution. In simulations with ENSO cycles, the EN (LN) basic state improves (worsens) MJO eastward propagation and its convection, including enhanced/suppressed convection over the source region. Hence, the extratropical teleconnections (phases 8+1, 3+4) are stronger under EN, with respect to those in simulations without ENSO. Remarkably, the enhanced convection over the source region strengthens under LN (phases 7+8) at higher resolution, favoring improved extratropical teleconnections (phases 8+1). Both ENSO states in the model generate forcing in the central-east subtropical SP that more efficiently triggers stronger teleconnections than simulations without ENSO, indicating nonlinear ENSO effects on MJO anomalies over SA.

Keywords: Coupled global models; ENSO-MJO Interaction; South American monsoon; Teleconnections.

1. Introduction

The Madden-Julian Oscillation (MJO), the leading global intraseasonal climate variability mode (Zhang 2005), has a substantial role in austral summer (December-January-February, DJF) rainfall variability in South America (SA) (Alvarez et al. 2015; Grimm 2019). The MJO influences SA rainfall through tropical (Kelvin and Rossby equatorial waves) and extratropical (extratropical Rossby waves) teleconnections (Grimm 2019). The former affects anomalous precipitation in equatorial SA and tropical central-east SA (CESA); the latter affects the rainfall anomalies over subtropical CESA where the South Atlantic Convergence Zone (SACZ) develops, the eastern edge of the monsoon core region. Also, the extratropical teleconnection strengthens tropical SA precipitation anomalies, which are first established by the tropical teleconnection (Grimm 2019).

Although the El Niño-Southern Oscillation (ENSO) does not affect overall MJO activity (Hendon et al. 1999; Slingo et al. 1999), El Niño events expand the MJO domain eastward in the central Pacific (Hendon et al. 1999; Kessler 2001; Tam and Lau 2005; Wei and Ren 2019). This is a critical region for SA, since here the MJO eastward propagation weakens and the MJO convection shifts south, entering the central-east subtropical South Pacific (SP) (hereafter "the source region") to trigger the extratropical teleconnection to SA (Grimm and Silva Dias 1995; Grimm 2019).

Fernandes and Grimm (2021) described the ENSO-driven modulation of the MJO impacts on SA. They noted that El Niño and La Niña effects on MJO impacts, with respect to neutral ENSO, are not always opposite, indicating nonlinear effects of ENSO on MJO anomalies over SA. Extratropical teleconnections show a similar response, which causes the most prominent precipitation anomalies and extreme events over the SACZ (phases 8-1). El Niño and La Niña favor anomalous MJO convection over the source region, a little further east and later in El Niño (phases 8-1) than La Niña (phases 7-8). Therefore, both ENSO states provide forcing to produce the teleconnection, whereas neutral ENSO years do not. Furthermore, there is a delay in the peak of the teleconnection forcing between central-eastern Pacific and SA precipitation anomalies, from La Niña (phase 8) to El Niño (phase 1). The ENSO-driven modulation of regional MJO teleconnections have been the focus of many recent investigations (Roundy et al. 2010; Moon et al. 2011; Ghelani et al. 2017; Henderson and Maloney 2018; Lee et al. 2019; Arcodia et al. 2020; Tseng et al. 2020).

Subseasonal to seasonal (S2S) predictions of the MJO and its teleconnections have improved recently (Vitart et al. 2017), but the simulation of the MJO-related teleconnections to SA remain challenging (Grimm et al., 2021). It would be valuable to validate the ability of a model to simulate the MJO, its impacts on SA, and the modulation of those impacts by the ENSO, since the roles of ENSO and MJO on S2S predictability for SA rainfall remain unclear (Klingaman et al. 2020). The ENSO-driven modulation of the MJO teleconnections to SA is critical to S2S predictions because both phenomena are considered "windows of opportunity" for extended S2S predictability (Vitart et al. 2015). However, Klingaman et al. (2020) found no improvement in S2S predictions of SA precipitation during active ENSO and MJO periods, potentially because of short-range errors in MJO and ENSO teleconnections to SA (Grimm et al., 2021).

The main MJO characteristics (e.g., convection, eastward propagation) typically improve in ocean-atmosphere Coupled Global Climate Models (CGCMs) with respect to their counterpart atmospheric Global Climate Models (AGCMs), although the mechanisms behind the differences remain unclear (DeMott et al. 2015). MJO characteristics have improved in recent generations of CGCMs (CMIP6; Ahn et al., 2020) compared to previous generations (CMIP5; Ahn et al. 2017), but substantial deficiencies remain in amplitude and propagation. Missing or incorrect convective physics and errors in the climatological state are the primary sources for these errors. The former affects the interaction between convection and circulation and the spatial structure of MJO diabatic heating (Jiang et al. 2015; Klingaman et al. 2015); the latter affects the tropical horizontal moisture distribution (Klingaman and Woolnough 2014a; Kim et al. 2017) and also the mean circulation and atmospheric structure that change the spatial structure of convection.

Besides predicting MJO events, the ability to predict the MJO impact on the global circulation is crucial to S2S predictions (Vitart et al. 2017). The MJO extratropical teleconnections, seen as sources of the S2S predictability, improve in GCMs that better depict the mean background flow and the MJO structure (Henderson et al. 2017). However, model physics changes that improve the MJO generally worsen the basic state (Kim et al. 2011; Klingaman and Woolnough 2014a; Bush et al. 2015).

Wang et al. (2020a) developed MJO teleconnection diagnostics to evaluate GCM biases in the Pacific North American (PNA) teleconnection, while Wang et al. (2020b) described how those biases relate to the model basic state and MJO characteristics. MJO

extratropical teleconnections in the Southern Hemisphere and their behavior in GCMs have been less explored. For instance, the main MJO effect on Australian rainfall does not occur through extratropical teleconnections but through tropical teleconnections (Wheeler et al. 2009). Over SA, S2S predictions of monsoon active and break phases are hampered by incorrect reproduction of the important extratropical teleconnection from central-east subtropical South Pacific to SA (Grimm et al. 2021).

This study evaluates whether the latest atmosphere-mixed-layer-ocean coupled configuration of the Met Office Unified Model (MetUM) (Walters et al. 2019), the Met Office Global Ocean Mixed Layer (MetUM-GOML3; Hirons et al. 2015; Peatman and Klingaman 2018; Giddings et al. 2020), reproduces the main MJO aspects, such as its activity in the Real-time Multivariate MJO (RMM) phase space, eastward propagation, convection, and teleconnections to SA rainfall. Also, we verify how the ENSO affects simulated MJO characteristics and modulates the MJO impacts over SA. Given the limited sample of observed ENSO events, it is crucial to use an extended sample of simulated ENSO events to verify recent observation-based results that show how ENSO-driven changes in the background state influence the MJO teleconnections to SA (Fernandes and Grimm 2021).

Furthermore, we identify which aspects of the MJO and its impacts are sensitive to atmospheric horizontal resolution. Increasing horizontal resolution in previous MetUM coupled configurations improved SA precipitation and circulation patterns, especially in the SACZ (de Souza Custodio et al. 2012; de Souza Custodio et al. 2017), a region strongly affected by the MJO and ENSO (Carvalho et al. 2004; Cunningham and Cavalcanti 2006; Hirata and Grimm 2015; Grimm 2019). The MJO impact on tropical SA precipitation did not improve in the higher resolution of the latest atmospheric MetUM version (Monerie et al. 2020). Also, Solman and Blázquez (2019) concluded that increased horizontal resolution does not improve SA intraseasonal precipitation variability in many GCMs. However, these studies assessed precipitation anomalies in more than one season, smoothing the leading MJO impact on austral summer (DJF). The MJO impacts vary significantly in spring, summer, and autumn (Alvarez et al. 2015).

Section 2 describes the model, the simulations, the datasets, and the methods used. Section 3 presents, for each MJO phase in DJF, the frequency of MJO activity, transition to the next phase and decay, for simulations with and without ENSO. Section 4 shows the MJO global anomaly patterns and precipitation anomalies over SA in the model without ENSO and

their biases. Section 5 shows the MJO global anomaly patterns and the precipitation anomalies over SA in EN and LN years in the model. The summary and conclusions are presented in Section 6.

2. Methodology

2.1. Model set-up

The coupled model MetUM-GOML3 comprises the MetUM atmospheric model coupled to a simplified one-dimensional ocean model, the Multi-Column *K* Profile Parameterization boundary-layer model (MC-KPP, based on Large et al. 1994), via the Ocean Atmosphere Sea Ice Soil (OASIS) coupler (Craig et al. 2017). One MC-KPP column is placed under each atmospheric gridpoint. MC-KPP has a 1000 m vertical domain with 100 unevenly spaced points, with the highest vertical resolution near the surface (~1 m) increasing to 25 m below 300 m.

As MC-KPP simulates only vertical mixing, temperature and salinity corrections are required in climate-length simulations to account for missing ocean dynamics and to adjust for biases in atmospheric surface fluxes (Hirons et al. 2015). The flux-correction technique constrains the mean seasonal cycle of temperature and salinity throughout the ocean column, without damping variability. The corrections are applied throughout each coupled ocean column and at each time step. The corrections are computed from an initial "tendency simulation" in which the MetUM-GOML3 is relaxed towards the target ocean climatology, with a timescale of 15 days. We use the 1980-2009 climatology from the Met Office (UKMO) ocean analysis (Smith and Murphy 2007), with the addition of a repeating ENSO cycle in some simulations (see Section 2.2). The daily climatology of temperature and salinity corrections is computed from the output of this "tendency simulation", smoothed with a 31-day running mean to remove high-frequency variability, and applied in a subsequent "free simulation" to constrain the basic state temperature and salinity. The free simulation has no relaxation and can be integrated effectively infinitely without drift. We analyse the output of these free simulations.

MetUM-GOML3 differs from MetUM-GOML1 (Hirons et al., 2015) and MetUM-GOML2 (Peatman and Klingaman, 2018) only by the atmospheric GCM: MetUM-GOML3 uses the MetUM Global Atmosphere 7.0 (GA7; Walters et al. 2019), whereas MetUM-GOML1 uses Global Atmosphere 3.0 and MetUM-GOML2 uses Global Atmosphere 6.0.

GA7 has 85 levels in the vertical and a model lid at 85 km. Further details on MetUM-GOML3 can be found in Hirons et al. (2015) and Peatman and Klingaman (2018).

2.2. Simulations

Simulations are performed at two horizontal resolutions: 1.875° x 1.25°, the lower resolution (called N96 in MetUM), with 200 km spacing between each longitude at the equator; and 0.83° x 0.56°, the higher resolution (called N216), with 90 km spacing between each longitude at the equator. A control MetUM-GOML3 simulation is performed at each resolution, with MC-KPP constrained to the 1980-2009 ocean climatology: 30 years long at N96 and 60 years long at N216. There is no ENSO in these simulations, as MC-KPP does not simulate ocean dynamics. Temperature and salinity corrections for these control simulations are computed from a 10-year tendency simulation at each resolution.

To isolate the effect of ENSO on the MJO (Section 5), ENSO cycles are imposed in MetUM-GOML3 in similar experiments to those described in Klingaman and DeMott (2020). We compute one-year climatologies (May-April, to mimic the "ENSO year") from the Smith and Murphy (2007) dataset for NT, EN, and LN conditions, based on terciles of the Niño 3.4 index in 1980-2009. These climatologies are concatenated (in order EN, LN, NT) to form a three-year composite ENSO cycle. At each resolution, we perform a 31-year tendency simulation, nudging to this three-year repeating ENSO cycle, to derive ten-year climatologies (May-April) of corrections for each ENSO state. Then, at each resolution we perform a 61-year free simulation imposing the corrections to obtain 20 complete 3-year cycles of May-April data. These free simulations provide robust statistics of simulated MJO impacts on SA across many ENSO events. For more information on this technique, refer to Klingaman and DeMott (2020).

Control simulations, without ENSO, are named "N96" and "N216" (Table 1). Simulations with ENSO are named "N96-ENSO" and "N216-ENSO". N96-ENSO and N216-ENSO are partitioned into EN and LN composites (e.g., N96-EN), according to simulated EN and LN years.

2.3. Datasets

To validate simulated precipitation, rain gauge daily precipitation data, between 1979 and 2009, from the Brazilian Water Agency (ANA) and other hydrometeorological institutes

from SA are analyzed. The data are verified to control systematic and aleatory errors. The Liebmann and Allured (2005) gridded precipitation data covers the extreme northern SA. Both precipitation datasets are gridded to 1°.

We validate simulated outgoing longwave radiation (OLR) against the Liebmann and Smith (1996) satellite-based dataset. The streamfunction is computed (Dawson 2016) from the MetUM-GOML3 wind output and reanalysis output from the European Centre for Medium-Range Weather Forecasts (ECMWF) (ERA-Interim reanalysis data, Dee et al. 2011). All observed and reanalysis data are analyzed for 1979-2009. The MJO tropical and extratropical teleconnections towards SA in the ERA-Interim reanalysis streamfunction data are consistent with those from the NCEP/NCAR reanalysis data, assessed by Grimm (2019) and Fernandes and Grimm (2021).

2.4. Methods

2.4.1. ENSO states

Observed ENSO states are classified by the first rotated mode obtained from Principal Component Analysis (PCA) applied to 1950-2009 DJF global monthly sea surface temperature (SST) anomalies (HadISST1 dataset, Rayner et al. 2003), gridded to 5°. The PCA is based on a correlation matrix; Varimax rotation is used to obtain orthogonal rotated variability modes associated with different physical processes (Wilks 2006). Factor scores above (below) 0.75 (-0.75) define the EN (LN) state, with the remainder (between -0.74 and 0.74) classified as NT. The classification results in 8 EN, 10 LN, and 14 NT years (Table 1 of Fernandes and Grimm 2021).

As MetUM-GOML3 is forced with a 3-yr repeating ENSO cycle, it is straightforward to partition N96-ENSO and N216-ENSO by terciles of the DJF mean monthly 1.5-meter temperature anomalies in the Niño 3.4 region (averaged 5°S-5°N, 170°-120°W, Fig. 1). From the 60 DJF periods in the 61-year simulations (Table 1), the warmest twenty seasons are selected as EN, the coldest twenty as LN, and the remaining twenty as NT.

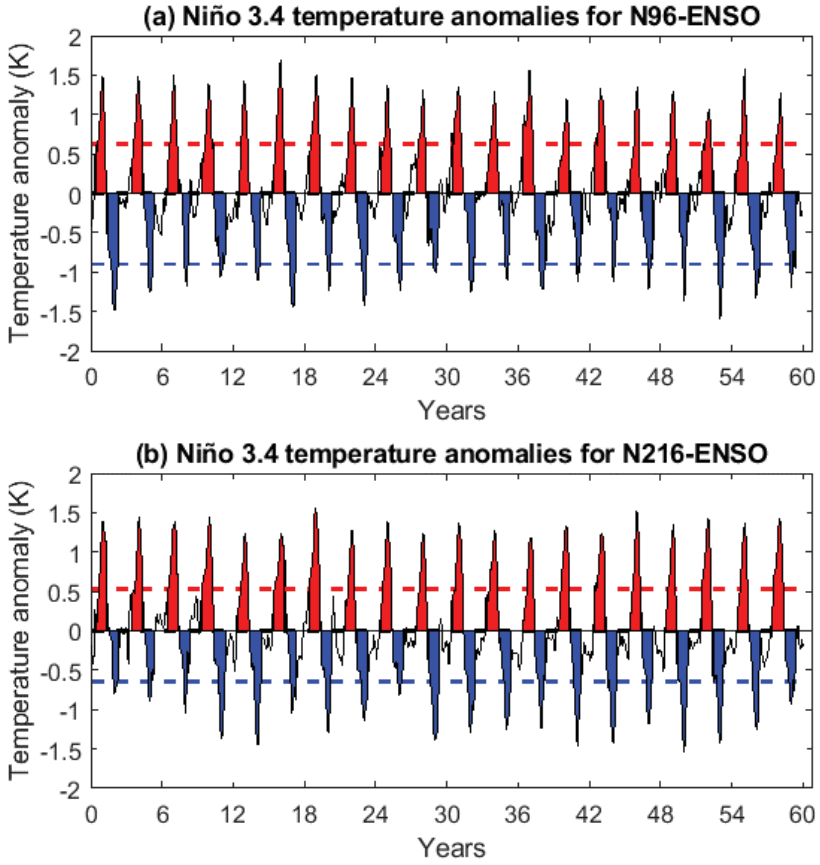

Figure 1: Timeseries of the Niño 3.4 1.5-meter temperature anomalies (°C) in (a) N96-ENSO and (b) N216-ENSO. Shading shows the May-April periods selected for the (red) El Niño and (blue) La Niña composites. The red and blue dashed lines show the thresholds for El Niño and La Niña composites, respectively. These thresholds are applied to the December-February mean index.

Table 1: For each simulation, the name used in the text, the grid spacing, the length of the simulation, and the target ocean state to which the model is constrained.

Name	Grid	Length	Target ocean state
N96	200 km	30 years	Smith and Murphy (2007)
N216	90 km	60 years	Smith and Murphy (2007)
N96-ENSO	200 km	60 years	3-year ENSO cycle
N216-ENSO	90 km	60 years	3-year ENSO cycle

2.4.2. MJO phases

MJO phases are defined by the Real-time Multivariate MJO (RMM) indices of Wheeler and Hendon (2004). The RMM1 and RMM2 indices are computed by projecting the OLR and zonal winds at 850 hPa and 200 hPa onto the first pair of combined empirical orthogonal functions (EOFs), computed from data averaged over 15°S-15°N, after removing the mean and first three harmonics of the annual cycle and the mean of the previous 120 days. For observations, we use the NOAA satellite OLR data (Liebmann and Smith 1996), and the ERA-Interim reanalysis wind data, to match with the ERA-Interim dataset used elsewhere in this study (Section 2.3). Simulated RMM indices are computed by projecting model data onto the EOFs derived from NOAA and ERA-Interim data.

The eight MJO phases are bounded by 45° intervals of the phase angle $\theta = \tan^{-1}\left(\frac{RMM2}{RMM1}\right)$. The MJO amplitude, for MetUM-GOML3 and observations, is defined by $A = [(RMM1)^2 + (RMM2)^2]^{\frac{1}{2}}$. When $A \geq 1$, the MJO is active; when $A < 1$, the MJO is neutral or inactive. Probabilities of MJO activity, propagation (transition to the next phase anti-clockwise), and decay (transition to the unit circle) are computed for all RMM phases and each phase separately, following Klingaman and Woolnough (2014a) and Klingaman and Woolnough (2014b).

2.4.3. MJO phases composites

Composite anomalies are calculated for each MJO phase as in Grimm (2019), further categorized according to ENSO status (EN or LN), as in Fernandes and Grimm (2021). Composites made for periods when both ENSO and MJO are active describe more efficiently the patterns than simple linear combinations of separate ENSO and MJO composites (Roundy et al. 2010). Daily anomalies are computed relative to a daily climatology that is smoothed with a 31-day running mean to remove spurious variance. The anomalies are filtered (Duchon 1979) by a 20-90 day window, using 211 weights. The filtered anomalies contain intraseasonal variability mainly related to the MJO, excluding effects from other time scales (synoptic, interannual, interdecadal), since our goal is the ENSO effect on the MJO rather than the sum of the MJO and ENSO-related anomalies.

We consider only DJF anomalies because DJF is the peak of not only the monsoon over most of SA, but also the ENSO, the MJO (Hendon et al. 1999; Slingo et al. 1999), and

the most substantial MJO impacts on SA (Alvarez et al. 2015; Grimm 2019). Also, the ENSO and MJO have different rainfall responses over SA in spring and summer (Grimm 2003, 2004; Alvarez et al. 2015), which argues against analyzing an extended six-month warm season. The statistical significance of the composites is assessed with the Student's *t*-test to verify whether the sample mean for each MJO phase and ENSO category in the composites is similar to the sample mean from all DJF days. The null hypothesis is rejected if the sample means are different (Wilks 2006). As the time series are serially correlated, it is crucial to evaluate the effective sample size $n = N\left(\frac{1-\rho_1}{1+\rho_1}\right)$, in which N is the original sample size, and ρ_1 is the lag-1 autocorrelation coefficient (Wilks 2006).

Biases and differences between the two resolutions (N216-N96) are shown in the composites. The precipitation and streamfunction data are interpolated in observations and N216 onto the common coarser N96 grid; simulated OLR is interpolated onto the 2.5° grid of the observations (Liebmann and Smith 1996). The t-test is applied to simulated and/or observed sample means for each MJO phase to test the significance of biases.

3. MJO activity

3.1. MJO activity in N96 and N216

In both N96 and N216, the model produces strong MJO on 62% of all DJF days (Fig. 2b-c), slightly lower than the 66% observed (Fig. 2a). The MJO activity decreases to 59-61% for all days in the year in the model and 64% in observations (not shown). Klingaman and Woolnough (2014a) found a similar percentage (61%) in MetUM-GOML1. The MJO phase frequencies range between 7% and 8.5% on all days in a year in both datasets (see Fig. 1a-e of Klingaman and Woolnough 2014a). However, in DJF, observed frequencies range between 4.5% (phase 1) and 13% (phase 7).

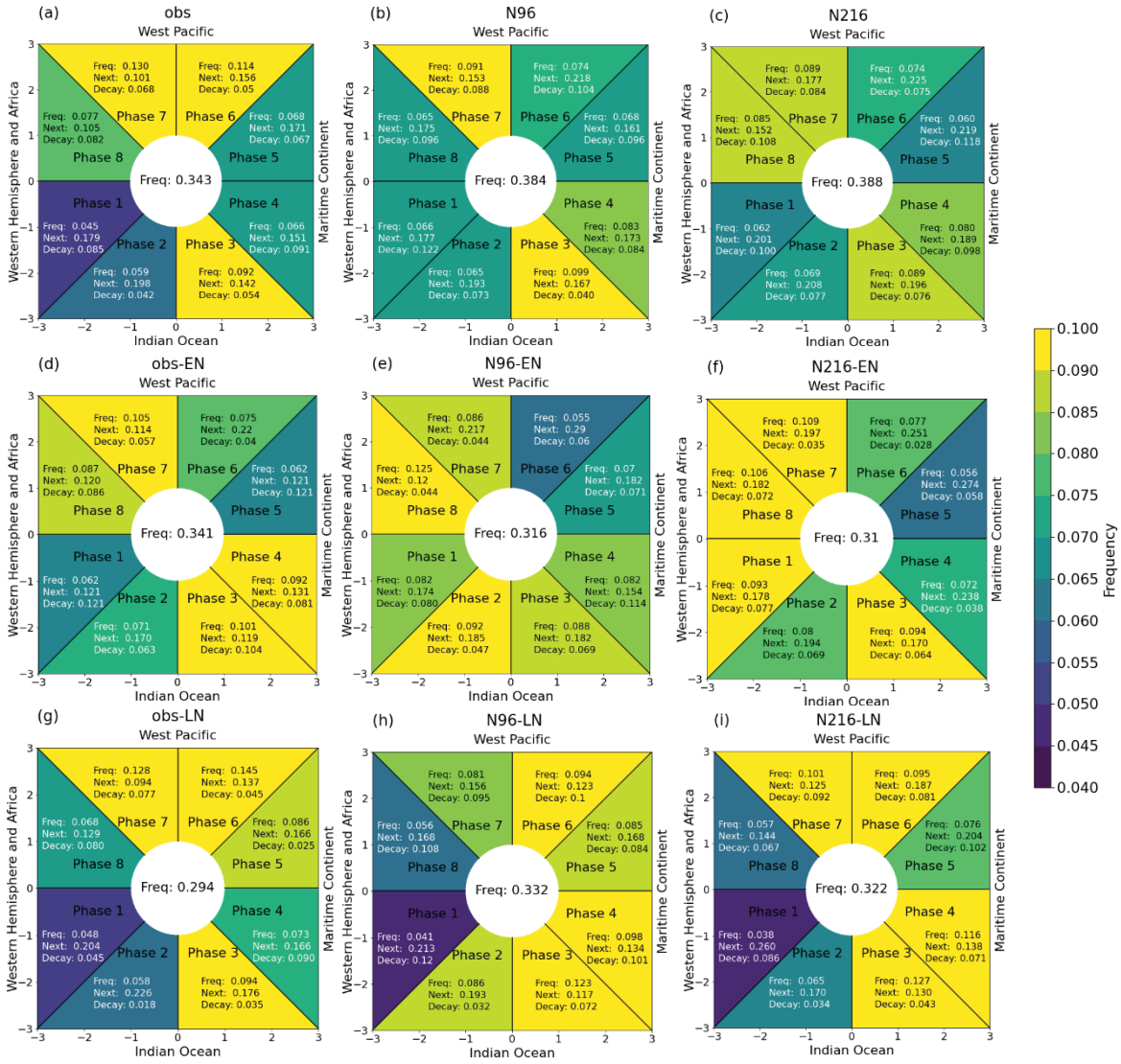

Figure 2: Fraction of MJO days in which amplitude is ≥1 (or strong MJO activity) in (a) observations (obs) (1979-2009), (b) N96, and (c) N216, during austral summer. (d-f) and (g-i) show the MJO activity like (a-c), but for N96-ENSO and N216-ENSO and only in EN year (d-f) and LN (g-i) years, respectively. The colored wedges show the daily frequency of the strong activity in each phase, relative to all DJF days, using the color bar. For each phase, the decimal fractions show the probability of MJO activity in that phase ('Freq'), as well as probabilities that, on the day following strong activity in that phase, the MJO transitions to the next (anticlockwise) phase ('Next') or moves into the unit circle ('Decay', i.e. amplitude <1). The frequency of weak MJO (amplitude <1) is given inside the unit circle.

The most frequent active MJO phases in DJF (Fig. 2a) are 7, 6, and 3, as shown by Fernandes and Grimm (2021) and Grimm et al. (2021) with RMM indices from NCEP/NCAR reanalysis. The less frequent active MJO phases are 1-2, followed by 4-5. This agrees with the distribution of ending (lysis) longitudes of tracked MJO events in Zhang and Ling (2017). The increased MJO activity in phases 6-7 (3) is related to active (suppressed) MJO events that

propagate through the Maritime Continent (MC) in phases 4-5 (1-2) and partly recover their strength near 180°.

The model reproduces well the observed MJO frequencies in DJF, with phases 3 and 7 more frequent (9%) (Fig. 2b-c). Hence, there are numerous MJO events in the model propagating through the MC in phases 1, 2, 4, 5. The model also shows decreased MJO activity in phases 1-2, though higher than observed. Remarkably, the MC barrier effect (Zhang and Ling 2017) to MJO activity is delayed to phases 5-6 in the model. MJO activity is not sensitive to horizontal resolution.

The probabilities of MJO decay and transition to the next phase are higher in the model (Fig. 2b-c) than observed (Fig. 2a). Higher transition probabilities suggest a faster simulated MJO propagation than observed, which can weaken extratropical teleconnections (Wang et al. 2020b). In phases 5-6, the MJO weakens as it moves from the MC to the western Pacific (WP), leading to a decay 50-100% greater in the model than observed, consistent with the exaggerated MC barrier effect in CGMs (Vitart and Molteni 2010; Kim et al. 2018). The decay in phases 5-6 in the model affects the frequency of MJO phase 7 (9%), which is smaller than observed (13%), although still the most frequent, along with phase 3 (9%)

3.2. MJO activity in each ENSO state

MJO frequencies conditioned on ENSO state show that active ENSO slightly increases DJF MJO activity in MetUM-GOML3 and observations (Fig. 2). The frequencies slightly decrease in NT years (not shown). Hence, interannual variability does not substantially affect global MJO activity (Hendon et al. 1999; Slingo et al. 1999). However, the simulated ENSO-related anomalies in DJF affect the relative occurrence of MJO phases, with similar patterns of circulation anomalies as found in Fernandes and Grimm (2021) for observations. Previous studies have shown a zonal shift of the MJO activity during ENSO over the equatorial Pacific Ocean in observations (Hendon et al. 1999) and AGCMs (Tam and Lau 2005).

There are similarities between EN/LN states and specific MJO phases concerning the strongest anomalies of Walker circulation over the equatorial eastern Indian Ocean (IO)-WP and the central Pacific. For instance, phases 8-2 (5-6) are more (less) frequent in MetUM-GOML3 and observations in EN (Fig. 2d-e-f) due to enhanced (suppressed) convection over the equatorial central Pacific (eastern IO, MC-WP). Phases 8-2 are more frequent in the MetUM-GOML3 than observations in EN because in MetUM-GOML3 more EN events

exceed ±0.8°C in the equatorial central-eastern Pacific (Fig. 1), favoring increased evaporation and moist static energy to enhance MJO convection. On the other hand, phases 4-6 (8-2) are more (less) frequent in LN (Fig. 2g-h-i) as the circulation features are opposite to those described in EN. These ENSO-driven changes in the MJO activity favor the model's enhancement of these MJO anomalies during EN and LN states in Section 5 (Roundy et al. 2010).

Decay probabilities are smaller in EN (Fig. 2e-f) than in simulations without ENSO (Fig. 2b-c). It indicates the EN state improves simulated eastward propagation in MetUM-GOML3, mainly in phases 5-6 when the MJO is over the MC-WP. It seems the simulated MJO events in EN are more likely to move east in the WP after the MC, until they reach colder SSTs. Klingaman and DeMott (2020) found the EN state greatly improved MJO propagation in a coupled version of the Super-Parameterized Community Atmospheric Model (SPCAM3), with the same oceanic model configuration as the MetUM-GOML3.

4. MJO and its impacts in N96 and N216

4.1. Global anomaly patterns associated with MJO

4.1.1 The simulated MJO

This section shows the global evolution of the MJO tropical convection and associated circulation and the description of the MJO impacts on SA in MetUM-GOML3 at lower (N96) and higher (N216) spatial resolution. Grimm (2019) composites are duplicated here as observations (Figs. 3a, 4a, 5a, 6a) using ERA-Interim. The main aspects discussed below are common to both horizontal resolutions. The model represents well the eastward propagation of the MJO. However, the convection is further east than observed when the MJO moves from the IO to the MC-WP (Fig. 3b-c, phases 3-4, phases 5-6 not shown). Differences in the eastward MJO propagation are also evident in displaced streamfunction quadrupoles (Figs. 4, 5), associated with Rossby and Kelvin equatorial waves (Matsuno 1966), and in the MJO Hovmoller diagrams (Fig. 6).

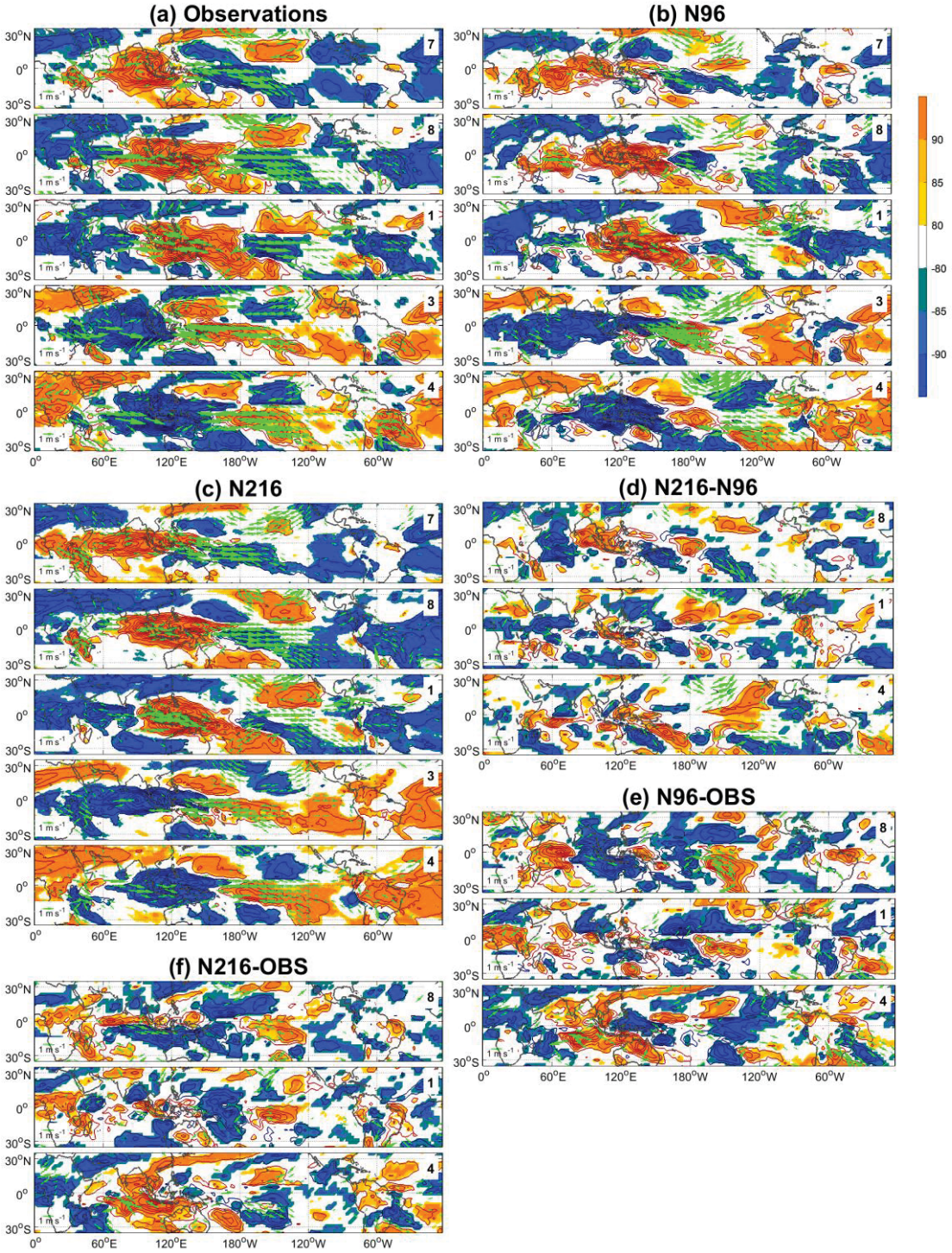

Figure 3: Composite anomalies of OLR and 850 hPa winds in MJO phases 7, 8, 1, 3, 4 in (a) observations (OBS), (b) N96, (c) N216. Differences between the anomalies of OLR and 850 hPa winds in MJO phases 8, 1, 4 for (d) N216-N96, (e) N96-OBS, (f) N216-OBS. Contour interval is 2.5 Wm^{-2}. The color bar indicates confidence levels, with signs indicating positive or negative OLR anomalies. Only wind anomalies (ms^{-1}) with confidence levels better than 80% are shown.

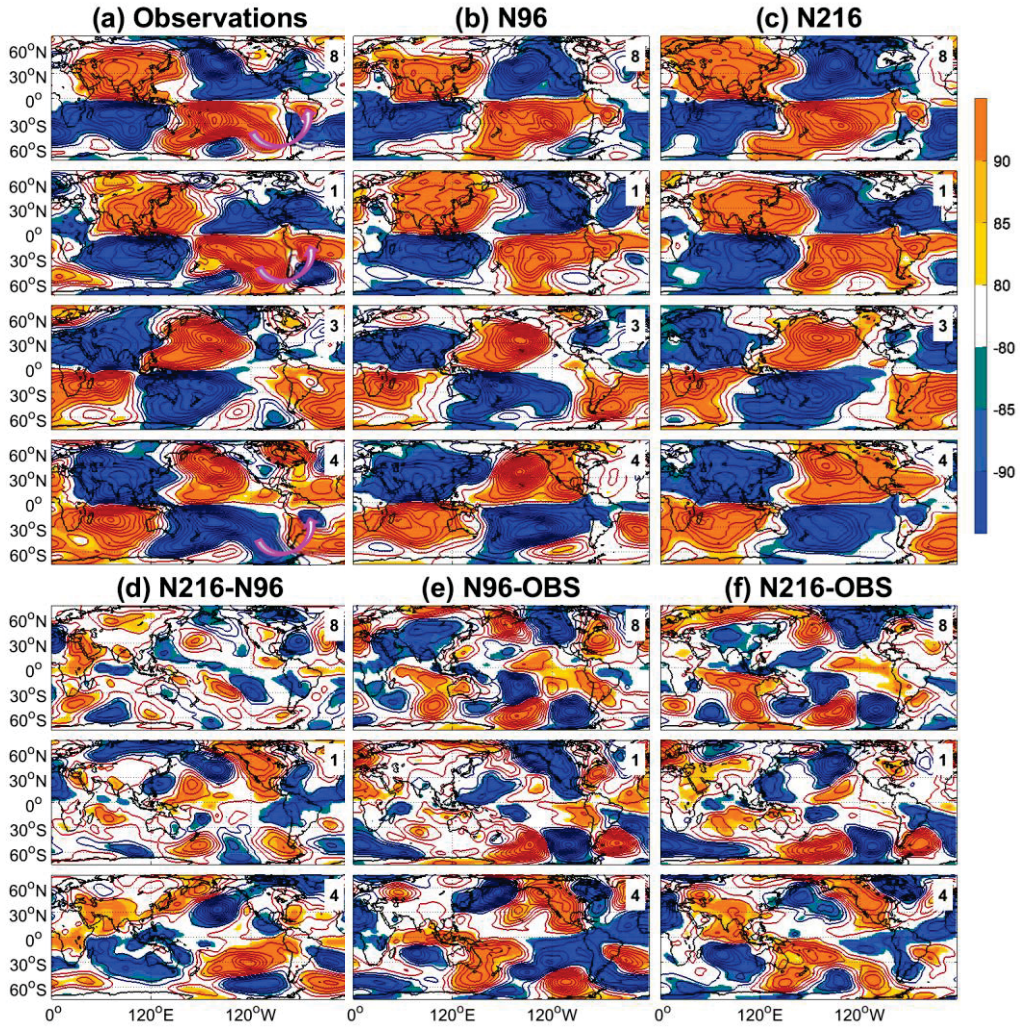

Figure 4: Composite anomalies of the 850 hPa streamfunction in MJO phases 8, 1, 3, 4 in (a) observations (OBS), (b) N96, (c) N216. Contour interval is $3 \times 10^5 m^2 s^{-1}$. Differences between the anomalies of 850 hPa streamfunction, in MJO phases 8, 1, 4 for (d) N216-N96, (e) N96-OBS, (f) N216-OBS. Zero line is omitted. The color bar indicates confidence levels of streamfunction anomalies, with signs indicating positive or negative anomalies.

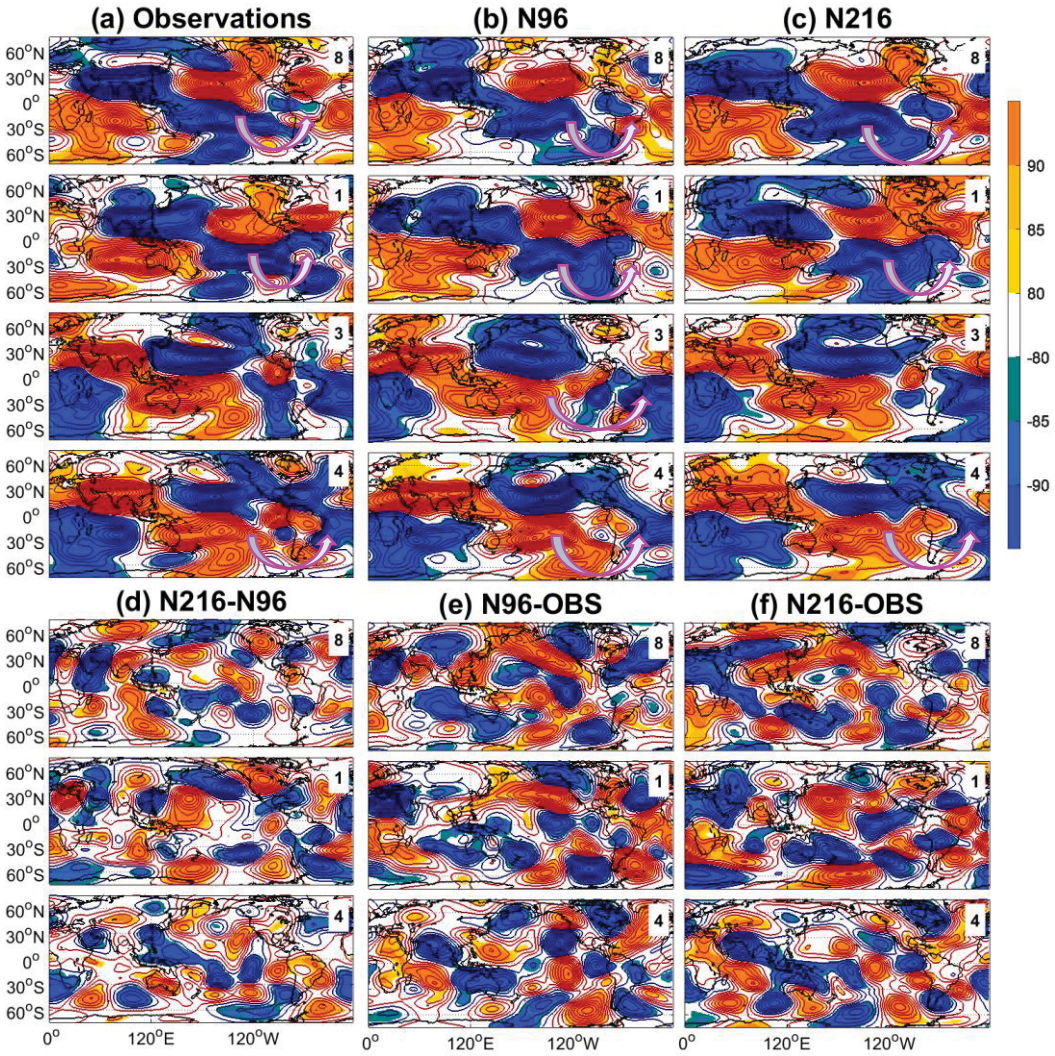

Figure 5: Composite anomalies of the 200 hPa streamfunction in MJO phases 8, 1, 3, 4 in (a) observations (OBS), (b) N96, (c) N216. Contour interval is $6 \times 10^5 m^2 s^{-1}$. Differences between the anomalies of 200 hPa streamfunction, in MJO phases 8, 1, 4 for (d) N216-N96, (e) N96-OBS, (f) N216-OBS. Zero line is omitted. The color bar indicates confidence levels of streamfunction anomalies, with signs indicating positive or negative anomalies.

The weak simulated IO low-level westerlies and streamfunction anomalies (Figs. 3b-c and 4b-c, phases 3-4, phase 2 not shown) indicate weakened equatorial Rossby waves propagating westwards, known to slow eastward MJO propagation (Chen and Wang 2018). On the other hand, the model simulates well the magnitude of equatorial Kelvin-wave easterly anomalies. The easterlies reduce stability east of the convective center by increasing boundary layer convergence and promoting congestus convection, leading to eastward MJO propagation through the MC (Chen and Wang 2018). As the dynamical wave feedbacks of both waves determine the eastward MJO propagation (Liu and Wang 2017), weakened Rossby waves may contribute to the further eastward propagation.

For a fixed MJO phase, the eastward displaced simulated OLR anomalies in the IO-WP is visible in the more horizontal slope of the Hovmoller diagrams, between 60°E-160°E (red dashed lines, Fig. 6a-b-c). On the other hand, the model satisfactorily represents the MJO activity from the RMM indices (previous section), which are primarily determined by the circulation (Straub 2013). Hence, there is an error in the convection-circulation phase relationship, since MetUM-GOML3 displaces the convection but achieves the same RMM phase.

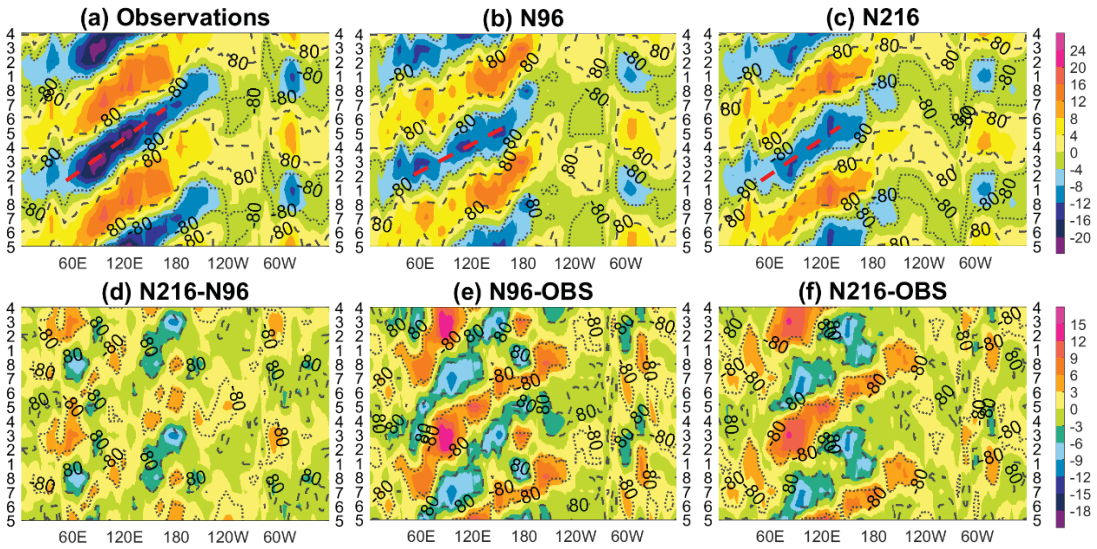

Figure 6: Time-longitude Hovmoller diagrams of 0°-15°S averaged OLR anomalies (Wm^{-2}) for (a) observations (OBS), (b) N96, (c) N216, (d) N216-N96, (e) N96-OBS, (f) N216-OBS. The dotted and dashed lines delimit the significant values with confidence levels > 80%.

The OLR anomalies are weaker in the model than observations (Figs. 3 and 6), a common issue in climate models (Kodama et al. 2015; Liu et al. 2017; Coelho et al. 2020). Both simulations reproduce the low-level tropical quadrupole (Fig. 4b-c), with the pair of cyclonic (anticyclonic) anomalies straddling the equator west (east) of the heating zone (or maximum convection, Fig. 3b-c). The baroclinic response in the tropical quadrupole appears between low and high levels (Figs. 4b-c, 5b-c). The OLR and low-level wind anomalies (Fig. 3b-c) are simulated southwards, consistent with the DJF MJO position.

4.1.2 The simulated MJO impacts on SA through teleconnections

MetUM-GOML3 produces earlier, in phase 8, the extratropical teleconnection (Fig. 5b-c) and its strongest impacts on SA, associated with enhanced (suppressed) convection in the SACZ (SESA) (Fig. 3b-c). Only convection in phase 8 resembles the SACZ shape,

extending towards the subtropical South Atlantic. The ECMWF and NCEP AGCMs also show this phase shift of the maximum extratropical teleconnection and its impacts on SA (Grimm et al. 2021). Also, the tropical teleconnection between the eastern Pacific and SA, which affects tropical CESA precipitation anomalies, is established earlier in MetUM-GOML3 (phase 8, Fig. 4b-c). In observations, the tropical and extratropical teleconnections to SA are fully established in phase 1 (Figs. 4a, 5a) (Grimm 2019).

Figures 4b-c and 5b-c show simulated extratropical teleconnections, indicated by their barotropic action centers (and curved arrows), stronger and more correctly positioned in phase 8 than 1, which differs from observations (Figs. 4a, 5a). The simulated circulation anomalies are more significant in phase 8 than 1, such as the anomalous upper-level extratropical anticyclone - subtropical cyclone over SA.

The simulated MJO convection (and low-level convergence) over the central-east subtropical SP lasts from phase 7 through phase 8 (Fig. 3b-c), weakening in phase 1 more than observed (Fig. 3a). Consequently, the extratropical teleconnections weaken in phase 1 (Fig. 5b-c), restricting the strongest negative OLR anomalies to equatorial North-Northeast Brazil (Fig. 3b-c), where they last until phase 2 (not shown). The wavetrain fades in phase 2, associated with fading anomalous convection over the source region and consistent with observations (not shown).

Three main factors shift the extratropical teleconnection to SA from phase 1 to phase 8 in MetUM-GOML3. (i) The eastward shift in convection for a given MJO phase with respect to observations, which means that simulated convection arrives at a given location “earlier” (in RMM phase space) than observed. As in Grimm et al. (2021) for the ECMWF and NCEP models, (ii) the conditions over the source region to excite teleconnections and establish the wavetrain happen almost simultaneously in the model (phase 8), whereas observations show a one-phase lag between convective initiation (phase 8) and the teleconnection peak (phase 1) (Grimm 2019). (iii) Weaker simulated negative OLR anomalies over the source region in phase 1 than observed (Fig. 3), which weakens the simulated teleconnection pattern.

In phase 4 (Fig. 3b-c), the model reproduces the opposite features over the source region to those in phase 8, associated with the phase 4 extratropical teleconnection to SA (Fig. 5b-c) (Fernandes and Grimm 2021). It is noteworthy that the model simulates the wavetrain in the expected MJO phase, probably because there is no phase lag between the suppressed

convection over the source region (Fig. 3a) and the teleconnection (Fig. 5a) in observations. The simulated teleconnection favors suppressed (enhanced) convection in the SACZ (SESA), coherent with observations. There is a significant anomalous coupled upper-level extratropical cyclone-subtropical anticyclone over SA in MetUM-GOML3 and observations. The anticyclonic circulation is over subtropical South Atlantic rather than over the continent as phase 8.

The streamfunction anomalies between the extratropical eastern SP and the southern tip of SA, associated with barotropic action centers of the extratropical teleconnection, are weaker in the model than observed (phases 8, 1, 4, Figs. 4b-c and 5b-c). There are more significant streamfunction biases in the extratropics than in the tropics (Figs. 4e-f and 5e-f), at upper and lower levels.

4.1.3 The effect of horizontal resolution

Despite similar overall MJO characteristics in N96 and N216 (section 3), N216 improves some aspects of the MJO and its impacts on SA. Increasing resolution enhances the equatorial convection a little east of 180° (Fig. 6c-d). Also, N216 enhances convection over the source region for extratropical teleconnection to SA (Grimm 2019), better simulating the observed features in this region (phases 7-8, Fig. 3c). Significant N216-N96 differences in the negative OLR and low-level wind anomalies appear in the source region (phase 8, Fig. 3d).

Biases (Fig. 3e-f) show that the SA convection and low-level wind anomalies associated with the MJO are better simulated in both resolutions in phase 8 than phase 1. Increased horizontal resolution is important to better reproduce SESA convection and low-level wind anomalies in phase 4 and phase 1 (Figs. 3b-c-d). In general, the biases in the convection anomalies over SA are smaller for N216 than for N96 (Figs. 3e-f). There are also smaller significant biases in N216 (Fig. 4f) than in N96 (Fig. 4e) in the low-level streamfunction anomalies between the eastern SP and the South Atlantic. By contrast, there are smaller significant biases in N96 (Fig. 5e) than N216 (Fig. 5f) in the upper-level streamfunction anomalies over the same regions, suggesting that higher resolution worsens the upper-level extratropical teleconnections.

Previous studies have found an eastward displacement of the PNA teleconnections due to a stronger and eastward extended North Pacific westerly jet, a common GCM bias (Henderson et al. 2017; Wang et al. 2020a, 2020b). The SA westerly jet weakens and shifts

southwards in DJF. It is stronger in MetUM-GOML3 than observed (purple contours in Fig. S1), as Hirons et al. (2015) described for MetUM-GOML1.

There is no significant difference in the climatological zonal wind at 200 hPa in DJF between N96 and N216 (not shown). However, the propagation of the extratropical teleconnection in the model still depends on the intensity of the SA westerly jet. The jet strength differs between N96 and N216 through MJO phases 8, 1, 3 and 4. N96 has a stronger westerly jet than N216 over the extratropical SP and South Atlantic oceans (Fig. S1b-c). On the other hand, over the southern tip of SA and subtropical SA, the westerly jet is stronger in N216 (Fig. S1a). The southern tip is the entrance region for the teleconnection pattern, from where it is established in the subtropics (Grimm 2019).

Therefore, N216 shifts the extratropical teleconnection due to a stronger SA westerly jet. It is noticeable the teleconnections shift east at upper levels in N216 with respect to N96 (curved arrows, Fig. 5b-c). N216 shifts the upper-level anomalous circulation dipole eastwards over the subtropical South Atlantic (phases 8, 1, 4, Fig. 5c). In N96, the subtropical cyclonic (anticyclonic) anomaly is over (closer to) SA in phases 8-1 (3-4) (Fig. 5b), consistent with observations (Fig. 5a).

4.2. Precipitation anomalies over SA associated with MJO

Figure 7 shows the CESA and SESA locations, the precipitation anomalies over SA in MJO phases 8-4, and their biases in MetUM-GOML3. The precipitation anomalies are consistent with the OLR (Fig. 3) and circulation (Figs. 4, 5) anomalies. The better-resolved topography in N216 improves the low-level anomalous circulation dipole (Fig. 4c) and the moisture flux over SA, represented by the low-level wind anomalies (Fig. 3c). These features lead to an expanded anomalous precipitation dipole, in which the significant anomalies reach larger continental areas (phases 8, 1, 4, 5, phase 5 not shown) (Fig. 7c). Delworth et al. (2012) and Jung et al. (2012) found mean precipitation patterns over SA improved in coupled GCMs with increased horizontal resolution. The better-resolved topography may also help the CESA mountains to anchor the SACZ in its climatological position (Grimm et al. 2007) (phase 8, Fig. 7c). The precipitation anomalies are improved in N216, even with the extratropical teleconnection to SA slightly shifted east (Fig. 5c).

Simulated precipitation anomalies are significant over the whole CESA in phase 8, when both teleconnections are fully established (Fig. 4b-c, 5b-c). On the other hand, the

anomalies are insignificant over the SACZ in phase 1 (Fig. 7b-c) as the extratropical teleconnection weakens (Fig. 5b-c). The significant positive anomalies retreat to the north of CESA and equatorial NE Brazil in phase 1, consistent with weakened negative OLR anomalies (Fig. 3b-c) and tropical teleconnections (Figs. 4b-c).

The precipitation dipole extends further west in the model (Fig. 7b-c), over the monsoon core region (10°-20°S, 45°-55°W, red squares in Fig. 7e-f) and the Amazon in phases 8, 1, 4, 5 (phase 5 not shown). The MJO impacts are more significant in observations (Fig. 7a) in the central-eastern SA (CESA), a little east of the monsoon core region (Grimm 2019). MetUM-GOML3 shows significant positive biases in the Amazon and the monsoon core region (phases 8-1, Fig. 7e-f). The model overestimates the daily precipitation climatology in DJF over these regions, corroborating deSouza Custodio et al. (2017), with differences larger than 3 mm/day (not shown). It favors enhanced MJO precipitation anomalies, which range between +/- 5mm/day. On the other hand, the model underestimates the precipitation anomalies in CESA (phase 1) and in equatorial NE Brazil (phases 8-1) (Fig. 7e-f).

The most significant MJO positive precipitation anomalies in SESA, associated with the Mesoscale Convective Systems (MCSs), occur in phases 3-4 (Fig. 7a), weakening in phase 5 (not shown). N216 better represents these anomalies during phases 4-5 (Fig. 7c, phase 5 not shown) associated with improved convection and circulation anomalies (phase 4, Figs. 3d, 4c). Monerie et al. (2020) hypothesized that increased horizontal resolution in MetUM improved the representation of MCSs over SA. By contrast, significant positive precipitation anomalies appear in SESA in phase 3 in N96 (Fig. 7b). They are confined to smaller region and are associated with the earlier appearance of the extratropical teleconnections (Fig. 5b).

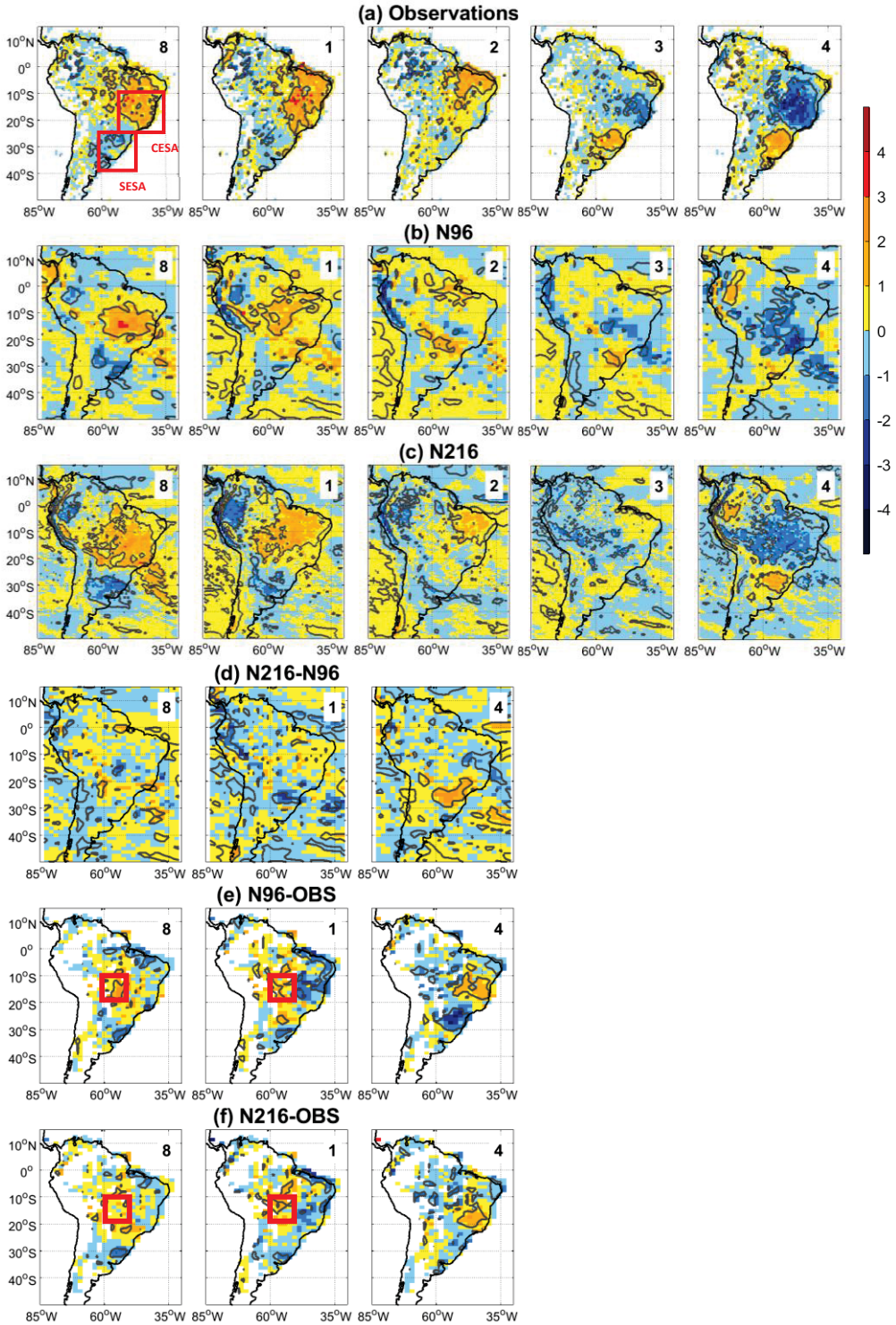

Figure 7: Composite anomalies of daily precipitation rate (color bar, $mm\ day^{-1}$), in MJO phases 8, 1, 2, 3, 4, in (a) observations (OBS), (b) N96, (c) N216. Differences between the anomalies of daily precipitation rate in MJO phases 8, 1, 4 for (d) N216-N96, (e) N96-OBS, (f) N216-OBS. Gray lines have anomalies with confidence levels better than 85%. The first map shows the CESA and SESA regions (red squares) cited in the text.

5. MJO impacts during El Niño and La Niña states

The following sections show the global anomalous MJO convection and circulation patterns in EN and LN in MetUM-GOML3 (Section 5.1) and related SA precipitation anomalies (Section 5.2). Fernandes and Grimm (2021) composites are duplicated here as observations (Figs. 8, 9, 10, 11, 12, 13) using ERA-Interim. We verify if the ENSO-driven background changes in MetUM-GOML3 influence the MJO and its impacts, not only in the frequency of individual MJO phases (Section 3.2) but in the MJO convection, circulation, and teleconnections affecting SA precipitation.

5.1. Global anomaly patterns associated with MJO in EN and LN

5.1.1 Influence of EN and LN states on the simulated MJO

In N96-ENSO and N216-ENSO, the global MJO OLR, wind at 850 hPa (Fig. 8c-d-e-f), and streamfunction anomalies (Figs. 9b-c-e-f and 10b-c-e-f) strengthen (weaken) in EN (LN) with respect to N96 and N216 (Figs. 3b-c, 4b-c, 5b-c). It is noticeable that the MJO strengthens (weakens) in EN (LN). For instance, the low-level westerlies of equatorial Rossby waves appear over Africa and the IO stronger in EN than in NT or LN years (phases 3-4, Fig. 8c-e), associated with the "drag effect" of these waves (Wang et al. 2018). The low-level easterlies of equatorial Kelvin waves and the suppressed convection over the WP (phases 3-4, Figs. 8c-e and 11b-c) are more significant in EN than LN, supporting MJO propagation (Kim et al. 2014; Chen and Wang 2018), as found in observations (Fernandes and Grimm 2021) and the atmosphere-mixed-layer-ocean coupled configuration of ECHAM4 (Wei and Ren 2019).

In addition, the OLR and U850 Hovmoller diagrams (Fig. 11) show that EN conditions produce the best simulated MJO eastward propagation, in agreement with Klingaman and DeMott (2020), as well as less MJO decay, mainly over the MC-WP (Fig. 2e-f). The magnitude of the equatorial OLR and U850 anomalies is closer to observations in EN than LN or simulations without ENSO (Fig. 6). The eastward displaced MJO enhanced convection over the IO-MC is visible in a gentler slope of the Hovmoller diagram between 60°E-160°E (red dashed lines, Fig. 11) in EN than LN. In other words, the MJO convection is further east in EN than LN from phase 3 through phase 5, as found in observations (Henderson and Maloney 2018; Fernandes and Grimm

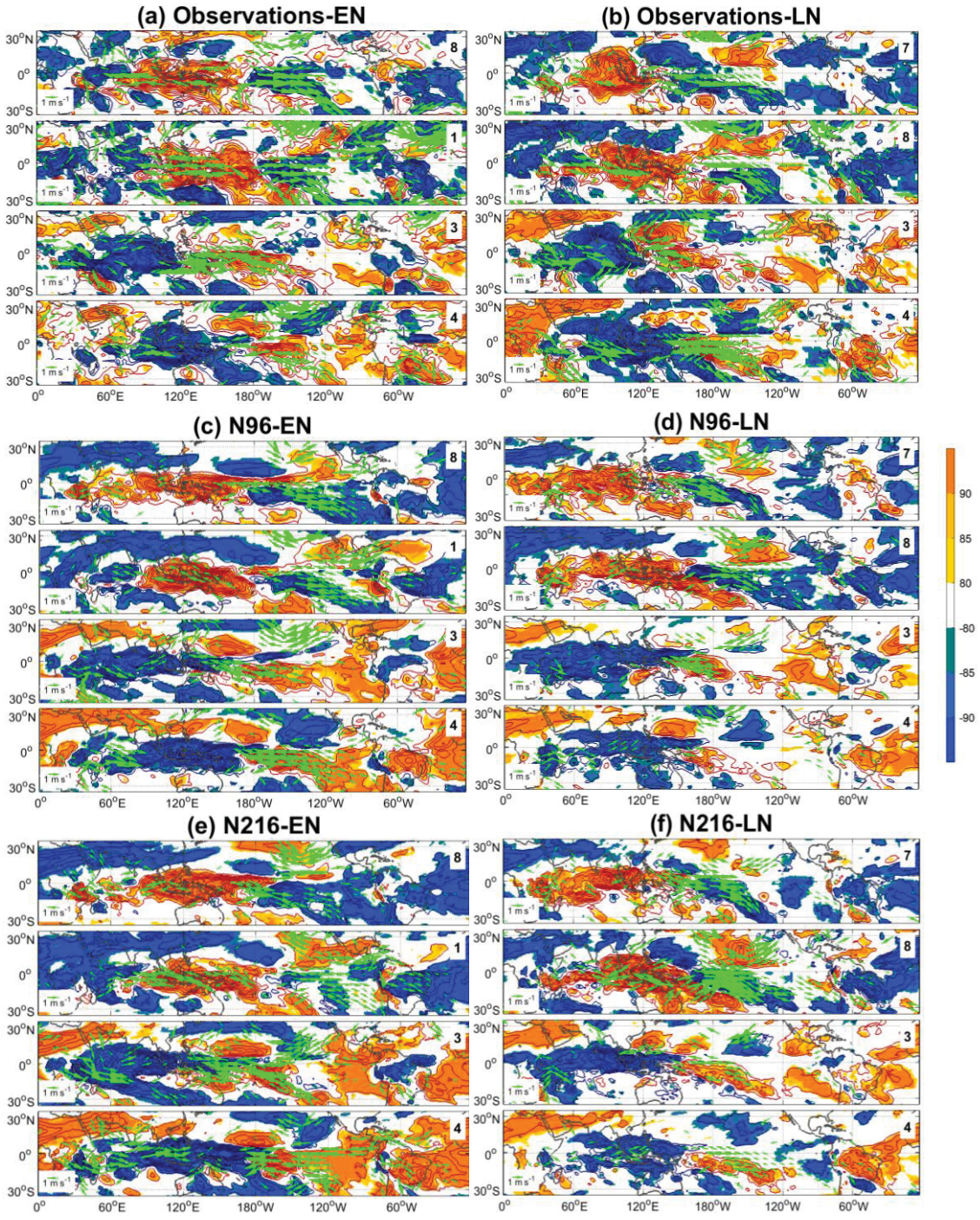

Figure 8: Composite anomalies of OLR and 850 hPa winds in MJO phases 8, 1, 3, 4 in (a) observations-EN, (c) N96-EN, (e) N216-EN, and in MJO phases 7, 8, 3, 4 in (b) observations-LN, (d) N96-LN, (f) N216-LN. Contour interval is 2.5 Wm^{-2}. The color bar indicates confidence levels, with signs indicating positive or negative OLR anomalies. Only wind anomalies (ms^{-1}) with confidence levels > 80% are shown.

2021) and the coupled configuration of ECHAM4 (Wei and Ren 2019). The simulated MJO suppressed convection weakens during LN (Fig. 11e-f) over the IO-MC, producing a standing oscillation near the MC. Therefore, the MC barrier effect (Zhang and Ling 2017), enhanced in GCMs (Vitart and Molteni 2010; Kim et al. 2018), is even more exaggerated in LN, mainly in N96-LN (not shown), consistent with the increased MJO decay in phases 5-6 in LN (Fig. 2h-i).

We hypothesize that the simulated EN strengthens moisture gradients near the MC, inducing more moisture advection by the stronger low-level wind anomalies during EN state (Fig. 8c-e), favoring MJO eastward propagation through the MC, as Wei and Ren (2019) showed for observations.

The increased spatial resolution in MetUM-GOML3 simulates the anomalous MJO and EN (LN) convection with the same (opposite) sign across the central Pacific during phases 6-7 (not shown). It increases (decreases) the subsidence over equatorial northeastern SA, enhancing (weakening) positive OLR anomalies in this region in N216-EN (N216-LN) (not shown). Furthermore, changes in the Walker circulation in N216-EN (N216-LN) decreases (increases) the ascent over the equatorial northeast SA, weakening (enhancing) the anomalous MJO convection in this region in phases 8-2 (Fig. 8e-f, shown only for phase 8, phases 1-2 not shown). The equatorial convection over SA in the Hovmoller diagrams is also more prominent in N216-LN than N216-EN (phases 8-2, Fig. 11c-f).

5.1.2 Influence of EN and LN states on the simulated MJO teleconnections and their impacts on SA

The MJO equatorial convection enhances east of 180° in EN (phases 6-1, Fig. 11a and Fig. 8 of Fernandes and Grimm), consistent with warm SST anomalies and anomalous ascent in the equatorial central-eastern Pacific (Hendon et al. 1999; Woolnough et al. 2000; Tam and Lau 2005). In the model, the convection remains just east of 180° in EN, consistent with observations-EN. However, the convection extends more to the east in N96-EN than N216-EN (Figs. 8c, e, for phases 8 and 1; Fig. 11b). On the other hand, the convection and the low-level westerlies stay longer a little east of 180° in N216-LN (Fig. 11f-l), likely linked to the higher resolution, as the convection was further east in N216 than N96 (Fig. 6). Therefore, we hypothesize that the anomalous equatorial convection east of 180° in N96-EN and N216-LN, which is more prominent than in simulations without ENSO (Fig. 6b-c), increases the

probability of enhanced convection over the source region to efficiently trigger the teleconnections towards SA in phases 8-1.

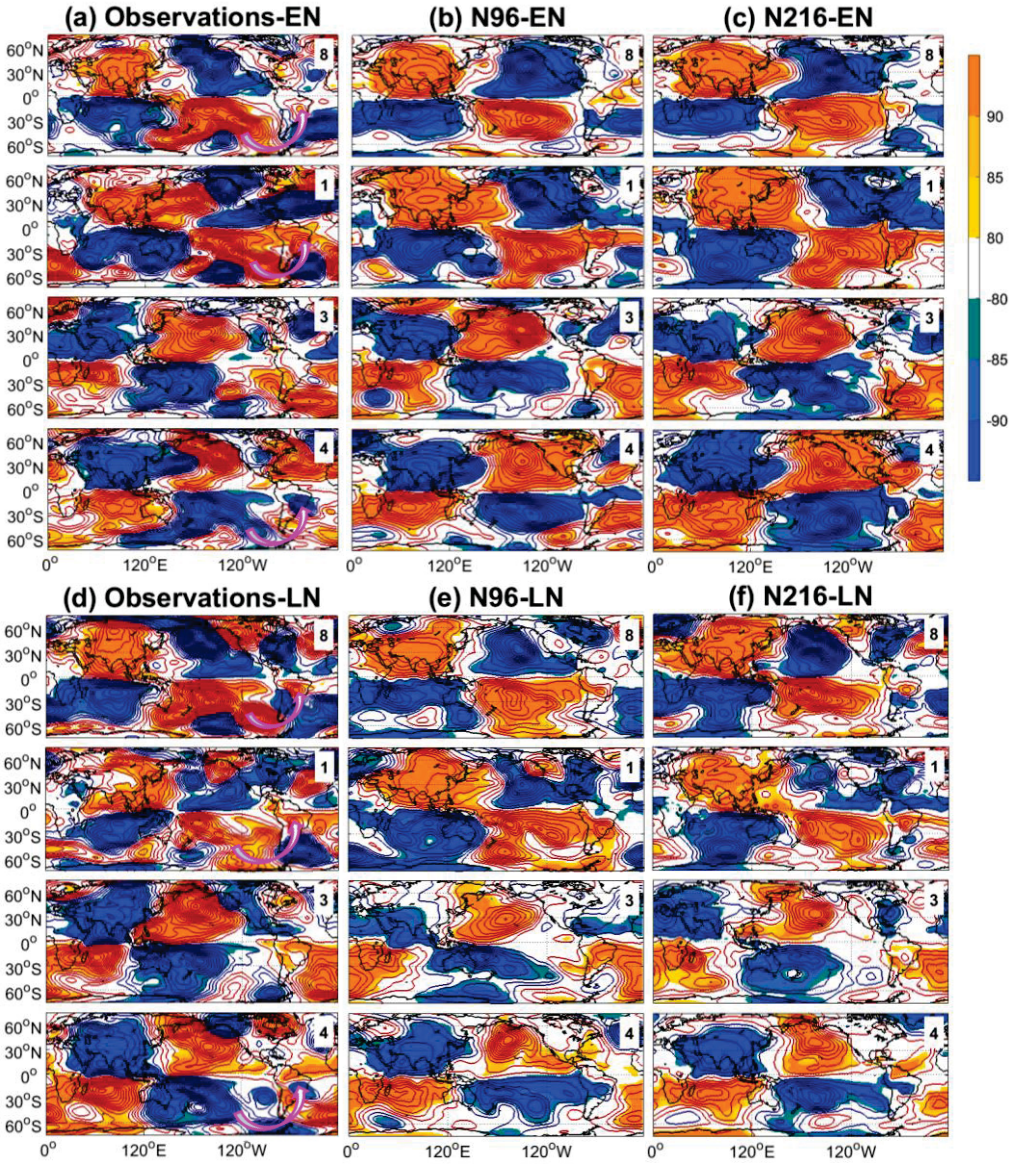

Figure 9: Composite anomalies of the 850 hPa streamfunction in MJO phases 8, 1, 3, 4 in (a) observations-EN, (b) N96-EN, (c) N216-EN, (d) observations-LN, (e) N96-LN, (f) N216-LN. Contour interval is $3 \times 10^5 m^2 s^{-1}$. Zero line is omitted. The color bar indicates confidence levels of streamfunction anomalies, with signs indicating positive or negative anomalies.

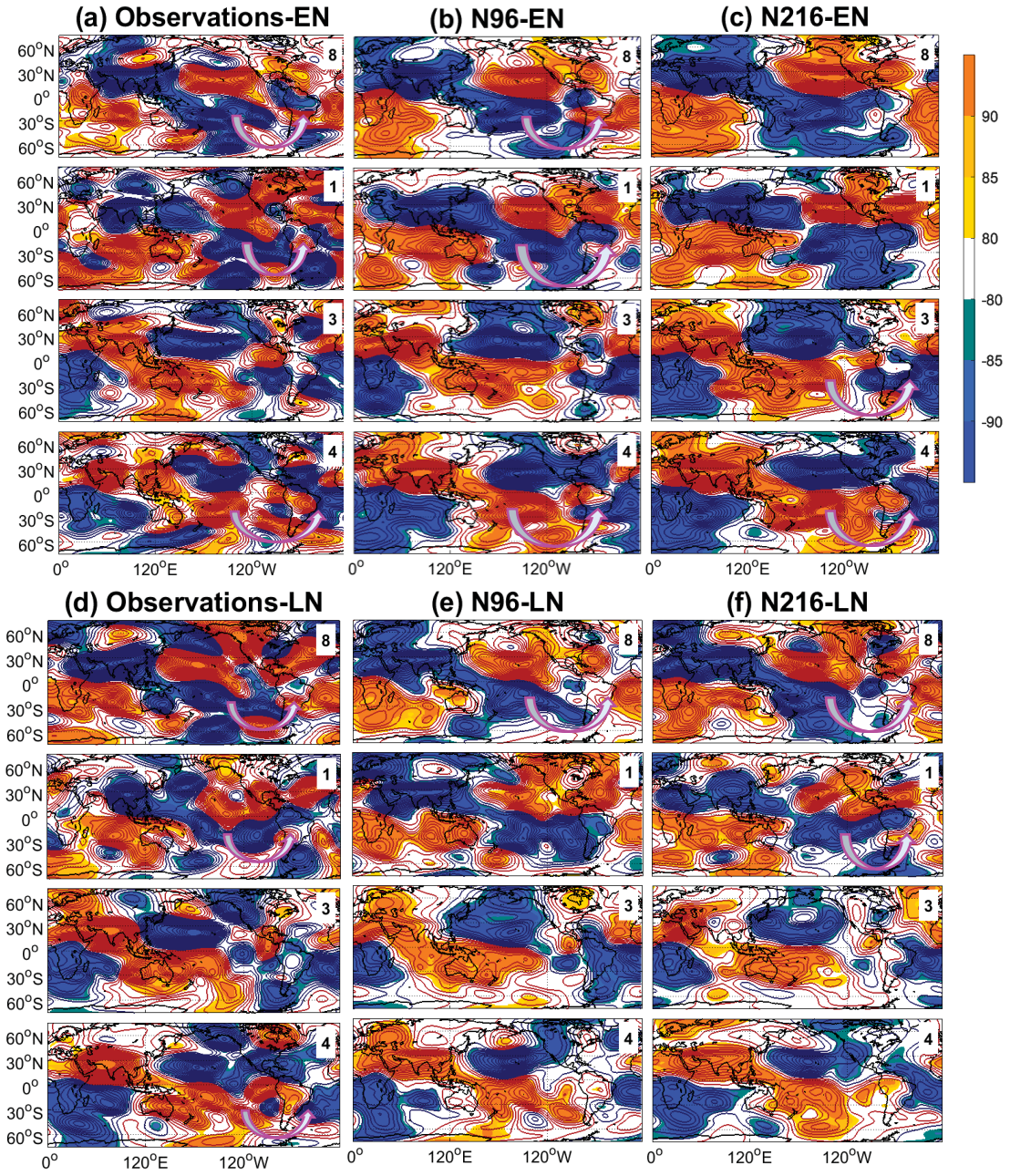

Figure 10: Composite anomalies of the 200 hPa streamfunction in MJO phases 8, 1, 3, 4 in (a) observations-EN, (b) N96-EN, (c) N216-N216, (d) observations-LN, (e) N96-LN, (f) N216-LN. Contour interval is $6 \times 10^5 m^2 s^{-1}$. Zero line is omitted. The color bar indicates confidence levels of streamfunction anomalies, with signs indicating positive or negative anomalies.

The MJO convection increases over the central-eastern SP in phases 6-1 (Fig. 3 and Fig. 8, some phases not shown), and this anomalous convection is enhanced during both EN and LN events, strengthening the extratropical teleconnection that produces more rainfall in CESA, especially in its southern part (Grimm 2019, Fernandes and Grimm 2021). This is favored by stronger low-level convergence in this region and also strong upper-level easterlies (Figs. 5 and 10, some phases not shown).

These features are stronger in N96-EN than N96 (Fig. 3b) and weaken too early in N216-EN (phases 8-1, Fig. 8e). Differences in the conditions over the source region between N96-EN and N216-EN may be due to differences in DJF Pacific air temperature anomalies (Fig. S2). Although the warm air temperatures anomalies have similar magnitudes over the central-east equatorial Pacific in both resolutions, the cold anomalies over the central-east subtropical South Pacific are stronger in N96-EN than N216-EN. We hypothesize that the increase in the subtropical temperature latitudinal gradient in N96-EN (Fig. S2) may favor the establishment of the teleconnection wavetrain to SA (Grimm and Natori, 2006).

In LN, the MJO anomalous convection is also shifted to the subtropical South Pacific (Moon et al. 2011; Fernandes and Grimm 2021) in phases 7-8 in MetUM-GOML3 and observations (Fig. 8b, d, f), coherent with colder equatorial SST and enhanced subsidence east of 180°. This subtropical convection during LN is shifted a little westward with respect to that associated with EN (Fig. 8a, b).

The above described features are best reproduced in N96-EN and N96-LN, as well as in N216-LN. The model weakens the subtropical convective anomalies during EN and displaces them to the east with respect to the observed ones, especially in N216-EN (Fig. 8, phases 8 and 1).

The extratropical teleconnections from the source region towards SA are visible in N96-EN, N96-LN and N216-LN (especially in phase 8, indicated by curved arrows, Fig. 10b, e, f), in which they are best represented, due to stronger forcing in the source region, described above, to excite the wavetrain. Notable component of this teleconnection patterns is the upper-level anomalous circulation dipole over subtropical and extratropical SA. The extratropical observed teleconnection establishes earlier in LN (phase 8, Fig. 10d) than EN (phase 1, Fig. 10a) (Fernandes and Grimm 2021). In observations-EN, the convection over the source region is stronger in phase 1 than in phase 8 (Fig. 8a), and the teleconnection wavetrain peaks in phase 1 (Fig. 10a). By contrast, the model teleconnection pattern is already fully established in phase 8 in both N96-EN (Fig. 10b) and N216-LN (Fig. 10f). In N96-EN, the convection over the source region is stronger in phase 8 than in phase 1, and the extratropical teleconnection establishes in phase 8.

In Section 4.1, three main factors are presented for the shift of the teleconnection pattern from phase 1 in observations to phase 8 in GOML3. Adding ENSO did not change this shift, at least concerning the enhanced convection in Southern CESA, in the SACZ.

The anomalous barotropic anticyclonic circulation near the southern tip of SA in phases 8-1 is part of the teleconnection wavetrain (Figs. 9a, d, 10a, d). It is shifted west in the model at upper-levels in phase 8 when the extratropical teleconnection is fully established (Figs. 5b, c, 10b, e, f). The anomalous anticyclonic circulation weakens in phase 1 (Figs. 5b, c and 10b, e) due to the decay of the teleconnection pattern. However, it is still visible in N216-LN at both levels (Figs. 9f, 10f). The upper-level cyclonic anomaly associated with enhanced rainfall in the SACZ is stronger in phase 8 than phase 1 in simulations (Fig. 10b, e, f). This feature is shifted east in N96-LN and N216-LN with respect to N96-EN in phase 8. Also, the precipitation anomalies in this phase are further east in N96-LN and N216-LN than N96-EN (next section).

As the enhanced (suppressed) convection is stronger and further east in EN (LN) than LN (EN) over the source region in phases 8-1 (3-4), the teleconnection pattern and its impacts on SA are shifted east in EN (LN) with respect to LN (EN) in phase 1 (phase 4) (Fig. 10a, d) (Fernandes and Grimm 2021). This shift also happens in the model, especially in phases 4 and 1 (cf Figs. 10b, c and Figs. 10e, f).

The subsidence over the central Pacific produced by the Walker circulation during LN favors equatorial MJO suppressed convection east of 180° (phase 3, Fig. 11d). The suppressed convection starts to shift southeastwards, entering into the favorable region to excite the teleconnection pattern to SA in phase 4 (Grimm 2019), which produces positive (negative) OLR anomalies in CESA (SESA) (Section 4.1). In the model, the equatorial suppressed convection extends east of 180° only in EN (Fig. 11b-c), because the MC barrier effect in MetUM-GOML3 magnifies in LN (not shown). N96-EN (phase 4) and N216-EN (phases 3-4) show maximized suppressed convection (and low-level divergence) over the central-eastern subtropical SP (Fig. 8c, e), able to trigger stronger extratropical teleconnections (Fig. 10b, c) with respect to simulations without ENSO (Fig. 5b, c). The teleconnection pattern is shifted east in N216-EN with respect to N96-EN, as simulations in Section 4.1. However, the wavetrain in phases 3-4 in N216-EN is more accurately positioned than N96-EN and simulations without ENSO, as the anomalous circulation dipole is adjacent to the South American continent, coherent with observations-EN.

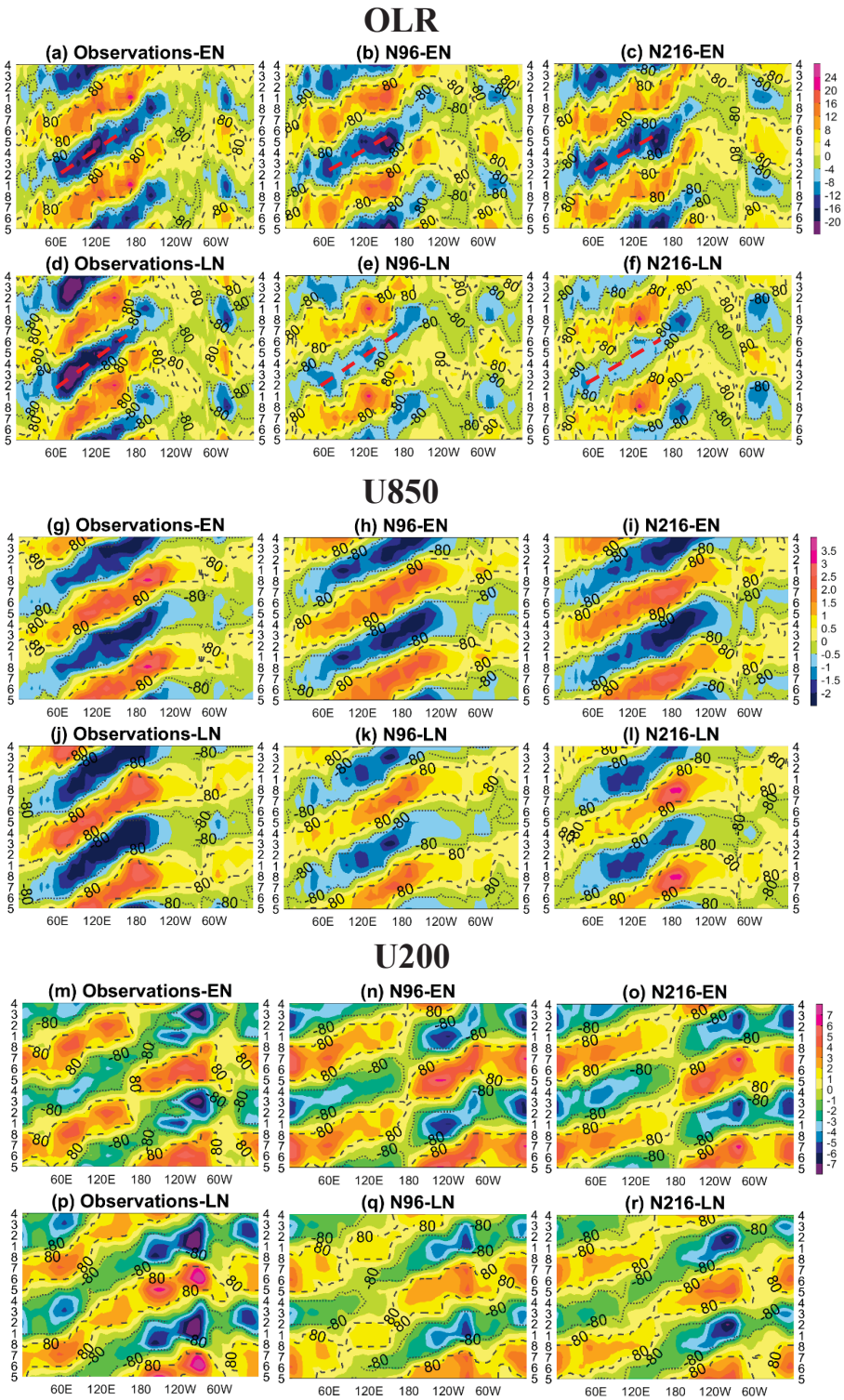

Figure 11: Time-longitude Hovmoller diagrams of 0°-15°S averaged OLR anomalies (Wm^{-2}), averaged zonal wind anomalies at 850 and 200 hPa (ms^{-1}), for each of the eight MJO phases during the austral summer in observations-EN (a, g, m), observations-LN (d, j, p), N96-EN (b, h, n), N96-LN (e-k-q), N216-EN (c-i-o), N216-LN (f-l-r). The dotted and dashed lines delimit the significant values with confidence levels > 80%.

The conditions over the source region to excite the wavetrain weaken in LN in the model (phases 3-4, Fig. 8d, f), and a weaker teleconnection pattern is visible in N96-LN and N216-LN (phase 4, Fig. 10e, f).

The eastward MJO propagation over the central-eastern Pacific slows (quickens) in EN (LN) due to warmer (colder) SSTs and stronger (weaker) convection during phases 6-7 (Zhang 2005), establishing the tropical teleconnection towards SA earlier in LN (phase 8, Figs. 9d and 11a) than EN (phase 1, Figs. 9a and 11d) (Fernandes and Grimm 2021). The U200 Hovmoller diagrams (Fig. 11) show that the eastward MJO propagation over colder SSTs in the equatorial central-eastern Pacific displays in LN stronger upper-level zonal winds, and gentler slopes than in EN (Fig. 11m-p) (Fernandes and Grimm 2021). The model reproduces the peak of the tropical teleconnection earlier in LN (phase 8) than EN (phase 1) (Figs. 9b, c, e, f). By contrast, EN (Fig. 11n-q) and LN (Fig. 11o-r) in MetUM-GOML3 show similar magnitude and propagation of the upper-level zonal winds.

Dry anomalies in phases 4-6 over the equatorial northeast SA last longer in N216-EN than N216-LN (phases 4-7), establishing the dipole over SA with opposite sign later in EN (phase 8) than LN (phase 7) (not shown). The anomalies are associated with changes in the simulated Walker circulation during EN in phases 6-7 by enhancing subsidence over northeastern SA, as discussed previously, extending the dryness in northern CESA (Fernandes and Grimm 2021). The persistent simulated dipole from phases 4-7 in EN is noticeable in the precipitation anomalies (next section).

5.2. Precipitation anomalies over SA associated with MJO in EN and LN

Figures 12 and 13 show the simulated precipitation anomalies over SA in each MJO phase in EN and LN states, respectively. A transition from negative to positive (positive to negative) precipitation anomalies over CESA (SESA) starts in phase 7, reaching the strongest positive precipitation anomalies in phase 1 (Fig. 7 of Grimm 2019). The model follows approximately this evolution (Figs. 12b, c), consistent with observations-EN (Fig. 12a). The persistent negative precipitation anomalies over northern CESA and NE Brazil in EN in phases 6-7 are related to the simulated enhanced convection in the central equatorial Pacific and increased subsidence over northeastern SA, as the combined effect of EN and MJO.

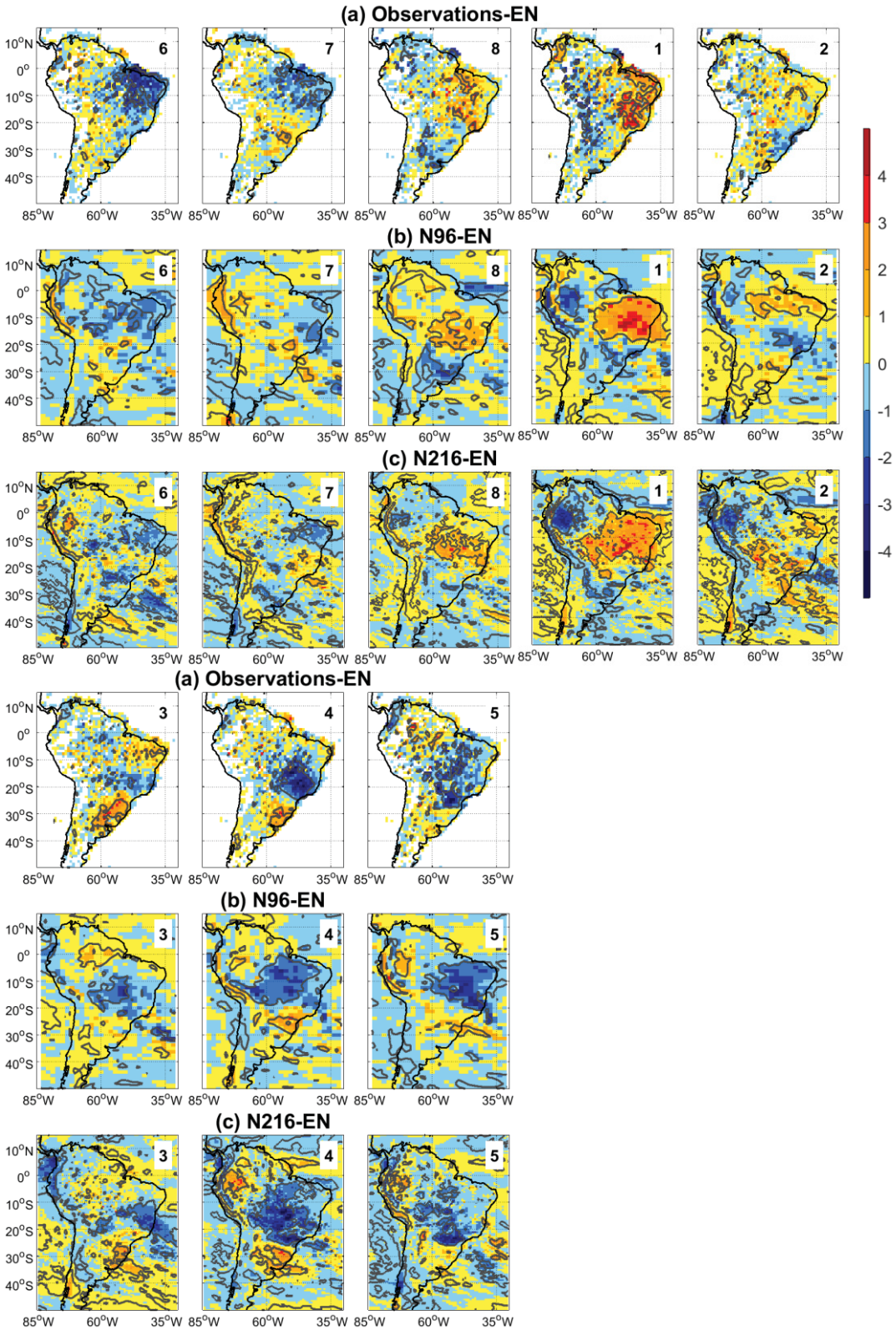

Figure 12: Composite anomalies of daily precipitation rate (color bar, $mm\ day^{-1}$), in each phase of the MJO, in (a) observations-EN, (b) N96-EN, (c) N216-EN. Gray lines have anomalies with confidence levels better than 85%.

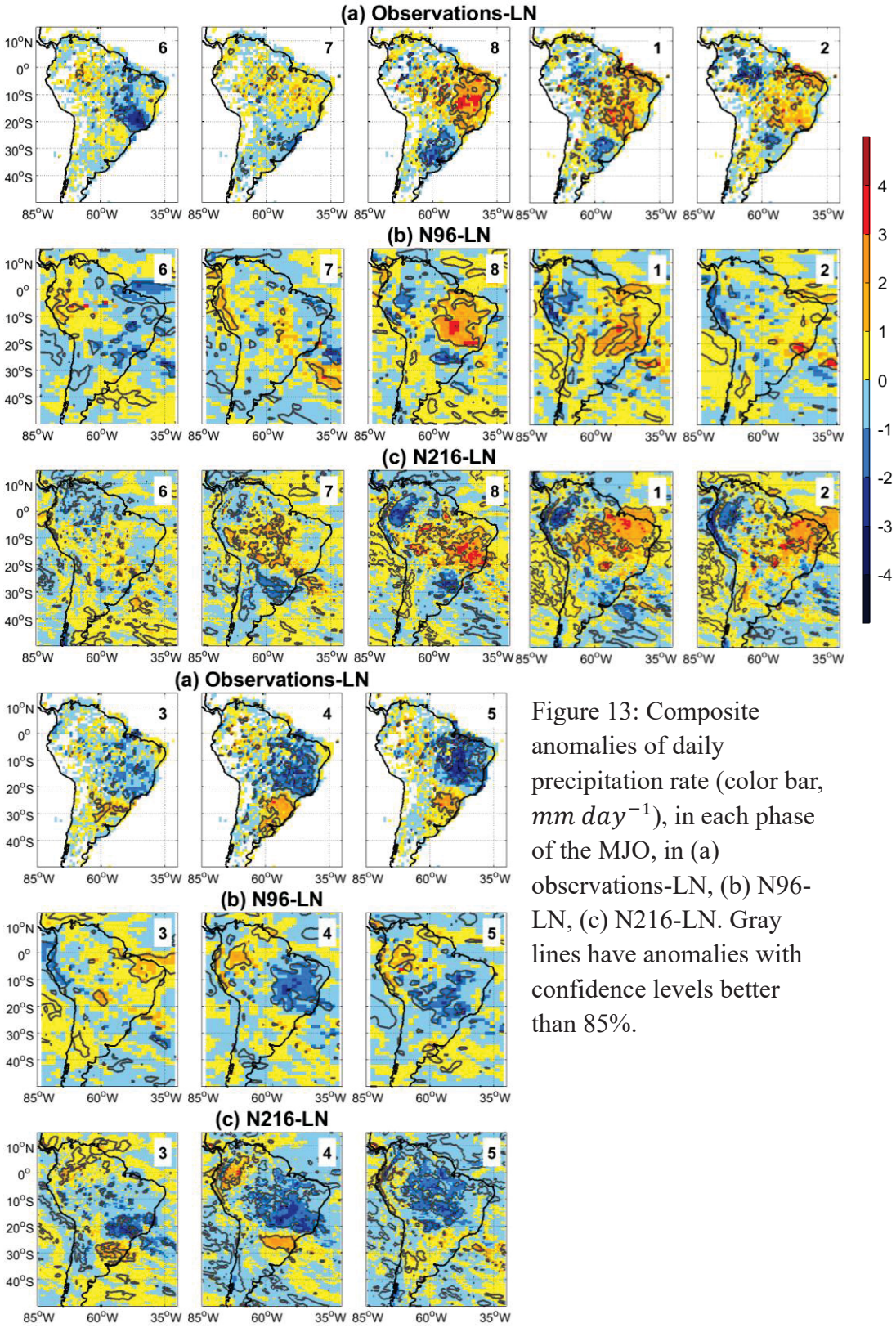

Figure 13: Composite anomalies of daily precipitation rate (color bar, $mm\ day^{-1}$), in each phase of the MJO, in (a) observations-LN, (b) N96-LN, (c) N216-LN. Gray lines have anomalies with confidence levels better than 85%.

Figure 13: Composite anomalies of daily precipitation rate (color bar, $mm\ day^{-1}$), in each phase of the MJO, in (a) observations-LN, (b) N96-LN, (c) N216-LN. Gray lines have anomalies with confidence levels better than 85%.

During LN, the evolution is a little advanced in relation to EN, as the transition that in EN starts in phase 7, in LN is almost completed in this phase, and the maximum precipitation anomalies in CESA happens in phase 8 (Fig. 13a). The model reproduces this difference, and also reproduces the stronger positive anomalies over NE Brazil in phase 2 during LN. Therefore, the model adequately represents the different evolutions of the precipitation dipole in EN and LN.

MJO circulation anomalies greatly differ over the continent between N96-EN and N216-EN in phase 8 (Fig. 10b, c). The strong anomalous extratropical anticyclone-subtropical cyclone pair over SA, linked to the extratropical teleconnection, appears well defined only in N96-EN. Hence, it is in this resolution that it favors significant positive SACZ precipitation anomalies (in southern CESA) (phase 8, Fig. 12b), while in phase 1 and in N216-EN the precipitation anomalies are shifted to northern CESA (Fig. 12b, c). Both resolutions reproduce the enhanced positive precipitation anomalies in tropical CESA and NE Brazil during phase 1 in EN (Fig. 12b, c), supported by strong westerly wind anomalies at lower levels (Fig. 8c, e), associated with the fully established tropical teleconnection (Fig. 9b, c), and coherent with observations-EN (Figs. 8a, 9a, 12a).

N96-LN and N216-LN simulate the most prominent anomalous precipitation dipole in phase 8 (Fig. 13b, c), consistent with observations-LN (Fig. 13a). N216-LN reproduces the strongest anomalous extratropical anticyclone-subtropical cyclone pair over SA in phase 8 (Fig. 10f). The equatorial waves strengthen positive precipitation anomalies from tropical CESA to NE Brazil. The extratropical Rossby wavetrain intensifies the subtropical precipitation anomalies and its circulation dipole over SA favors low-level moisture flux from the Amazon, increasing SACZ precipitation.

The similar effect of N96-EN and N96-LN / N216-LN on the most significant MJO precipitation anomalies in the SACZ through extratropical teleconnections happens in phase 8 (Figs. 12b, 13c), as the wavetrain decays in phase 1 (Fig. 10b, e, f). In observations, the nonlinear ENSO effect is stronger in phase 1 than phase 8 (Figs. 12a, 13a).

Increased horizontal resolution improves simulated precipitation anomalies in LN, bringing the model closer to observations-LN in phase 8. For instance, significant positive precipitation anomalies extend over the eastern Amazon and NE Brazil in N216-LN in phases 8-2 (Fig. 13c), consistent with enhanced convection over northeastern SA during LN,

discussed in Section 5.1. Also, significant negative precipitation anomalies appear in SESA in N216-LN in phases 7-1, enhanced by LN-driven subsidence added to the MJO effect (Grimm 2004; 2019).

A transition from positive to negative (negative to positive) precipitation anomalies over CESA (SESA) starts in phase 3 (Fig. 7 of Grimm 2019). The anomalous precipitation dipole in phases 3-4 in N216-EN (Fig. 12c) is coherent with observations-EN (Fig. 12a), shifted southeast with respect to N96-EN, as a response to the improved extratropical teleconnection position (Fig. 10a, c). In EN, the positive precipitation anomalies in the southern part of SESA last from phases 3 to 7 in both resolutions, consistent with observations-EN and the EN effect on SESA added to the MJO effect (Grimm 2003; 2019). On the other hand, negative precipitation anomalies appear over SESA, in phases 3-6 in N96-LN (Fig. 13b), which does not agree with observations-LN (Fig. 13a).

Summary and Conclusions

This study has evaluated the simulated MJO, its impacts on SA and their modulation by ENSO in MetUM-GOML3 during austral summer. The main conclusions are summarized below.

Changes in the MJO activity

MetUM-GOML3 simulates well the distribution of MJO activity in RMM phase space. Phases 3 and 7 (1, 2, 4, 5) are more (less) frequent, as observed (Fig. 2a) (Fernandes and Grimm 2021; Grimm et al. 2021). MJO activity is not affected by increased horizontal resolution (Fig. 2b, c). The model reproduces increased (decreased) MJO activity (Fig. 2e, f, h, i) when the ENSO-related anomalies in the Walker circulation favor (oppose) individual effect of MJO phases, as observed (Fig. 2d, g) (Fernandes and Grimm 2021). In simulations without ENSO, MetUM-GOML3 overestimates the observed likelihood of MJO decay over the MC (Fig. 2a, c); the overestimation is reduced in EN years in simulations with ENSO (Fig. 2e, f). Hence, the EN state improves eastward MJO propagation and weakens the MC barrier effect, which is generally too strong in GCMs (Vitart and Molteni 2010; Kim et al. 2018).

The simulated MJO and its impacts on SA

MetUM-GOML3 simulates well the MJO convection (Fig. 3b, c) and its eastward propagation (Fig. 6b, c). However, for a given MJO phase, the convection is further east than observed, particularly when the MJO moves through the MC-WP, which suggests errors in the convection-circulation phase relationship. The dynamical wave feedback may quicken propagation. MetUM-GOML3 shows weaker equatorial Rossby waves over the IO, but the observed magnitude of the equatorial Kelvin waves (low-level westerlies and easterlies, respectively, in Fig. 3b, c) over the MC-WP.

The fully established tropical (Fig. 4) and extratropical teleconnections to SA (Fig. 5), the strongest convection (Fig. 3), and positive precipitation anomalies over CESA (Fig. 7) during phase 1 (Grimm 2019) happen earlier in MetUM-GOML3, in phase 8. MetUM-GOML3 simulates anomalous convection (and low-level convergence) over the source region to excite the teleconnection pattern in phases 7-8, but it weakens too early (phase 1). Therefore, the precipitation anomalies in phases 8-1 in GOML3 are similar to the observed anomalies in phases 1-2, as in the ECMWF and NCEP models (Grimm et al. 2021).

Besides the quicker weakening of the convection over the central-east subtropical SP, MetUM-GOML3 establishes the teleconnection wavetrain to SA faster than observed (Grimm et al. 2021), which also favors earlier extratropical teleconnections. In addition, the higher transition probabilities of MJO activity to the next phase in MetUM-GOML3 (Fig. 2b, c) further supports earlier establishment of extratropical teleconnections towards SA (Fig. 4b-c).

It is worth emphasizing that in phase 4 MetUM-GOML3 also simulates suppressed convection (and low-level divergence) over the central-east subtropical SP (Fig. 3b, c), which is able to trigger the teleconnection to SA opposite-signed with respect to phases 8-1 (Fig. 5b-c). The teleconnection pattern and its impacts on SA, suppressed (enhanced) convection and negative (positive) precipitation anomalies in the SACZ (SESA), are simulated during phase 4 in both resolutions, appearing earlier in phase 3 in N96.

The effect of horizontal resolution

Increasing resolution enhances the MJO convection (Fig. 6), the low-level anomalous circulation dipole over SA (phases 8, 4, Fig. 4c), and the low-level cyclonic (anticyclonic) anomaly over subtropical SA in phase 8 (phase 4) (Fig. 3c), which brings moisture flux from

the Amazon into SACZ (SESA). Hence, the precipitation dipole extends to wider continental areas, with highest precipitation anomalies over SACZ in phases 8 and 4 (Fig. 7c).

Resolution strengthens the SA westerly jet over subtropical SA and its southern tip in N216 in phases 8, 1, 3, 4 (Fig. S1). Consequently, the upper-level extratropical teleconnections and their impacts over SA are slightly shifted east in N216 with respect to N96 (Figs. 5c, d, f, 7b, c). Remarkably, N216 improves the representation of the MJO impacts on SESA associated with the formation of MCSs over SA. The results support the hypothesis of Monerie et al. (2020) for increased austral summer (DJF) rainfall at higher resolution.

The ENSO-driven modulation of the MJO and its impacts on SA

Simulations with ENSO show that EN and LN background states influence the MJO phase distribution, eastward propagation, the position and intensity of the convection, teleconnections, and impacts on SA rainfall. Not all observed ENSO effects (Fernandes and Grimm 2021) are well simulated by the model and some of them are not reproduced. Notwithstanding, the agreement between MetUM-GOML3 and observations on many aspects validates the physical mechanisms proposed for ENSO modulation of the MJO impacts on observations, particularly as the MetUM-GOML3 simulations provide a larger sample of ENSO events than that from the observed records in Fernandes and Grimm (2021).

The MJO-related anomalies generally strengthen (weaken) in EN (LN) (Figs. 8, 9, 10) with respect to simulations without ENSO (Figs. 3, 4, 5), improving (worsening) the depiction of the equatorial waves. Hence, MJO eastward propagation is more (less) robust (Fig. 11) in EN (LN), coherent with the smaller (larger) MJO decay over the MC (Fig. 2). We hypothesize that the MetUM-GOML3 EN SST anomalies increase the moisture gradient near the MC and induce moisture advection and convergence by the enhanced low-level wind anomalies (Fig. 8c, e), favoring MJO eastward propagation through the MC (Wei and Ren 2019), an aspect which deserves further investigations.

Some MJO impacts on SA convection (and rainfall) during LN are well reproduced in MetUM-GOML3 at N216 (Figs. 8f, 11f), such as those on equatorial northeastern SA, affected by the ENSO modulation of the Walker circulation. The simulated subsidence (ascent) in EN (LN) reinforces (weakens) the dry anomalies over equatorial northeast SA in phases 5-6, extending them to phase 7 in N216-EN. On the other hand, the ascent

(subsidence) in N216-LN (EN) reinforces (weakens) the wet anomalies over this region later, in phases 8-2 (Figs. 12c, 13c).

The anomalous MJO convection over the central-east subtropical South Pacific in phases 6-8 is more prominent in N96-EN, N96-LN and N216-LN (Fig. 8c, d, f) than in simulations without ENSO (Fig. 6b, c), favoring conditions in the source region to trigger the extratropical teleconnections in phases 8-1. The convection and low-level convergence peaks earlier in N96-LN and N216-LN (phases 7-8) than N96-EN (phases 8-1), coherent with observations. In N216-LN, improvements result from increased horizontal resolution, as in simulations without ENSO. Both tropical and extratropical teleconnections are fully established in phase 8 (Figs. 9f and 10f), leading to the strongest anomalous precipitation dipole over SA (Fig. 13c), coherent with observations-LN (Figs. 9d, 13a) (Fernandes and Grimm 2021).

In phases 3-4 in EN, MetUM-GOML3 also shows maximum suppressed convection and low-level divergence over the source region (Fig. 8c, e), which triggers improved extratropical teleconnections to SA (Fig. 8c, e), with respect to simulations without ENSO (Figs. 5b, c and 7b, c). When MetUM-GOML3 correctly simulates MJO teleconnections, the magnitude and spatial distribution of the precipitation anomalies over SA improve (Figs. 12 and 13). Furthermore, we know the MJO itself improves under the MetUM-GOML3 EN background state. Hence, both the EN OLR basic state and the improved MJO enhance the simulated extratropical teleconnection towards SA.

The model delays the establishment of the tropical teleconnection towards SA in EN (phase 1) with respect to LN (phase 8), enhancing the precipitation anomalies over tropical CESA during the expected MJO phase. The simulated extratropical teleconnection pattern and its impacts on SA are shifted east in EN (LN) with respect to LN (EN) in phase 1 (phase 4) (Figs. 10b, c and Figs. 10e, f) as observed. (Fig. 10 a, d). MetUM-GOML3 reproduces the ENSO influence on both the basic state and the MJO convective anomalies, which modulate the MJO teleconnections and their impacts on SA. On the other hand, some issues found in simulations without ENSO persist in those with ENSO. For instance, the simulated teleconnection pattern is fully established earlier than observed, in phase 8. Hence, MetUM-GOML3 simulates the nonlinear ENSO effect on MJO anomalies over the SACZ earlier than observed, in phase 8 rather than phase 1.

MetUM-GOML3 shows valuable ability to simulate the MJO teleconnections in phases 8 and 4 and their opposite impacts on SA. In addition, as the MJO and its teleconnections improve during EN, other CGCMs may reproduce these features, and S2S predictions to SA may be better forecast when EN and MJO peak in DJF, though the MJO impacts in phase 1 remain challenging.

References

Ahn, M. S. et al. (2017) 'MJO simulation in CMIP5 climate models: MJO skill metrics and process-oriented diagnosis', Climate Dynamics, 49(11–12), pp. 4023–4045. doi: 10.1007/s00382-017-3558-4.

Ahn, M. S. et al. (2020) 'MJO propagation across the Maritime Continent: Are CMIP6 models better than CMIP5 models?', Geophysical Research Letters, 47, e2020GL087250. https://doi.org/10.1029/2020GL087250.

Arcodia, M. C. et al. (2020) 'How MJO Teleconnections and ENSO Interference Impacts U.S. Precipitation', Journal of Climate, 33, pp. 4621–4640.

Alvarez, M. S. et al. (2015) 'Influence of the Madden Julian Oscillation on precipitation and surface air temperature in South America', Climate Dynamics, 46(1–2), pp. 245–262. doi: 10.1007/s00382-015-2581-6.

Bush, S. J. et al. (2015) 'The effect of increased convection entrainment on Asian monsoon biases in the MetUM general circulation model.' Quarterly Journal of the Royal Meteorological Society, 141, pp. 311-326. doi: 10.1002/qj.2371.

Carvalho, L. M. V., Jones, C. and Liebmann, B. (2004) 'The South Atlantic convergence zone: Intensity, form, persistence, and relationships with intraseasonal to interannual activity and extreme rainfall', Journal of Climate, 17(1), pp. 88–108. doi: 10.1175/1520-0442(2004)017<0088:TSACZI>2.0.CO;2.

Chen, G. and Wang, B. (2018) 'Effects of Enhanced Front Walker Cell on the Eastward Propagation of the MJO', Journal of Climate, 31, pp. 7719-7738.

Coelho, C. A. S. et al. (2020) 'Evaluation of climate simulations produced with the Brazilian global atmospheric model version 1.2', Climate Dynamics. doi: 10.1007/s00382-020-05508-8.

Craig, A., Valcke, S., Coquart L. (2017) 'Development and performance of a new version of the OASIS coupler, OASIS3-MCT_3.0', Geoscientific Model Development, 10, pp. 3297-3308. https://doi.org/10.5194/gmd-10-3297-2017.

Cunningham, C. A. C. and Cavalcanti, I. F. de A. (2006) 'Intraseasonal modes of variability affecting the South Atlantic Convergence Zone', International Journal of Climatology, 26(9), pp. 1165–1180. doi: 10.1002/joc.1309.

Dawson, A. (2016) 'Windspharm: A High-Level Library for Global Wind Field Computations Using Spherical Harmonics', Journal of Open Research Software, 4. doi: 10.5334/jors.129.

Dee, D. P. et al. (2011) 'The ERA-Interim reanalysis: Configuration and performance of the data assimilation system', Quarterly Journal of the Royal Meteorological Society, 137(656), pp. 553–597. doi: 10.1002/qj.828.

Delworth, T. L. et al. (2012) 'Simulated climate and climate change in the GFDL CM2.5 high-resolution coupled climate model', Journal of Climate, 25(8), pp. 2755–2781. doi: 10.1175/JCLI-D-11-00316.1.

DeMott, C. A., Klingaman, N. P. and Woolnough, S. J. (2015) 'Reviews of Geophysics Atmosphere-ocean coupled processes in the Madden-Julian oscillation'. doi: 10.1002/2014RG000478.

Duchon, C. E. (1979) 'Lanczos Filtering in One and Two Dimensions.', Journal of applied meteorology, pp. 1016–1022. doi: 10.1175/1520-0450(1979)018<1016:LFIOAT>2.0.CO;2.

Fernandes, L. G., Grimm A. M. (2021) 'Global ENSO modulation of MJO and its impacts on South America', submitted in Climate Dynamics.

Ghelani, R. P. S. et al. (2017) 'Joint Modulation of Intraseasonal Rainfall in Tropical Australia by the Madden-Julian Oscillation and El Niño-Southern Oscillation', Geophysical Research Letters, 44(20), pp. 10,754-10,761. doi: 10.1002/2017GL075452.

Giddings et al. (2020) 'The effect of seasonally and spatially varying chlorophyll on Bay of Bengal surface ocean properties and the South Asian monsoon', Weather and Climate Dynamics, 1, pp. 635-655. doi: 10.5194/wcd-1-635-2020.

Grimm, A. M. (2003) 'The El Niño impact on the summer monsoon in Brazil: Regional processes versus remote influences', Journal of Climate, 16(2), pp. 263–280. doi: 10.1175/1520-0442(2003)016<0263:TENIOT>2.0.CO;2.

Grimm, A. M. (2004) 'How do La Niña events disturb the summer monsoon system in Brazil?', Climate Dynamics, 22(2–3), pp. 123–138. doi: 10.1007/s00382-003-0368-7.

Grimm, A. M. (2019) 'Madden–Julian Oscillation impacts on South American summer monsoon season: precipitation anomalies, extreme events, teleconnections, and role in the MJO cycle', Climate Dynamics, 53(1–2), pp. 907–932. doi: 10.1007/s00382-019-04622-6.

Grimm, A. M., Hakoyama, L. R. and Scheibe, L. A. (2021) 'Active and break phases of the South American summer monsoon: MJO influence and subseasonal prediction', Climate Dynamics, (0123456789). doi: 10.1007/s00382-021-05658-3.

Grimm, A. M., Pal, J. S. and Giorgi, F. (2007) 'Connection between spring conditions and peak summer monsoon rainfall in South America: Role of soil moisture, surface temperature, and topography in eastern Brazil', Journal of Climate, 20(24), pp. 5929–5945. doi: 10.1175/2007JCLI1684.1.

Grimm, A. M. and Natori, A. A. (2006) 'Climate change and interannual variability of precipitation in South America', Geophysical Research Letters, 33, pp. 1–5. doi: 10.1029/2006GL026821.

Grimm, A. M. and Silva Dias, P. L. (1995) 'Analysis of tropical-extratropical interactions with influence functions of a barotropic model', Journal of Atmospheric Sciences, pp. 3538–3555. doi: 10.1175/1520-0469(1995)052<3538:AOTIWI>2.0.CO;2.

Henderson, S. A., Maloney, E. D. and Son, S. W. (2017) 'Madden-Julian oscillation Pacific teleconnections: The impact of the basic state and MJO representation in general circulation models', Journal of Climate, 30(12), pp. 4567–4587. doi: 10.1175/JCLI-D-16-0789.1.

Henderson, S. A. and Maloney, E. D. and Son. (2018) 'The Impact of the Madden-Julian Oscillation on High-Latitude Winter Blocking during El Niño-Southern Oscillation Events', Journal of Climate, 31, pp. 5293–5318.

Hendon, H. H., Zhang, C. and Glick, J. D. (1999) 'Interannual variation of the Madden-Julian oscillation during austral summer', Journal of Climate, 12(8 PART 2), pp. 2538–2550. doi: 10.1175/1520-0442(1999)012<2538:ivotmj>2.0.co;2.

Hirata, F. E. and Grimm, A. M. (2015) 'The role of synoptic and intraseasonal anomalies in the life cycle of summer rainfall extremes over South America', Climate Dynamics, 46(9–10), pp. 3041–3055. doi: 10.1007/s00382-015-2751-6.

Hirons, L. C., Klingaman, N. P. and Woolnough, S. J. (2015) 'MetUM-GOML1: A near-globally coupled atmosphere-ocean-mixed-layer model', Geoscientific Model Development, 8(2), pp. 363–379. doi: 10.5194/gmd-8-363-2015.

Jiang, X. et al. (2015) 'Vertical structure and physical processes of the Madden-Julian oscillation: Exploring key model physics in climate simulations', Journal of Geophysical Research, 120, pp. 4718–4748. doi: 10.1002/2014JD022375.

Jung, T. et al. (2012) 'High-resolution global climate simulations with the ECMWF model in project athena: Experimental design, model climate, and seasonal forecast skill', Journal of Climate, 25(9), pp. 3155–3172. doi: 10.1175/JCLI-D-11-00265.1.

Kessler, W. S. (2001) 'EOF Representations of the Madden-Julian Oscillation and Its Connection with ENSO', Journal of Climate, 14, pp. 3055-3061.

Kim, D., Kug, J.-S. and Sobel, A. H. (2011) ‘A systematic relationship between intraseasonal variability and mean state bias in AGCM simulations’, Journal of Climate, 24(21), pp. 5506–5520. doi: 10.1175/2011JCLI4177.1.

Kim, D. et al. (2014) ‘Propagating versus nonpropagating Madden–Julian oscillation events’, Journal of Climate, 27, pp. 111–125. doi: 10.1175/JCLI-D-13-00084.1.

Kim, D., Kim, H. and Lee, M. I. (2017) ‘Why does the MJO detour the Maritime Continent during austral summer?’, Geophysical Research Letters, 44(5), pp. 2579–2587. doi: 10.1002/2017GL072643.

Kim, H., Vitart, F. and Waliser, D. E. (2018) ‘Prediction of the Madden-Julian oscillation: A review’, Journal of Climate, 31(23), pp. 9425–9443. doi: 10.1175/JCLI-D-18-0210.1.

Klingaman, N. P. et al. (2015) ‘Vertical structure and physical processes of the Madden-Julian oscillation: Linking hindcast fidelity to simulated diabatic heating and moistening’, Journal of Geophysical Research, 120(10), pp. 4690–4717. doi: 10.1002/2014JD022374.

Klingaman, N. P. et al. (2020) ‘Subseasonal Prediction Performance for Austral Summer South American Rainfall’, Weather and Forecasting, 36(1), pp. 147–169. doi: 10.1175/waf-d-19-0203.1.

Klingaman, N. P. and Demott, C. A. (2020) ‘Mean State Biases and Interannual Variability Affect Perceived Sensitivities of the Madden-Julian Oscillation to Air-Sea Coupling’, Journal of Advances in Modeling Earth Systems, 12(2), pp. 1–22. doi: 10.1029/2019MS001799.

Klingaman, N P and Woolnough, S. J. (2014a) ‘The role of air – sea coupling in the simulation of the Madden – Julian oscillation in the Hadley Centre model †’, (October), pp. 2272–2286. doi: 10.1002/qj.2295.

Klingaman, N. P. and Woolnough, S. J. (2014b) ‘Using a case-study approach to improve the Madden-Julian oscillation in the Hadley Centre model’, Quarterly Journal of the Royal Meteorological Society, 140(685), pp. 2491–2505. doi: 10.1002/qj.2314.

Kodama, C. et al. (2015) ‘A 20-Year climatology of a NICAM AMIP-type simulation’, Journal of the Meteorological Society of Japan, 93(4), pp. 393–424. doi: 10.2151/jmsj.2015-024.

Large, W. G., McWilliams, J. C. and Doney, S. C. (1994) ‘Oceanic vertical mixing: A review and a model with a nonlocal boundary layer parameterization’, Reviews of Geophysics, 32(4), pp. 363–403. doi: 10.1029/94RG01872.

Lee, R. W. et al. (2019) ‘ENSO Modulation of MJO Teleconnections to the North Atlantic and Europe’, Geophysical Research Letters, 46(22), pp. 13535–13545. doi: 10.1029/2019GL084683.

Liebmann, B. and Allured, D. (2005) ‘Daily precipitation grids for South America’, Bulletin of the American Meteorological Society, 86(11), pp. 1567–1570. doi: 10.1175/BAMS-86-11-1567.

Liebmann B. and Smith C.A. (1996) ‘Description of a Complete (Interpolated) Outgoing Longwave Radiation Dataset’, Bulletin of the American Meteorological Society, 77, pp.1275-1277.

Liu, F. and Wang B. (2017) ‘Roles of the Moisture and Wave Feedbacks in Shaping the Madden-Julian Oscillation’, Journal of Climate, 30, pp. 10275-10291.

Liu, X. et al. (2017) ‘MJO prediction using the sub-seasonal to seasonal forecast model of Beijing Climate Center’, Climate Dynamics, 48(9–10), pp. 3283–3307. doi: 10.1007/s00382-016-3264-7. doi: https://doi.org/10.1175/JCLI-D-17-0003.1.

Matsuno, T. (1966) ‘Quasi-Geostrophic Motions in the Equatorial Area’, Journal of the Meteorological Society of Japan. Ser. II, 44(1), pp. 25–43. doi: 10.2151/jmsj1965.44.1_25.

Monerie, P.-A. et al. (2020) ‘Role of atmospheric horizontal resolution in simulating tropical and subtropical South American precipitation in HadGEM3-GC31’, Geoscientific Model Development Discussions, (June), pp. 1–44. doi: 10.5194/gmd-2020-125.

Moon, J. Y., Wang, B. and Ha, K. J. (2011) ‘ENSO regulation of MJO teleconnection’, Climate Dynamics, 37(5), pp. 1133–1149. doi: 10.1007/s00382-010-0902-3.

Peatman, S. C., Klingaman, N. P. (2018) ‘The Indian summer monsoon in MetUM-GOML2.0: effects of air-sea coupling and resolution’, Geoscientific Model Development, 11, pp. 4693-4709. https://doi.org/10.5194/gmd-11-4693-2018.

Rayner, N. A. et al. (2003) ‘Global analyses of sea surface temperature, sea ice, and night marine air temperature since the late nineteenth century’, Journal of Geophysical Research D: Atmospheres, 108(14). doi: 10.1029/2002jd002670.

Roundy, P. E. et al. (2010) ‘Modulation of the global atmospheric circulation by combined activity in the Madden-Julian oscillation and the El Niño-southern oscillation during boreal winter’, Journal of Climate, 23(15), pp. 4045–4059. doi: 10.1175/2010JCLI3446.1.

Sakaeda, N. and Roundy, P. E. (2016) ‘The development of upper-tropospheric geopotential height anomaly in the Western Hemisphere during MJO convective initiations’, Quarterly Journal of the Royal Meteorological Society, 142(695), pp. 942–956. doi: 10.1002/qj.2696.

Shaffrey, L. C. et al. (2009) ‘U.K. HiGEM: The new U.K. high-resolution global environment model - Model description and basic evaluation’, Journal of Climate, 22(8), pp. 1861–1896. doi: 10.1175/2008JCLI2508.1.

Slingo, J. M. et al. (1999) ‘On the predictability of the interannual behaviour of the Madden-Julian Oscillation and its relationship with El Nino’, Quarterly Journal of the Royal Meteorological Society, 125(554), pp. 583–609. doi: 10.1256/smsqj.55410.

Smith, D. M. and Murphy, J. M. (2007) ‘An objective ocean temperature and salinity analysis using covariances from a global climate model’, Journal of Geophysical Research, 12(C02022). https://doi.org/10.1029/2005JC003172.

Solman, S. A. and Blázquez, J. (2019) ‘Multiscale precipitation variability over South America: Analysis of the added value of CORDEX RCM simulations’, Climate Dynamics, 53(3–4), pp. 1547–1565. doi: 10.1007/s00382-019-04689-1.

de Souza Custodio, M. de S., Rocha, R. P. da and Vidale, P. L. (2012) ‘Analysis of precipitation climatology simulated by high resolution coupled global models over the South America’, Hydrological Research Letters, 6(0), pp. 92–97. doi: 10.3178/hrl.6.92.

de Souza Custodio, M. et al. (2017) ‘Impact of increased horizontal resolution in coupled and atmosphere-only models of the HadGEM1 family upon the climate patterns of South America’, Climate Dynamics, 48(9–10), pp. 3341–3364. doi: 10.1007/s00382-016-3271-8.

Straub, K. H. (2013) ‘MJO Initiation in the Real-Time Multivariate MJO Index’, Journal of Climate, 26, pp. 1130-1151.

Tam, C. Y. and Lau, N. C. (2005) ‘Modulation of the Madden-Julian Oscillation by ENSO: Inferences from observations and GCM simulations’, Journal of the Meteorological Society of Japan, 83(5), pp. 727–743. doi: 10.2151/jmsj.83.727.

Tseng, K. C., Maloney, E. and Barnes, E. A. (2020) ‘The consistency of MJO teleconnection patterns on interannual time scales’, Journal of Climate, 33(9), pp. 3471–3486. doi: 10.1175/JCLI-D-19-0510.1.

Vitart, F. et al. (2017) ‘The subseasonal to seasonal (S2S) prediction project database’, Bulletin of the American Meteorological Society, 98(1), pp. 163–173. doi: 10.1175/BAMS-D-16-0017.1.

Vitart, F. and Molteni, F. (2010) ‘Simulation of the Madden-Julian oscillation and its teleconnections in the ECMWF forecast system’, Quarterly Journal of the Royal Meteorological Society, 136(649), pp. 842–855. doi: 10.1002/qj.623.

Vitart, F., A. W. Robertson, A. W and S2S Steering Group (2015) ‘Sub-seasonal to seasonal prediction: Linking weather and climate.’ Seamless Prediction of the Earth System: From Minutes to Months, G. Brunet, S. Jones, and P. M. Ruti, Eds., WMO-1156, World Meteorological Organization, 385–401. [Available online at http://library.wmo.int/pmb_ged/wmo_1156_en.pdf.]

Walters, D. et al. (2019) 'The Met Office Unified Model Global Atmosphere 7.0/7.1 and JULES Global Land 7.0 configurations', Geoscientific Model Development, 12(5), pp. 1909–1963. doi: 10.5194/gmd-12-1909-2019.

Wang, J. et al. (2020a) 'MJO teleconnections over the PNA region in climate models. Part I: Performance- And process-based skill metrics', Journal of Climate, 33(3), pp. 1051–1067. doi: 10.1175/JCLI-D-19-0253.1.

Wang, J. et al. (2020b) 'MJO Teleconnections over the PNA Region in Climate Models. Part II: Impacts of the MJO and Basic State', Journal of Climate, 33(12), pp. 5081–5101. doi: 10.1175/jcli-d-19-0865.1.

Wang, L., Li, T. and Nasuno, T. (2018) 'Impact of Rossby and Kelvin Wave Components on MJO Eastward Propagation', Journal of Climate, 31, pp. 6913–6931.

Wei Y, Ren H-L (2019) 'Modulation of ENSO on Fast and Slow MJO Modes during Boreal Winter', Journal of Climate, 32, pp. 7483-7506. https://doi.org/10.1175/JCLI-D-19-0013.1

Wheeler, M. C. and Hendon, H. H. (2004) 'An all-season real-time multivariate MJO index: Development of an index for monitoring and prediction', Monthly Weather Review, 132(8), pp. 1917–1932. doi: 10.1175/1520-0493(2004)132<1917:AARMMI>2.0.CO;2.

Wheeler, M. C. et al. (2009) 'Impacts of the Madden-Julian Oscillation on Australian Rainfall and Circulation', Journal of Climate, 22, pp. 1482–1498.

Wilks, D. S. (2006) 'Statistical Methods in the Atmospheric Sciences'. United States of America: Academic Press, 627 pp., 2006.

Woolnough, S. J., Slingo, J. M. and Hoskins, B. J. (2000) 'The relationship between convection and sea surface temperature on intraseasonal timescales', Journal of Climate, 13(12), pp. 2086–2104. doi: 10.1175/1520-0442(2000)013<2086:TRBCAS>2.0.CO;2.

Zhang, C. (2005) 'MADDEN-JULIAN OSCILLATION', (2004), pp. 1–36. doi: 10.1029/2004RG000158.1.INTRODUCTION.

Zhang, C. and Ling, J. (2017) 'Barrier effect of the Indo-Pacific Maritime Continent on the MJO: Perspectives from tracking MJO precipitation', Journal of Climate, 30(9), pp. 3439–3459. doi: 10.1175/JCLI-D-16-0614.1.

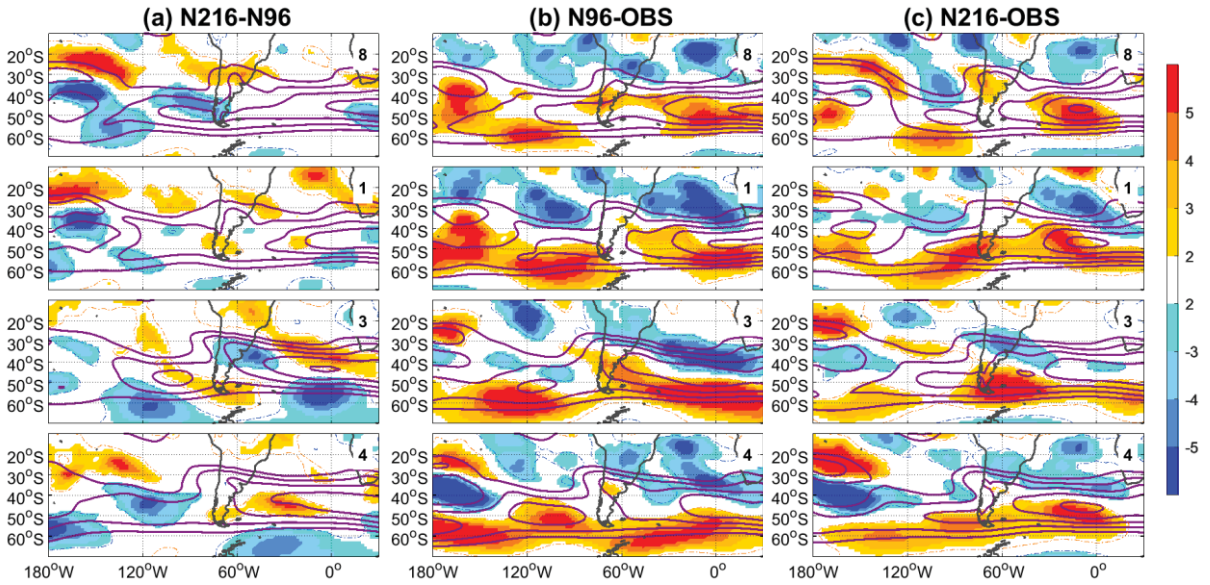

Figure S1: Zonal wind at 200 hPa (contour interval: 5 ms^{-1} starting from 20 ms^{-1}) in MJO phases 8, 1, 3, 4 in (a) observations, (b) N96, and (c) N216. Shading denotes (a) N216-N96, (b) N96-OBS, and (c) N216-OBS differences in the zonal wind at 200 hPa. Dashed lines areas indicate significant differences exceeding the 95% confidence level.

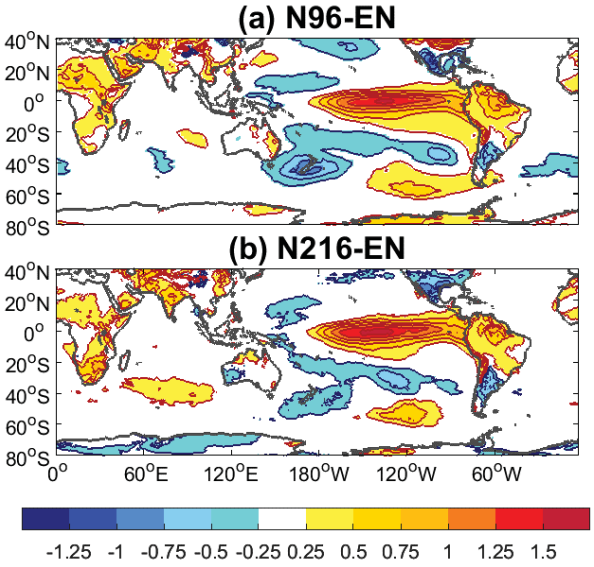

Figure S2: Monthly mean 1.5-meter temperature anomalies during the austral summer (DJF) in (a) N96-EN and (b) N216-EN.

6. Summary and Conclusions

The results shown in both manuscripts have confirmed the hypothesis mentioned on page 15 of this study. Although the global MJO activity does not show a great connection with ENSO in observations (Section 3.3 of Manuscript 1) and simulations (Section 3.2 of Manuscript 2), as pointed out by previous studies (e.g., HENDON et al., 1999; SLINGO et al., 1999; KESSLER, 2001), the background changes produced by different ENSO states influence several MJO aspects in MetUM-GOML3 and observations. Among them are the distribution of MJO phases, the eastward propagation, the position and intensity of convection, the teleconnections, and the impacts on SA. Not all observed ENSO effects (Fernandes and Grimm 2021) are well simulated by the model and some of them are not reproduced. Notwithstanding, the agreement between MetUM-GOML3 and observations on many aspects validates the physical mechanisms proposed for ENSO modulation of the MJO impacts on observations, particularly as the MetUM-GOML3 simulations provide a larger sample of ENSO events than that from the observed records.

We propose the following answers for the research questions (also from page 15) prompted by the hypothesis above.

(1) How does the ENSO-MJO combination affect the precipitation anomalies and their extremes on SA?

Answer: ENSO can modify the MJO-rainfall relationship in SA not only because it modifies the MJO characteristics regarding convective anomalies and their propagation, but also because it creates different basic states through which the perturbations propagate toward SA, affecting the physical mechanisms by which the MJO influences rainfall variability in SA. Changes in these impacts in opposite ENSO states with respect to the NT state affect both the intensity of precipitation anomalies and the frequency of extreme events, as well as their temporal distribution throughout the MJO cycle, and are not always opposite, indicating the existence of both linear and nonlinear effects of ENSO.

(2) What are the changes in the MJO teleconnection patterns and the atmospheric circulation related to the joint influence?

Answer: Observations show that the slower (faster) eastward propagation of the MJO signal over the equatorial central-eastern South Pacific is probably due to warmer (colder)

SSTs and enhancement (suppression) of convection in this region in EN (LN). It delays (anticipates) the MJO phase in which there is the inversion of the intraseasonal precipitation dipole over CESA in EN (LN), making the distribution of positive and negative precipitation anomalies in CESA less (more) symmetric in EN (LN) than NT. This effect is more noticeable in the second half of the MJO cycle (phases 6, 7, 8) since in this period there is the strongest difference between EN and LN equatorial anomalous convection in central-east Pacific, between 180°W-120°W. The decreased (increased) MJO phase velocity in EN (LN) leads to the peak of the tropics-tropics teleconnections between the central-eastern equatorial Pacific and SA in MJO_{LN}phase8, while it happens later in MJO_{EN}phase1. Besides, the different EN/LN OLR background states affect the enhanced MJO convection over the subtropical central-eastern South Pacific, favoring it in MJO_{LN}phases7+8 (Fig. 10, top panel) and a little further east, in MJO_{EN}phases8+1 (Fig. 10, bottom panel). These differences affect the evolution, strength, and propagation of the tropics-extratropics teleconnections to SA in ENSO years. They are stronger one phase later and are shifted east in MJO_{EN}phases8+1 with respect to MJO_{LN}phases8+1 (Fig. 10).

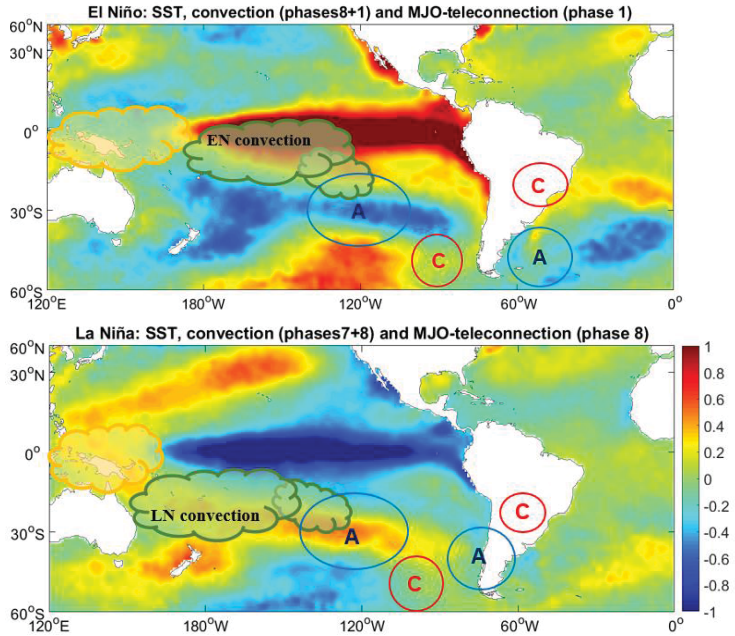

Figure 10: The schematic diagrams illustrating the typical patterns of MJO tropics-extratropics teleconnections to SA in MJO_{EN}phase1 (top panel) and MJO_{LN}phase8 (bottom panel). Blue and red thick contours display the MJO teleconnection at 200 hPa. Letter A (C) depicts the anticyclonic (cyclonic) circulation anomaly. The color bar shows the SST anomalies. The cloud shape in green represents convection associated with MJO (small convection) and ENSO (large convection), and the cloud shape orange denotes the MJO subsidence.

Therefore, the strongest impact over CESA is advanced by one phase in LN with respect to EN since both the tropics-tropics and the tropics-extratropics teleconnections that connect the MJO to SA are established one phase earlier in LN. Notwithstanding, the impact on subtropical CESA (and in the SACZ) rainfall and its extremes is still strong in MJO_{LN}phase1, being a little displaced westward in MJO_{LN}phases8+1 with respect to MJO_{EN}phases8+1.

Also, changes in the MJO impacts in EN and LN states with respect to NT ENSO state indicate nonlinear effects of ENSO on MJO anomalies over SA. Similar effects are on the extratropical teleconnection pattern, which causes the most prominent precipitation anomalies and extreme events over the SACZ (phases 8-1). EN and LN favor anomalous MJO convection over the source region, providing enhanced conditions to produce the teleconnection pattern in phases 8+1, whereas NT ENSO years do not. Furthermore, similar effects happen again in phases 4+5, when enhanced negative precipitation anomalies are over subtropical CESA, associated with the extratropical teleconnection pattern in phase 4 and suppressed convection over the source region in phases 3+4. Despite the characteristic teleconnection wave train in phase 4 is missing in composites for all years (1979-2009) (GRIMM, 2019), it is well defined in composites for each ENSO state (EN, LN, NT) through the same period.

Observations also show that MJO_{EN}phase4 and MJO_{LN}phase4 favor suppressed MJO convection in the central-eastern subtropical South Pacific, stronger and a little further to the east in MJO_{LN}phase4 than MJO_{EN}phase4. It shifts the tropics-extratropics teleconnections to SA eastward in MJO_{LN}phase4 with respect to MJO_{EN}phase4. This behavior is analogous to the teleconnection wave train displaced eastwards in MJO_{EN}phases8+1 with respect to MJO_{LN}phases8+1 due to enhanced convection over the central-eastern subtropical South Pacific stronger and more to the east in MJO_{EN}phases8+1 (Fig. 10, top panel) than MJO_{LN}phases7+8 (Fig. 10, bottom panel). Therefore, the ENSO seems to modulate the MJO teleconnections to SA in complex ways due to its widespread influence on both the basic state and the MJO convective anomalies.

(3) What are the effects of the ENSO-MJO combination reproduced in the MetUM-GOML3?

Answer: The anomalous MJO convection over the central-east subtropical South Pacific in phases 6-8 is more prominent in N96-EN, N96-LN and N216-LN than in simulations without ENSO, favoring conditions in the source region to trigger the extratropical teleconnections in phases 8-1. The convection and low-level convergence peaks earlier in N96-LN and N216-LN (phases 7-8) than N96-EN (phases 8-1), coherent with observations. In N216-LN, improvements result from increased horizontal resolution, as in simulations without ENSO. Both tropical and extratropical teleconnections are fully established in phase 8 in N216-LN, leading to the strongest anomalous precipitation dipole over SA, coherent with observations-LN (Fernandes and Grimm 2021).

In phases 3-4 in EN, MetUM-GOML3 also shows maximum suppressed convection and low-level divergence over the source region, which triggers improved extratropical teleconnections to SA, with respect to simulations without ENSO (Figs. 5b, c and 7b, c). When MetUM-GOML3 correctly simulates MJO teleconnections, the magnitude and spatial distribution of the precipitation anomalies over SA improve. Furthermore, we know the MJO itself improves under the MetUM-GOML3 EN background state. Hence, both the EN OLR basic state and the improved MJO enhance the simulated extratropical teleconnection towards SA.

MetUM-GOML3 shows valuable ability to simulate the MJO teleconnections in phases 8 and 4 and their opposite impacts on SA. Furthermore, MetUM-GOML3 reproduces the ENSO influence on both the basic state and the MJO convective anomalies, which modulate the MJO teleconnections and their impacts on SA. For instance, over northeast SA, considering simulations at N216, the MJO-related anomalous subsidence and dryness that occurs mainly in phases 5 and 6 are enhanced during EN and extended to phase 7, while anomalous wetness in phases 1 and 2 is reduced, thanks to the EN background anomalies of Walker circulation subsidence over that region (Fig. 11a, left panels). During the LN state, the opposite occurs (Fig. 11b, right panels).

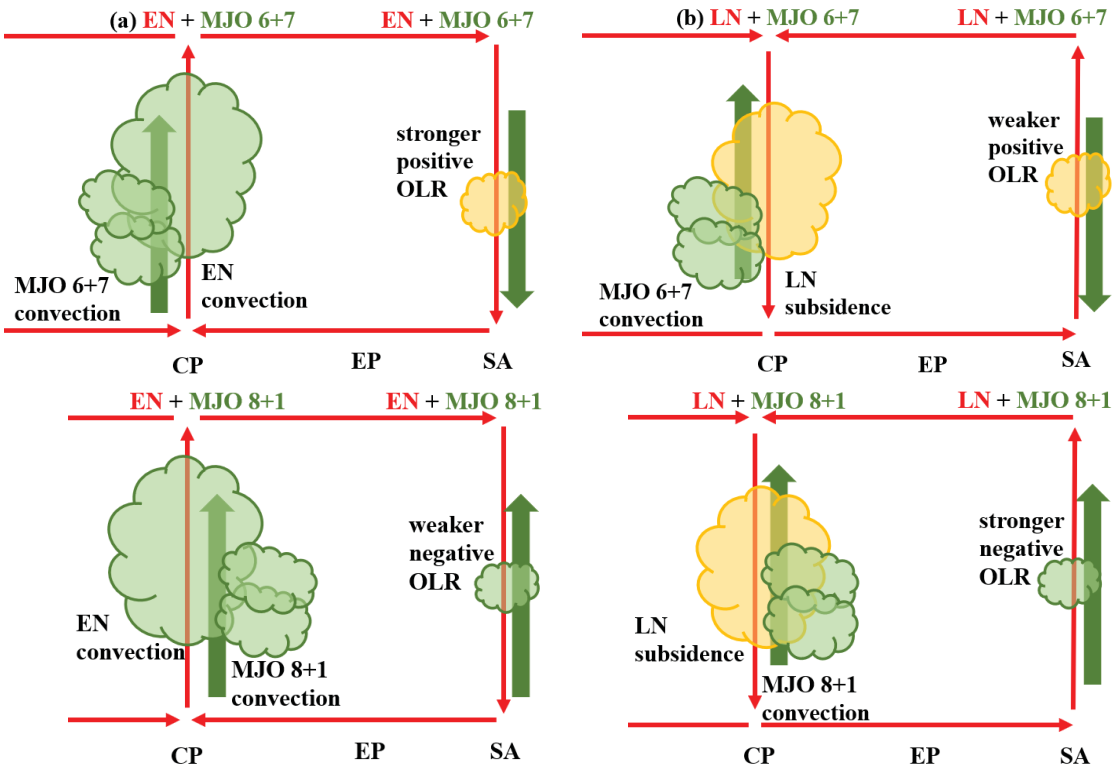

Figure 11: Scheme shows changes in the Walker circulation due to (a) EN and (b) LN, and how they affect the intraseasonal OLR anomalies at the equator, over Central Pacific (CP), Eastern Pacific (EP), and South America (SA) in MJO phases 6+7 (top) and 8+1 (bottom). Red arrows: Walker circulation in each ENSO phase. Green arrows: Vertical motion associated with MJO. The cloud shape in green represents convection associated with MJO and ENSO, and the cloud shape orange denotes the subsidence.

On the other hand, some issues found in simulations without ENSO persist in those with ENSO. For instance, the simulated extratropical teleconnection pattern is fully established earlier than observed, in phase 8. Hence, MetUM-GOML3 simulates the nonlinear ENSO effect on MJO anomalies over the SACZ earlier than observed, in phase 8 rather than phase 1.

The ENSO-driven changes in the MJO impacts on SA are more significant in the frequency of extreme events than in the precipitation anomalies in MetUM-GOML3 and observations. However, we have decided not to show the extreme events in Manuscript 2 to avoid extending the analyzes. It could be argued that extreme events are extensively and significantly much enhanced (or reduced) with respect to NT in regions where the effects of both ENSO and MJO contribute to enhance (or reduce) them. The strongest modulation of MJO impacts on extremes happens during the EN state, probably because it represents a stronger deviation from the climatology since the LN state represents an enhancement of climatological conditions over the Pacific.

The conclusions about the ENSO influence on the MJO impact on SA rainfall emphasize the importance of investigating the modulation of these MJO impacts by other natural climate variability oscillations, as the main interdecadal climate variability modes affecting the SA climate, the IPO, and the AMO (GRIMM and SABOIA, 2015; GRIMM et al., 2016). Further studies about the interaction between other natural climate variability modes occurring in other seasons and different phase combinations are essential for water resources management on SA. There are many water supply reservoirs in SA, and electric power generation strongly depends on hydroelectricity. The storage of water resources in SA must be planned according to the possible effects of the climate oscillations and their combinations, so that the effects of severe droughts or extreme rainfall events can be mitigated. The short period of available precipitation and hydrologic data usually shows extremes that may be overcome by extremes originated by the combined effect of natural climate variability modes. The water resources managers must be aware of how extreme the water emergencies can be.

The most recent example is the severe drought in Southern Brazil during the austral autumn of 2020, which was a superposition of the effects of negative IPO, positive AMO, and a central EN (GRIMM et al., 2020). The drought conditions have persisted during the austral spring of 2020 and the austral summer of 2020/21 due to the development and establishment of the LN 2020/21. For instance, the drought could be even more accentuated in some weeks of 2020/2021 summer if the MJO were strong and active during phases 8-1, which favor the reduced anomalous precipitation in southern Brazil.

In summary, results pointed here and by previous studies (KAYANO and CAPISTRANO, 2014; GRIMM and SABOIA, 2015 GRIMM et al., 2016; GRIMM et al., 2021) highlight indicate that the SA precipitation anomalies and their extremes are conditioned by the combined influence of different climate variability modes. Moreover, the IPO modulates the ENSO (CAI et al., 2020; LEE and MCPHADEN, 2010; AN and WANG, 2000) and their impacts on subtropical (FERNANDES and RODRIGUES, 2018) and extratropical (GARREAUD et al., 2020) SA rainfall. Therefore, despite the conclusions regarding the ENSO-MJO interaction, the interaction between distinct climate variability modes, acting on different time scales, and its impacts on SA climate is a very active research area (e.g., GRIMM et al. 2021), open to further future investigations.

References

ACEITUNO, P. On the Functioning of the Southern Oscillation in the South American Sector. Part I: Surface Climate. **Mon Weather Rev,** v. 116, p. 506-524, 1988.

AHN M-S. et al. MJO simulation in CMIP5 climate models: MJO skill metrics and process-oriented diagnosis. **Clim Dyn,** v. 49, p. 4023-4045, 2017.

AHN M-S. et al. MJO propagation across the Maritime Continent: Are CMIP6 models better than CMIP5 models? **Geophys Res Lett**, v. 47, e2020GL087250, 2020.

AN, S. I.; WANG, B. Interdecadal change of the structure of the ENSO mode and its impact on the ENSO frequency. **J Clim**, v. 13, p. 2044-2055, 2000.

ALVAREZ, M. S. et al. Influence of the Madden Julian Oscillation on precipitation and surface air temperature in South America. **Clim Dyn,** v. 46, p. 245-262, 2015.

ARCODIA, M. C. et al. How MJO teleconnections and ENSO interference impacts U.S. precipitation. **J Clim,** v. 33, p. 4621-4640, 2020.

ASHOK, K.; YAMAGATA, T. The El Niño with a difference. **Nature**, v. 461, n. 24, p. 481-484, 2009.

BORGES, P. A. et al. Extreme rainfall indices in Distrito Federal, Brazil: Trends and links with El Niño southern oscillation and Madden-Julian oscillation. **Int J Climatol**, v. 461, n. 38, p. 4550-4567, 2018.

BUSH, S. J. et al. The effect of increased convection entrainment on Asian monsoon biases in the MetUM general circulation model. **Quarterly Journal of the Royal Meteorological Society,** v. 141, p. 311-326, 2015.

CAI, W. et al. Climate impacts of the El Niño–Southern Oscillation on South America. **Nature Reviews Earth & Environment**, v. 1, n. 4, p. 215-231, 2020.

CARVALHO, L. M. V. et al. The South Atlantic Convergence Zone: intensity, form, persistence, and relationships with intraseasonal to interannual activity and extreme rainfall. **J Clim**, v. 17, p. 88-108, 2004.

CASARIN, D. P.; KOUSKY, V.E. Precipitation anomalies in Southern Brazil and variations of the atmospheric circulation. **Rev Bras Meteor,** v.1, p. 83-90, 1986.

CAZES-BOEZIO, G. et al. Seasonal dependence of ENSO teleconnections over South America and relationships with precipitation in Uruguay. **J Clim**, v. 16, p. 1159-1176, 2003.

CHEN, G.; WANG, B. Effects of Enhanced Front Walker Cell on the Eastward Propagation of the MJO. **J Clim,** v. 31, p. 7719-7738, 2018.

COELHO, C. A. S. et al. Evaluation of climate simulations produced with the Brazilian global atmospheric model version 1.2. **Clim Dyn,** v. 56, p. 873-898, 2020.

CRAIG, A. et al. Development and performance of a new version of the OASIS coupler, OASIS3-MCT_3.0. **Geoscientific Model Development**, v.10, p. 3297-3308, 2017.

CUNNINGHAM, C. A. C.; CAVALCANTI, I. F. de A. Intraseasonal modes of variability affecting the South Atlantic Convergence Zone. **Int J Climatol,** v. 26(9), p. 1165–1180, 2006.

DAWSON, A. Windspharm: A High-Level Library for Global Wind Field Computations Using Spherical Harmonics. **Journal of Open Research Software 4**, 2016.

DEE, D. P. et al. The ERA-Interim reanalysis: configuration and performance of the data assimilation system. **Q J Roy Meteor Soc,** v. 137, p. 553–597, 2011.

DELWORTH, T. L. et al. Simulated climate and climate change in the GFDL CM2.5 high-resolution coupled climate model. **J Clim,** v. 25(8), p. 2755-2781, 2012.

DEMOTT, C. A.; KLINGAMAN, N. P.; WOOLNOUGH, S. J. Atmosphere-ocean coupled processes in the Madden-Julian oscillation. **Rev Geophys,** v. 53, p. 1099-1154, 2015.

DÍAZ, A.; ACEITUNO P. Atmospheric Circulation Anomalies during Episodes of Enhanced and Reduced Convective Cloudiness over Uruguay. **J Clim,** v. 16, p. 3171-3185, 2003.

DUCHON, C. E. Lanczos filtering in one and two dimensions. **J Appl Meteor,** p. 1016-1022, 1979.

FERNANDES, L. G.; RODRIGUES, R. R. Changes in the patterns of extreme rainfall events in Southern Brazil. **Int J Climatol**, v. 38, n. 3, p. 1337–1352, 2018.

FINK, A.; SPETH, P. Some potential forcing mechanisms of the year-to-year variability of the tropical convection and its intraseasonal (25-70-day) variability. **Int J Climatol,** v. 17, p. 1513-1534, 1997.

GANDU, A. W.; SILVA DIAS, P. L. Impact of tropical heat sources on the South American tropospheric upper circulation and subsidence. **J Geophys Res,** v. 103, p.6001-6015, 2018.

GARREAUD, R. D. et al. The Central Chile Mega Drought (2010–2018): A climate dynamics perspective. **Int J Climatol**, v. 40, n. 1, p. 421-439, 2020.

GHELANI, R. P. S. et al. Joint Modulation of Intraseasonal Rainfall in Tropical Australia by the Madden-Julian Oscillation and El Niño-Southern Oscillation. **Geophys Res Lett**, v. 44(20), p. 10754-10761, 2017.

GIDDINGS et al. The effect of seasonally and spatially varying chlorophyll on Bay of Bengal surface ocean properties and the South Asian monsoon. **Weather and Climate Dynamics,** v. 1, p. 635-655, 2020.

GILL, A. E. et al. The vortex created by mass transfer between layers of rotating fluid.

Geophys. Astrophys. Fluid Dyn., v. 12, p. 195-220, 1979.

GILL, A. E. Some simple solutions for heat-induced tropical circulation. **Q J Roy Meteor Soc,** v. 106(449), p. 447-462, 1980.

GOTTSCHALCK J. et al. A framework for assessing operational Madden-Julian Oscillation forecasts. **Bull Am Meteor Soc,** p. 1247-1258, 2010.

GRIMM, A. M. The El Niño Impact on the Summer Monsoon in Brazil: Regional Process versus Remote Influences. **J Clim**, v. 16, p. 263-280, 2003.

GRIMM, A. M. How do La Niña events disturb the summer monsoon system in Brazil? **Clim Dyn,** v. 22, p. 123-138, 2004.

GRIMM, A. M. Interannual climate variability in South America: Impacts on seasonal precipitation, extreme events, and possible effects of climate change. **Stoch Environ Res Risk Assess,** v. 25(4), p. 537–554, 2011.

GRIMM, A. M. **South American Monsoon and its Extremes**. In: Vuruputur VJ, Sukhatme R, Murtugudde R, Roca (eds) Tropical Extremes: Natural Variability and Trends, Elsevier, Amsterdam, p. 51-93, 2018.

GRIMM, A. M. Madden-Julian Oscillation impacts on South America summer monsoon season: precipitation anomalies, extreme events, and teleconnections. **Clim Dyn,** v. 53, p. 907-932, 2019.

GRIMM, A. M. et al. Precipitation anomalies in Southern Brazil associated with El Niño and La Niña events. **J Clim**, v.11, p. 2863-2880, 1998.

GRIMM, A. M. et al. Climate Variability in Southern South America Associated with El Niño and La Niña Events. **J Clim**, v. 13, p. 35-58, 2000.

GRIMM, A. M. et al. The South American Monsoon System. In: CHANG, C. P.; WANG B.; LAU N. C. G. **The Global Monsoon System: Research and Forecast**, WMO/TD 1266 – TMRP70, p. 219-238, 2005. Disponível para download em: www.wmo.int/pages/prog/arep/tmrp/documents/global_monsoon_system_IWM3.pdf.

GRIMM, A. M. et al. Connection between spring conditions and peak summer monsoon rainfall in South America: role of soil moisture surface temperature, and topography in eastern Brazil. **J Clim**, v. 20, p. 5929-5945, 2007.

GRIMM, A. M. et al. Interdecadal variability and extreme precipitation events in South America during the monsoon season. **Climate Research**, v. 68, p. 277-294, 2016.

GRIMM, A. M. et al. Active and break phases of the South American summer monsoon: MJO influence and subseasonal prediction. **Clim Dyn,** (0123456789), 2021.

GRIMM, A. M. et al. The combined effect of climate oscillations in producing extremes: the 2020 drought in southern Brazil. **Brazilian Journal of Water Resources**, 25(e48), 2021.

GRIMM, A. M; ACEITUNO, P. El Niño, novamente! **Rev Bras Meteor,** v. 34, n. 4, p. 351-357, 2015.

GRIMM, A. M.; AMBRIZZI, T. **Teleconnections into South America from the Tropics and Extratropics on Interannual and Intraseasonal timescales**. In: Vimeux F, Sylvestre F, Khodri (eds) M. Past climate variability in South America and Surrounding Regions: from the last glacial maximum to the Holocene, 14ª ed. Springer, USA, p 159-191, 2009.

GRIMM, A. M.; NATORI, A. A. Climate change and interannual variability of precipitation in South America. **Geophys Res Lett**, v. 33, p. 1–5, 2006.

GRIMM, A. M; SABOIA, J. P. J. Interdecadal variability of the South American precipitation in the monsoon season. **J Clim**, v. 28, p. 755-775, 2015.

GRIMM, A. M.; SILVA DIAS, P. L. Analysis of tropical-extratropical interactions with influence functions of a barotropic model. **J Atmos Sci,** v. 52, 3538-3555, 1995.

GRIMM, A. M.; SILVA DIAS, M. A. F. Synoptic and Mesoscale Processes in the South American Monsoon. In: CHANG, C. P.; DING Y.; LAU N. C. G. JOHNSON, R. H.; WANG, B; YASUNARI, T. **The Global Monsoon System: Research and Forecast**, **World Scientific Series on Asia-Pacific Weather and Climate**, v. 5, World Scientific Publishing Company, Singapore, p. 239-256, 2011.

GRIMM, A. M.; TEDESCHI, R. G. ENOS and Extreme Rainfall Events in South America. **J Clim**, v. 22, p. 1589-1609, 2009.

GRIMM, A. M.; ZILLI, M. T. Interannual Variability and Seasonal Evolution of Summer Monsoon Rainfall in South America. **J Clim,** v. 22, p. 2257-2275, 2009.

GUTZLER, D. S. Interannual Fluctuations of Intraseasonal Variance of Near- Equatorial Zonal Winds. **J Geophys Res,** v. 96, p. 3173-3185, 1991.

HENDERSON, S. A. et al. Madden-Julian oscillation Pacific teleconnections: The impact of the basic state and MJO representation in general circulation models. **J Clim,** v. 30(12), p. 4567-4587, 2017.

HENDERSON, S. A. et al. The Impact of the Madden-Julian Oscillation on High-Latitude Winter Blocking during El Niño-Southern Oscillation Events. **J Clim,** v. 31, p. 5293-5318, 2018.

HENDON, H. H. et al. Interannual variation of the Madden-Julian oscillation during austral summer. **J Clim**, v. 12, p. 2538-2550, 1999.

HENDON, H. H. et al. Seasonal Dependence of the MJO-ENSO Relationship. **J Clim,** v. 20, p.531-543, 2007.

HIRATA, F. E.; GRIMM, A. M. The role of synoptic and intraseasonal anomalies in the life cycle of summer rainfall extremes over South America. **Clim Dyn,** v. 46, p. 3041-3055, 2015.

HIRATA, F. E.; GRIMM, A. M. Extended-range prediction of South Atlantic convergence zone rainfall with calibrated CFSv2 reforecast. **Clim Dyn,** v. 50, p. 3699-3710, 2018.

HIRONS, L. C.; KLINGAMAN, N. P.; WOOLNOUGH, S; J. MetUM-GOML: A near-globally coupled atmosphere-ocean-mixed-layer model. **Geoscientific Model Development**, v. 8, p. 363-379, 2015.

INTERGOVERNMENTAL PANEL ON CLIMATE CHANGE (IPCC, 2013). **Climate Change 2014 Synthesis Report**. Available on: https://archive.ipcc.ch/pdf/assessment-report/ar5/syr/SYR_AR5_FINAL_full_wcover.pdf. Accessed on: 10/07/2017.

JIANG, X. et al. Vertical structure and physical processes of the Madden-Julian oscillation: Exploring key model physics in climate simulations. **J Geophys Res: Atmos**, v. 120, p. 4718-4748, 2015.

JIN, E. K. et al. Currente status of ENSO prediction skill in coupled ocean-atmosphere models. **Clim Dyn,** v. 31, p. 647-664, 2008.

JOLLIFFE, I. T. **Principal Component Analysis**. 2nd edition. New York: Springer, 487 p., 2002.

JONES, C. et al. Global occurrences of extreme precipitation events and the Madden-Julian oscillation: Observations and predictability. **J Clim**, v. 17, p. 4575-4589, 2004.

JUNG, T. et al. High-resolution global climate simulations with the ECMWF model in project athena: Experimental design, model climate, and seasonal forecast skill. **J Clim,** v. 25(9), p. 3155-3172, 2012.

KALNAY, E. et al. The NCEP/NCAR 40-year reanalysis project **Bull Am Meteor Soc,** v.77, p. 437-471, 1996.

KAYANO, M. T.; ANDREOLI, R. V. Clima da região Nordeste do Brasil. In: Cavalcanti et al. [organizadores]. **Tempo e Clima no Brasil**. São Paulo: Oficina de Textos, 2009. p. 213-233.

KAYANO, M. T.; CAPISTRANO, V. B. How the Atlantic multidecadal oscillation (AMO) modifies the ENSO influence on the South American rainfall. **Int J Climatol**, v. 34, p. 162-178, 2014.

KAYANO, M. T.; KOUSKY, V. E. Intraseasonal (30—60 day) variability in the global tropics: principal modes and their evolution. **Tellus**, v. 51A, p. 373-386, 1999.

KESSLER, W. S. EOF representations of the Madden-Julian and its connection with ENSO. **J Clim**, v. 14, n. 13, p. 3055-3061, 2001.

KIM, D. et al. A systematic relationship between intraseasonal variability and mean state bias in AGCM simulations. **J Clim,** v. 24(21), p. 5506-5520, 2011.

KIM, D. et al. Propagating versus nonpropagating Madden–Julian oscillation events. **J Clim,** v. 27, p. 111–125, 2014.

KIM, D.; KIM, H.; LEE, M. Why does the MJO detour the Maritime Continent during austral summer? **Geophys Res Lett**, v. 44, n. 5, p. 2579-2587, 2017.

KIM, H. et al. Prediction of the Madden-Julian oscillation: A review. **J Clim,** v. 31(23), p. 9425–9443, 2018.

KLINGAMAN, N. P. et al. Vertical structure and physical processes of the Madden-Julian oscillation: Synthesis and summary. **J Geophys Res: Atmos**, v. 120, n. 10, p. 4671-4689, 2015.

KLINGAMAN, N. P. et al. Subseasonal Prediction Performance for Austral Summer South American Rainfall. **Weather and Forecasting,** v. 36(1), p. 147-169, 2020.

KLINGAMAN, N. P.; DEMOTT, C. A. Mean State Biases and Interannual Variability Affect Perceived Sensitivities of the Madden-Julian Oscillation to Air-Sea Coupling. **Journal of Advances in Modeling Earth Systems**, v. 12(2), p. 1-22, 2020.

KLINGAMAN, N. P.; WOOLNOUGH, S. J. The role of air-sea coupling in the simulation of the Madden-Julian oscillation in the Hadley Centre model. **Q J Roy Meteor Soc,** v. 140, p. 2272-2286, 2014a.

KLINGAMAN, N. P.; WOOLNOUGH, S. J. Using a case-study approach to improve the Madden-Julian oscillation in the Hadley Centre model. **Q J Roy Meteor Soc,** v. 140(685), p. 2491-2505, 2014b.

KODAMA, C. et al. A 20-Year climatology of a NICAM AMIP-type simulation. **J Meteorol Soc Jpn,** v. 93(4), pp. 393-424, 2015.

KOUSKY, V. E. et al. A review of the Southern Oscillation: oceanic-atmospheric circulation changes and related rainfall anomalies. **Tellus**, v. 36, p. 490-504, 1984.

LARGE, W. J. et al. Oceanic vertical mixing: A review and a model with a nonlocal boundary layer parameterization. **Rev Geophys,** v.32, p. 363-403, 1994.

LEE, R. W. et al. ENSO Modulation of MJO Teleconnections to the North Atlantic and Europe, **Geophys Res Lett**, v. 46(22), p. 13535-13545, 2019.

LEE, T.; MCPHADEN, M. J. Increasing intensity of El Niño in the central-equatorial **Pacific. Geophys Res Lett**, v. 37, n. 14, 2010.

LIEBMANN, B.; ALLURED, D. Daily Precipitation Grids for South America. **Bull Am Meteor Soc,** v. 86, p. 1567-1570, 2005.

LIEBMANN, B.; MECHOSO, C. R. The South American Moonson System. In: CHANG, C. P.; DING Y.; LAU N. C. G.; JOHNSON, R. H.; WANG, B; YASUNARI, T. **The Global Monsoon System: Research and Forecast**, **World Scientific Series on Asia-Pacific Weather and Climate**, v. 5, World Scientific Publishing Company, Singapore, p. 137-157, 2011.

LIEBMANN, B.; SMITH, C. A. Description of a Complete (Interpolated) Outgoing Longwave Radiation Dataset. **Bull Am Meteor Soc,** v. 77, p.1275-1277, 1996.

LIM, H.; CHANG, C. P. Dynamics of teleconnections and Walker circulations forced by equatorial heating. **J Atmos Sci,** v. 40, p. 1897-1914, 1983.

LIU, X. et al. MJO prediction using the sub-seasonal to seasonal forecast model of Beijing Climate Center. **Clim Dyn,** v. 48(9–10), p. 3283-3307, 2017.

LIU, F.; WANG B. Roles of the Moisture and Wave Feedbacks in Shaping the Madden-Julian Oscillation. **J Clim,** v. 30, p. 10275-10291, 2017.

LORREY, A. et al. Reconstructing the South Pacific Convergence Zone Position during the Presatellite Era: A La Niña Case Study. **Mon Weather Rev,** v. 140, p. 3653-3668, 2012.

MADDEN, R.; JULIAN, P. Detection of a 40-50 day oscillation in the zonal wind in the Tropical Pacific. **J Atmos Sci,** v.28, p. 702-708, 1971.

MADDEN, R.; JULIAN, P. Description of global-scale circulation cells in the tropics with a 40-50 day period. **J Atmos Sci,** v.29, p. 1109-1123, 1972.

MALONEY, E. D.; WOLDING, B. O. Initiation of an intraseasonal oscillation in an aquaplanet general circulation model. **Journal of Advances in Modeling Earth Systems**, v. 7, p. 1956-1976, 2015.

MARENGO, J. A. Interannual Variability of Surface Climate in the Amazon Basin. **Int J Climatol**, v. 12, p. 853-863, 1992.

MASUNAGA, H. Seasonality and regionality of the Madden-Julian Oscillation, Kelvin Wave, and equatorial Rossby Wave. **J Atmos Sci,** v.64, p. 4400-4416, 2007.

MATSUNO, T. Quasi-Geostrophic Motions in the Equatorial Area. **J Meteorol Soc Jpn,** v. 44(1), p. 25-43, 1966.

MECHOSO, C. R. et al. The American monsoon systems: An introduction. **The Global Monsoon System: Research and Forecast**, cap. 13, p. 197-206, 2005.

MO, K. C. Relationships between low frequency variability in the Southern Hemisphere and sea surface temperature anomalies. **J Clim**, v. 13, p. 3599-3610, 2000.

MONERIE, P.-A. et al. Role of atmospheric horizontal resolution in simulating tropical and subtropical South American precipitation in HadGEM3-GC31. **Geoscientific Model Development Discussions,** (June), p. 1-44, 2020.

MOON, J. Y. et al. ENSO regulation of MJO teleconnection. **Clim Dyn,** v. 37(5), p.1133-1149, 2011.

NOGUÉS-PAEGLE, J. et al. Alternating Wet and Dry over South American during summer. **Mon Weather Rev,** v. 125, p. 279-291, 1997.

PAEGLE, J. N. et al. Intraseasonal Modulation of South American Summer Precipitation. **Mon Weather Rev,** v. 128, p. 837-850, 2000.

PEATMAN, S. C.; KLINGAMAN, N. P. The Indian summer monsoon in MetUM-GOML2.0: effects of air-sea coupling and resolution. **Geoscientific Model Development**, v. 11, p. 4693-4709, 2018.

POHL, B.; MATTHEWS A. J. Observed Changes in the Lifetime and Amplitude of the Madden-Julian Oscillation Associated with Interannual ENSO Sea Surface Temperature Anomalies. **J Clim,** v. 20, p. 2659-2674, 2007.

RAO, V. B.; HADA K. Characteristics of Rainfall over Brazil: Annual Variations and Connections with the Southern Oscillation. **Theor Appl Clim,** v. 42, p. 81-91, 1990.

RAYNER, N. A. et al. Global analyses of sea surface temperature, sea ice, and night marine air temperature since the late nineteenth century. **J Geophys Res: Atmos**, v. 108, 2003.

RICHMAN, M. B. Rotation of Principal Components. **J Climatol,** v. 6, p. 293-335, 1986.

RODRIGUES, R. R. et al. The Impacts of Inter–El Niño Variability on the Tropical Atlantic and Northeast Brazil Climate. **J Clim**, v. 24, n. 13, p. 3402-3422, 2011.

RODRIGUES, R. R.; MCPHADEN, M. J. Why did the 2011-2012 La Niña cause a severe drought in the Brazilian Northeast? **Geophys Res Lett**, v. 24, n. 13, p. 1012-1018, 2014.

ROPELEWSKI, C. F.; HALPERT, M. S. Global and Regional Scale Precipitation Patterns Associated with the El Niño/Southern Oscillation. **Mon Weather Rev,** v. 115, p. 1606-1626, 1987.

ROUNDY, P. E. et al. Modulation of the global atmospheric circulation by combined activity in the Madden-Julian oscillation and the El Niño-southern oscillation during boreal winter. **J Clim**, v. 23(15), p. 4045-4059, 2010.

SAKAEDA, N.; ROUNDY, P. E. The development of upper-tropospheric geopotential height anomaly in the Western Hemisphere during MJO convective initiations. **Q J Roy Meteor Soc,** v. 142(695), p. 942-956, 2016.

SEO, K. H.; KIM, K. Y. Propagation and initiation mechanisms of the Madden-Julian oscillation. **J Geophys Res**, v. 108(D13), p. 4384-4406, 2003.

SHAFFREY, L. C. et al. U.K. HiGEM: The new U.K. high-resolution global environment model - Model description and basic evaluation. **J Clim,** v. 22(8), p. 1861-1896, 2009.

SHIMIZU, M. H.; AMBRIZZI, T. MJO influence on ENSO effects in precipitation and temperature over South America. **Theor Appl Clim,** v. 124, p. 291-301, 2015.

SHIMIZU, M. H. et al. Extreme precipitation events and their relationship with ENSO and MJO phases over northern South America. **Int J Climatol**, v. 37, p. 2977-2989, 2017.

SLINGO, J. M. et al. On the predictability of the interannual behaviour of the Madden-Julian Oscillation and its relationship with El Nino. **Q J Roy Meteor Soc,** v. 125(554), p.583-609, 1999.

SMITH, D. M.; MURPHY, J. M. An objective ocean temperature and salinity analysis using covariances from a global climate model. **J Geophys Res**, v. 12(C02022), 2007.

SOLMAN, S. A.; BLÁZQUEZ, J. Multiscale precipitation variability over South America: Analysis of the added value of CORDEX RCM simulations. **Clim Dyn,** v. 53(3–4), p. 1547-1565, 2019.

SOUZA, E. B.; AMBRIZZI, T. Modulation of the Intraseasonal rainfall over Tropical Brazil by the Madden-Julian Oscillation. **Int J Climatol**, v. 26, p. 1759-1776, 2006.

de SOUZA CUSTODIO, M. et al. Analysis of precipitation climatology simulated by high resolution coupled global models over the South America. **Hydrological Res Lett,** v. 6(0), p. 92-97, 2012.

de SOUZA CUSTODIO, M. et al. Impact of increased horizontal resolution in coupled and atmosphere-only models of the HadGEM1 family upon the climate patterns of South America. **Clim Dyn,** v. 48(9–10), p. 3341–3364, 2017.

STRAUB, K. H. MJO Initiation in the Real-Time Multivariate MJO Index. **J Clim,** v. 26, p. 1130-1151, 2013.

TAM, C. Y.; LAU, N. C. Modulation of the Madden-Julian Oscillation by ENSO: Inferences from Observations and GCM Simulations. **J Meteorol Soc Jpn,** v. 83, p. 727-743, 2005.

TEDESCHI, R. G. et al. Influences of two types of ENSO on South American precipitation. **Int J Climatol**, v. 33, n. 6, p. 1382-1400, 2013.

TEDESCHI, R. G. et al. Influence of Central and East ENSO on extreme events of precipitation in South America during austral spring and summer. **Int J Climatol**, v. 33, p. 2045-2064, 2015.

TEDESCHI, R. G. et al. Influence of Central and East ENSO on precipitation and its extreme events in South America during austral autumn and winter. **Int J Climatol**, v. 36, p. 4797-4814, 2016.

TRENBERTH, K. E. The definition of El Niño. **Bull Am Meteor Soc,** v.78, n.12, p. 2771-2777, 1997.

TRENBERTH, K. E.; STEPANIAK, D. P. Indices of El Niño Evolution. **J Clim**, v. 14, p. 1697-1701, 2001.

TSENG, K. C. et al. The consistency of MJO teleconnection patterns on interannual time scales. **J Clim**, v. 33(9), p. 3471-3486, 2020.

UVO, C. B. et al. The Relationships between Tropical Pacific and Atlantic SST and Northeast Brazil Monthly Precipitation. **J Clim**, v. 11, p. 551-562, 1998.

VELASCO, I. & FRITSCH, J. M. Mesoscale Convective Complexes in the Americas. **J Geophys Res**, v. 92, p. 9591-9613, 1987.

VERA, C. G. et al. Differences in El Niño response over the Southern Hemisphere. **J Clim**, v. 17, p. 1741-1753, 2004.

VERA, C. G. et al. Toward a Unified View of the American Monsoon Systems. **J Clim**, v. 19, p. 4977-5000, 2006.

VINCENT, E. M. et al. Interannual variability of the South Pacific Convergence Zone and implications for tropical cyclone genesis. **Clim Dyn,** v. 36, p. 1881-1896, 2009.

VITART, F. et al. The subseasonal to seasonal (S2S) prediction project database. **Bull Am Meteor Soc,** v. 98(1), p. 163-173, 2017.

VITART, F.; MOLTENI, F. Simulation of the Madden-Julian oscillation and its teleconnections in the ECMWF forecast system. **Q J Roy Meteor Soc,** v. 136(649), p. 842-855, 2010.

VITART, F.; ROBERTSON, A. and S2S Steering Group. **Sub-seasonal to seasonal prediction: Linking weather and climate.** Seamless Prediction of the Earth System: From Minutes to Months, G. Brunet, S. Jones, and P. M. Ruti, Eds., WMO-1156, World Meteorological Organization, p. 385-401, 2015. [Available online at http://library.wmo.int/pmb_ged/wmo_1156_en.pdf.]

WALISER, D. E. et al. Potential predictability and the Madden-Julian Oscillation. **Bull Am Meteor Soc,** v. 84, p. 33-50, 2003.

WALTERS, D. et al. The Met Office Unified Model Global Atmosphere 7.0/7.1 and JULES Global Land 7.0 configurations. **Geoscientific Model Development**, v.12, p. 1909-1963, 2019.

WANG, B. et al. A trio-interaction theory for Madden-Julian oscillation. **Geoscience Letters**, p. 3-34, 2016.

WANG, J. et al. MJO teleconnections over the PNA region in climate models. Part I: Performance- And process-based skill metrics. **J Clim,** v. 33(3), p. 1051-1067, 2020a.

WANG, J. et al. MJO Teleconnections over the PNA Region in Climate Models. Part II: Impacts of the MJO and Basic State. **J Clim,** v. 33(12), p. 5081-5101, 2020b.

WANG, L. et al. Impact of Rossby and Kelvin Wave Components on MJO Eastward Propagation. **J Clim,** v. 31, p. 6913-6931, 2018.

WEI, Y.; REN, H-L. Modulation of ENSO on Fast and Slow MJO Modes during Boreal Winter. **J Clim,** v. 32 p. 7483-7506, 2019.

WEISHEIMER, A. et al. Addressing model error through atmospheric stochastic physical parametrizations: Impact on the coupled ECMWF seasonal forecasting system. **Philosophical Transactions of the Royal Society A: Mathematical, Physical and Engineering Sciences**, v. 372, n. 2018, p. 1-21, 2014.

WHEELER, M. C. et al. Impacts of the Madden-Julian Oscillation on Australian Rainfall and Circulation. **J Clim,** v. 22, p. 1482-1498, 2009.

WHEELER, M. C.; HENDON, H. H. An all-season real-time multivariate MJO index: development of an index for monitoring and prediction. **Mon Weather Rev,** v. 132, p. 1917-1932, 2004.

WILKS, D. S.; **Statistical Methods in the Atmospheric Sciences**. United States of America: Academic Press, 627 p., 2006.

WMO. **Technical regulations, Volume I – General meteorological standards and recommended practices.** WMO Basic Documents No. 2, 48p., 2019. https://library.wmo.int/doc_num.php?explnum_id=10113.

WOOLNOUGH, S. J. et al. The relationship between convection and sea surface temperature on intraseasonal timescales. **J Clim,** v.13(12), p. 2086-2104, 2000.

YEH, S. W. et al. El Niño in a changing climate. **Nature**, v. 461, p. 511-514, 2009.

ZHANG, C. Madden-Julian Oscillation. **Rev Geophys,** v. 43, p. 1-36, 2005.

ZHANG, C.; GOTTSCHALCK, J. SST anomalies of ENSO and the Madden-Julian Oscillation in the Equatorial Pacific. **J Clim,** v. 15, p. 2429-2445, 2002.

ZHANG, C.; LING, J. Barrier Effect of the Indo-Pacific Maritime Continent on the MJO: Perspectives from Tracking MJO Precipitation. **J Clim,** v. 30, p. 3439-3459, 2017.